X-ray cluster **selection**
& **mass calibration**

Stefano Ettori
INAF-OAS / INFN Bologna

Outline (covered by Lorenzo; not covered but potentially relevant):

- ***Intro:*** Stage-IV, on the selection, high-z
- ***Scaling laws:*** dynamical state, astrophysics at low-M, evolution
- ***Hydrostatic mass:*** limits, uncertainties, biases (& T cross-calib)
- ***internal structure as complementary proxy***
  (c-M-z; sparcity; f_{gas})
- Generalized-SR (Ettori 13, 15); universal ICM profiles (Ettori+23)

Stage-IV

The Dark Energy Task Force (DETF) report [Albrecht+06] classified DE surveys into an approximate sequence: on-going projects, either taking data or soon to be taking data, are Stage II; near-future, intermediate-scale projects are Stage III (DES, KiDS, HSC); and larger-scale, longer-term future projects are designated Stage IV (Euclid; LSST; SKA; JDEM/WFIRST; CMB-S4). More advanced stages are in general expected to deliver tighter dark energy constraints, which the DETF quantified using the w_0-w_a FoM:

$$FoM \propto (\sigma_{w0}\sigma_{wa})^{-1}$$

W.r.t. Stage II, Stage III experiments are expected to deliver a ~ x3-5 *in combination*; Stage IV experiments should improve the FoM by ~10; these estimates are subject to considerable systematic uncertainties

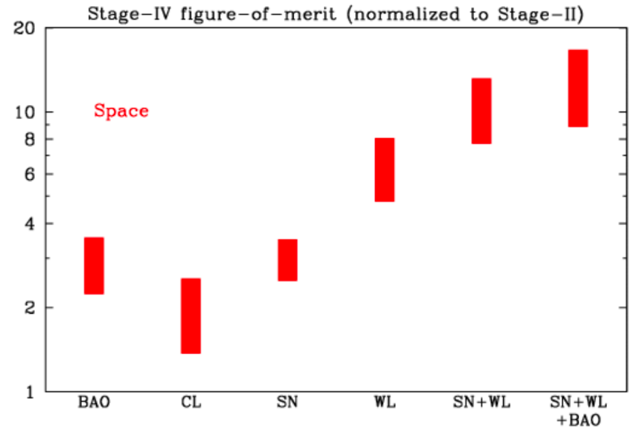

Illustration of the potential improvement in the DETF figure of merit arising from Stage IV space-based projects. The bars extend from the pessimistic to the optimistic projections in each case. The final two error bars illustrate the improvement available from combining techniques; other combinations of techniques may be superior or more cost-effective. CL results are from an x-ray satellite; the others results from an optical/NIR satellite.

Stage-IV

DETF (Albrecht+06)

4. The techniques are at different levels of maturity:
   a. The **BAO** technique has only recently been established. It is less affected by astrophysical uncertainties than other techniques.
   b. The **CL** technique has the statistical potential to exceed the BAO and SN techniques but at present has the largest systematic errors. Its eventual accuracy is currently very difficult to predict and its ultimate utility as a dark energy technique can only be determined through the development of techniques that control systematics due to non-linear astrophysical processes.
   c. The **SN** technique is *at present* the most powerful and best proven technique for studying dark energy. If redshifts are determined by multiband photometry, the power of the supernova technique depends critically on the accuracy achieved for photo-z's. **(Multiband photometry measures the intensity of the object in several colors. A redshift determined by multiband photometry is called photometric redshift, or a photo-z.)** If spectroscopically measured redshifts are used, the power of the experiment as reflected in the DETF figure of merit is much better known, with the outcome depending on the uncertainties in supernova evolution and in the astronomical flux calibration.
   d. The **WL** technique is also an emerging technique. Its eventual accuracy will also be limited by systematic errors that are difficult to predict. *If* the systematic errors are at or below the level asserted by the proponents, it is likely to be the most powerful individual Stage-IV technique and also the most powerful component in a multi-technique program.

- **Galaxy Cluster Counting (CL) [*Dark-energy Observables:* $D^2(z)/H(z)$ and $g(z)$]**
  - ***Strengths:*** Galaxy-cluster abundances are sensitive to both the expansion and growth histories of the Universe, in this case with extremely strong dependence on the growth factor. There are multiple approaches to cluster detection: the Sunyaev-Zeldovich (SZ) effect, x-ray emission, lensing shear, and of course optical detection of the cluster galaxies. A large SZ cluster survey (SPT) is already funded, and is the only funded project in our Stage III class.
  - ***Weaknesses:*** While *N*-body simulations will be able to predict the abundance of clusters vs. mass and vs. lensing shear to high accuracy, the prediction of SZ, x-ray, or galaxy counts is subject to substantial uncertainties in the baryonic physics. Dark-energy constraints are very sensitive to errors in these "mass-observable" relations, which are likely to dominate the error budget. This method is the one for which our forecasts are least reliable, due to this large astrophysical systematic effect.
  - ***Potential Advantages of LST:*** LST can detect galaxy clusters via the effect of their mass on shear patterns and also via the overdensities of the cluster galaxies themselves. Deep weak-lensing observations would play a key role for calibrating the mass-observable relation for optical (LST) observables as well as SZ and x-ray observables of spatially overlapping SZ or x-ray surveys.
  - ***Potential Advantages of Space Mission:*** An x-ray cluster survey, of course, requires a space mission. With an optical/NIR-imaging space mission, lensing-selected cluster surveys benefit from in the same way as WL surveys do, by offering lower noise levels for WL mapping due to higher density of resolved background galaxies. We subsume consideration of lensing-selected clusters into our WL category because any cosmic-shear survey is also a cluster survey. A similar statement can be made for optically-selected galaxy clusters.
  - ***Potential Advantages of SKA:*** None recognized: cluster galaxies tend to be deficient in neutral hydrogen, so cluster detection is not a strength of SKA.
  - ***Steps to Sharpen Forecasts:*** "Self-calibration" methods can potentially recover much of the information lost to the mass-observable uncertainties, but their efficacy depends critically on the complexity/diversity of cluster baryon evolution. A better understanding of cluster baryonic physics will likely result from the SZ surveys about to commence. Weak-lensing observations of the detected clusters in these surveys may help as well; more generally, intercomparison of all four kinds of observables could constrain many of the uncertain parameters in the mass-observable relations.

The main challenge for using cluster counts for DE tests is that the mass of a cluster is not directly observable. On the other hand it is this richness in the available observables of a cluster that provides the opportunity to calibrate the selection empirically and the checks against systematic errors in the modeling

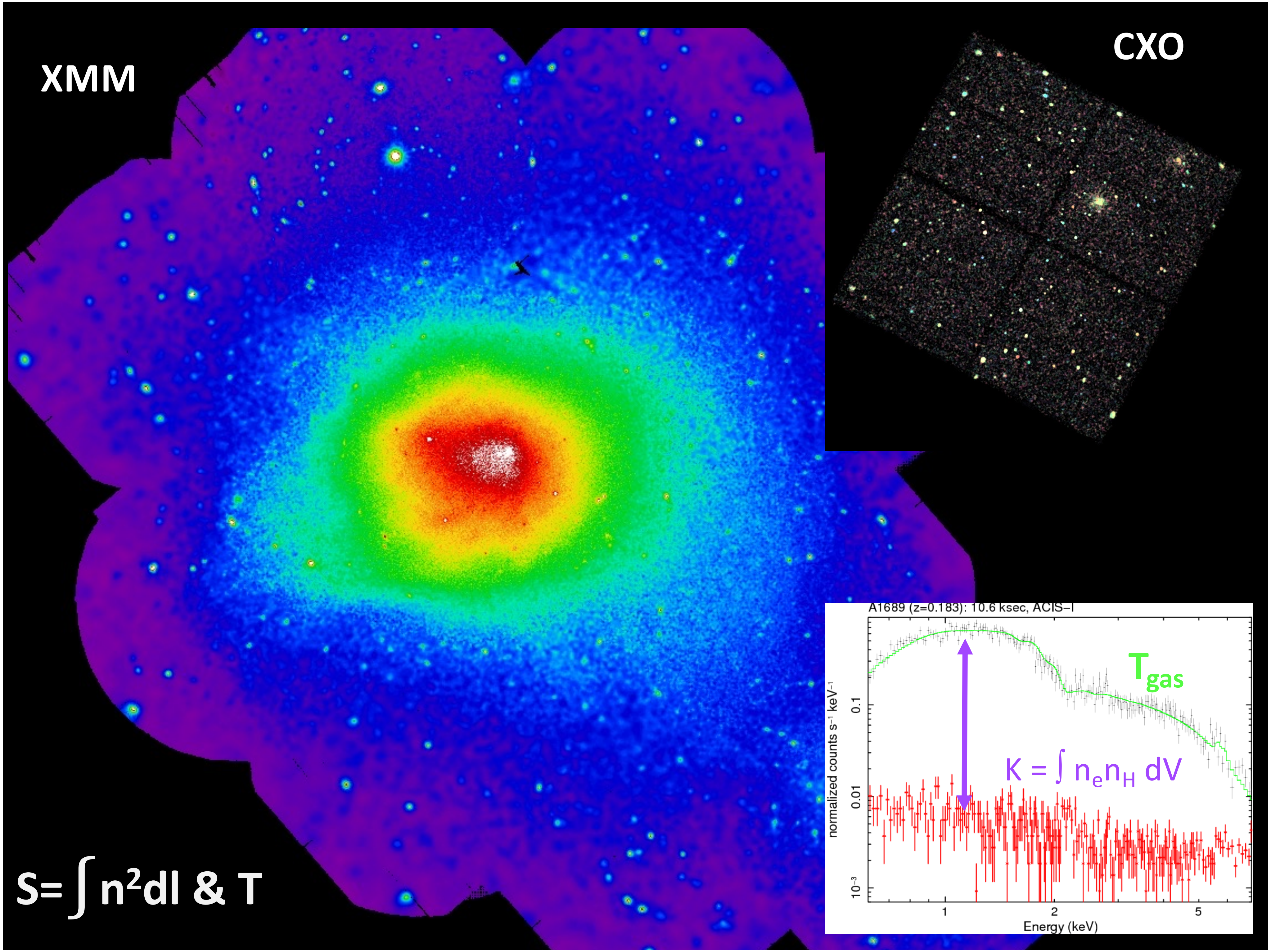
XMM
CXO
$S=\int n^2 dl$ & T
A1689 (z=0.183): 10.6 ksec, ACIS-I
normalized counts s^{-1} keV^{-1}
0.1
0.01
10^{-3}
1
2
5
Energy (keV)
T_{gas}
$K = \int n_e n_H \, dV$

X-ray Cluster Surveys (1980 - present)

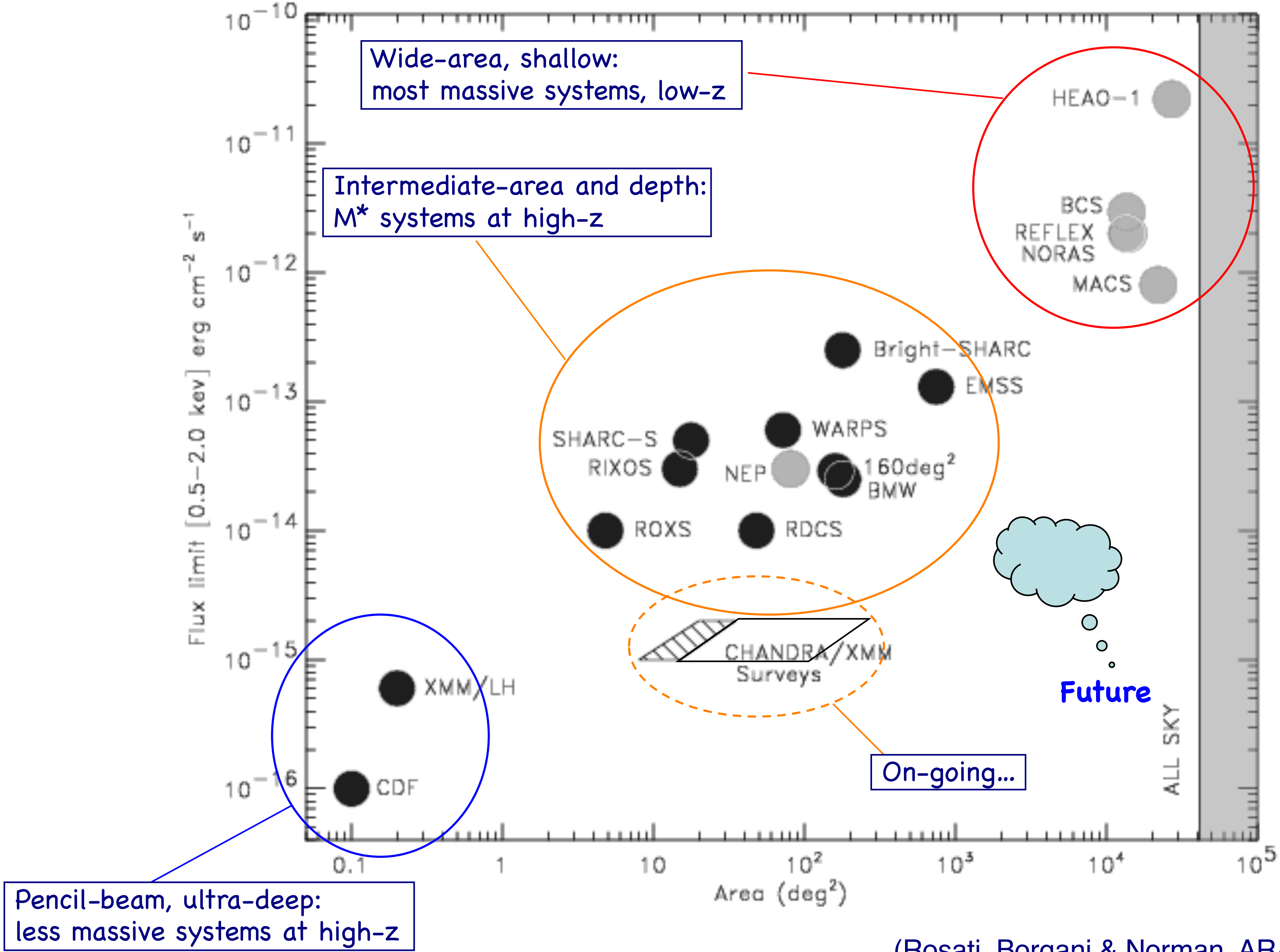

(Rosati, Borgani & Norman, ARAA 2002)

Cosmology with GC

What we need to do cosmology with GC:

1. robust cluster catalogs with large z leverage
   *(with well understood purity & completeness;
   look for DES, SPT-3G, Advanced ACT- Pol,
   eROSITA, LSST, WFIRST-AFTA, Euclid)*

2. accurate absolute mass calibration
   *(from weak lensing, or when we will understand
   better the hydrostatic bias)*

3. sufficiently low-scatter mass proxy information
   *(mainly from X-ray and SZ follow-up; optical probably
   too expensive and still affected from large scatter)*

From observables to mass

Largest sources of systematic err

1. Absolute M_{tot} calibration,
i.e. ***normalization/slope of the scaling relations***
2. Relative M_{tot} calibration at low/high-z,
i.e. ***evolution of the scaling relations***

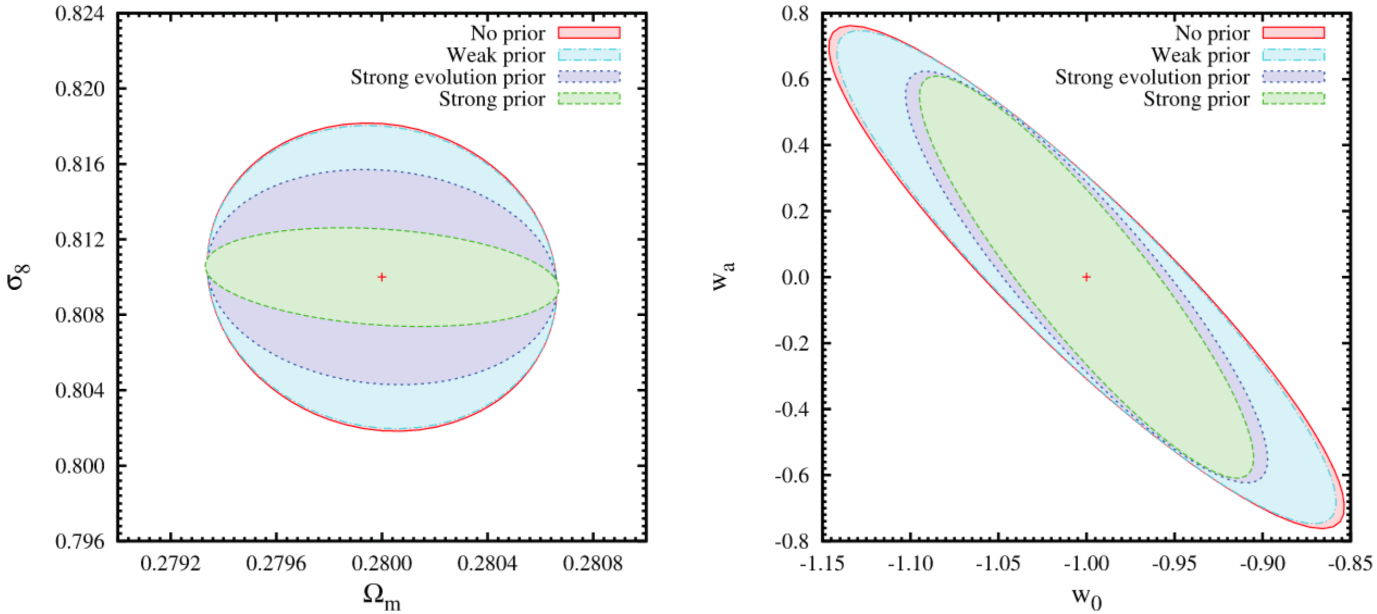

Sartoris+12

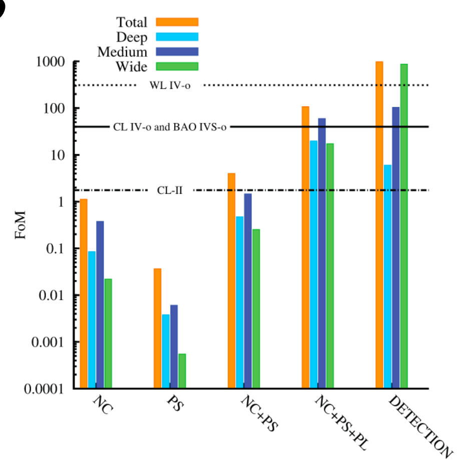

Figure 11. The histograms represent the Figures of Merit for the (w_0, w_a) parameters from WFXT surveys, as derived in the following configurations: by including in the FM the cluster number counts only (NC), the cluster mean power spectrum only (PS), the sum of the two (NC+PS) and by adding the prior from the *Planck* experiment (NC+PS+PL). All these FoM are obtained by assuming *strong prior* on mass parameters. The last group of histograms shows FoMs as obtained in the configuration NC+PS+PL by considering all clusters that can be detected (≈30 source counts) in a given survey and by assuming *no prior* on mass parameters. The FoM for the Deep, the Medium and the Wide cluster surveys are shown with the cyan, blue and green histograms, respectively. The yellow histogram represents the FoM obtained from the combination of the three surveys. The horizontal lines show the FoM as reported in the DETF (Albrecht et al. 2006) for Stage II cluster projects (CL-II; dot–dashed), for optimistic Stage IV BAO and cluster projects (BAO IVS-o and CL IVS-o, respectively; solid line) and for optimistic Stage IV weak lensing project (WL IV-o; dotted line), by combining each probe with CMB *Planck* priors.

From X-ray/SZ integrated quantities to mass

Largest sources of systematic err

1. Absolute M_{tot} calibration,

i.e. ***normalization/slope of the scaling relations***

2. Relative M_{tot} calibration at low/high-z,

i.e. ***evolution of the scaling relations***

Mean statistical err (1 σ)

Err (L) ~ 4% Err (T) ~ 7% Err (M_{gas}) ~ 9%

Err (Y_{SZ}) ~ 14% Err(M_{HE}) ~ 20%

Systematic ~ Statistical err

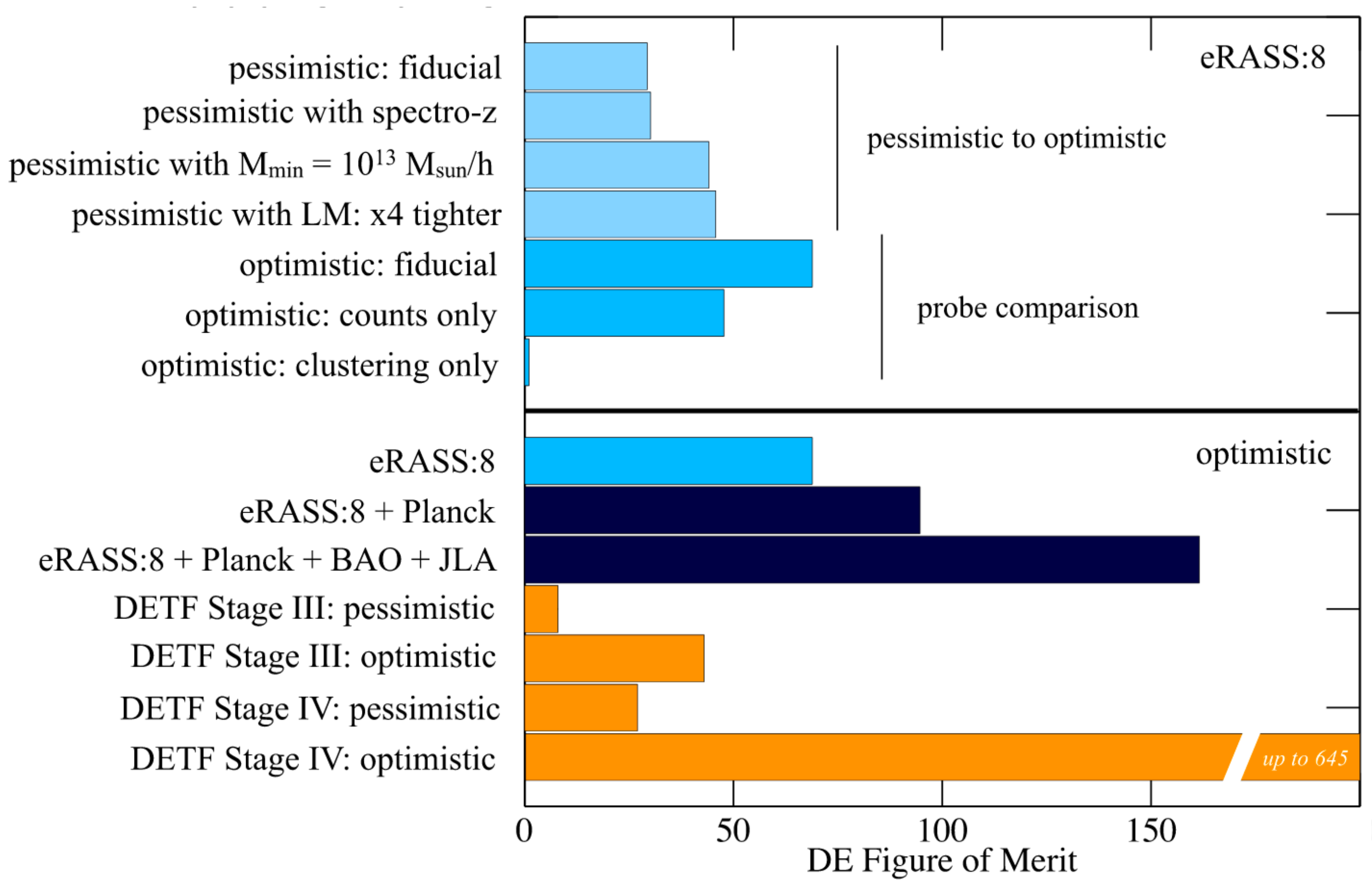

Pillepich+18 **eROSITA: in 66% of sky, ~9e4 objects, median(z)~0.35, M>7e13**; they can simultaneously constrain cosmology, selection effects, and M-O relation by adopting very broad non-informative priors on the slope, normalization, time-evolution, and scatter of L_X-M relation. Tightening of the constraints from pessimistic to optimistic scenario: (i) better knowledge of the LM relation ($\boldsymbol{\sigma}_8$ Ω_m), (ii) the lower mass threshold (1e13), particularly for the DE sector. NB when group-size objects are included in the analysis +pessimistic priors on the LM are adopted, errors on w_0 and w_a shrink by about an additional 20–30 per cent in comparison to the case when only high-mass objects are included in the analysis.

No groups, no party

- ✓ Excluding low-M systems significantly reduces the cosmological parameter constraints
- ✓ Increasing incompleteness of parent samples in the low-M regime together with a steeper Lx–M relation observed for groups can lead to biased cosmological parameters (lower Ω_M and/or σ_8; Schellenberger & Reiprich 17)
- ✓ Galaxy groups often show lower/flatter Sx than clusters (e.g. Ponman+, Sanderson+) ➔ less robust than the properties derived for galaxy clusters
- ✓ But they are very common: a factor of ~30/210/1500 more objects in the mass range $M_{500} = 10^{13}$ Msun – M1 than in M_{500} > M1, and M1 = 1/2/5 × 10^{14}M @z=0

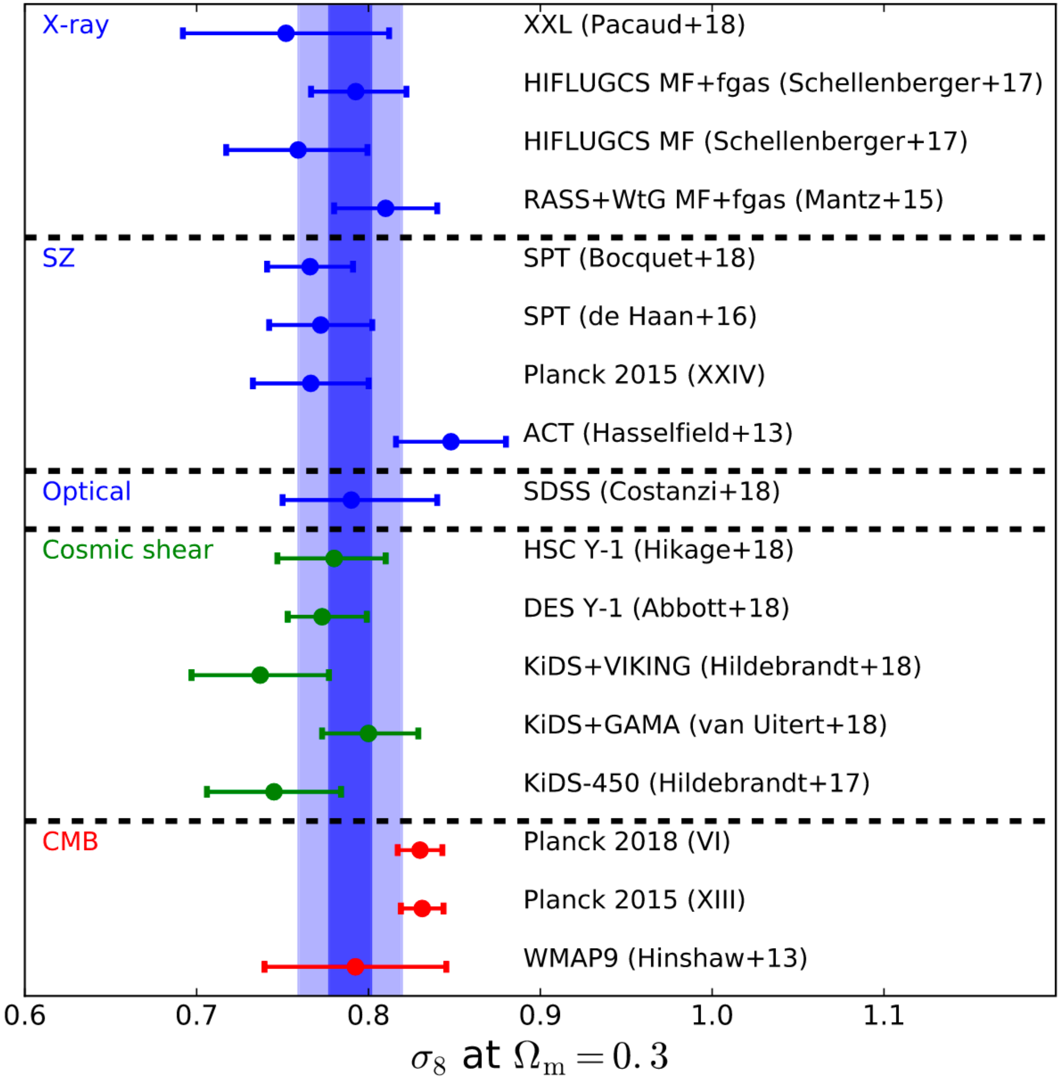

From Pratt+19, Lovisari+21

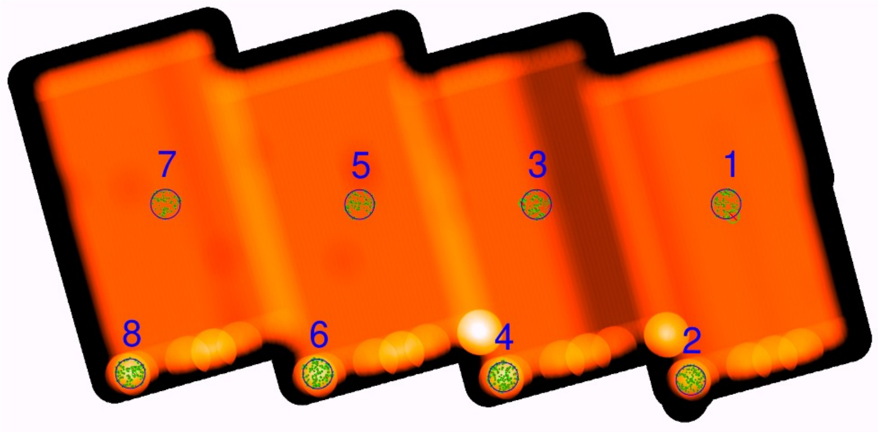

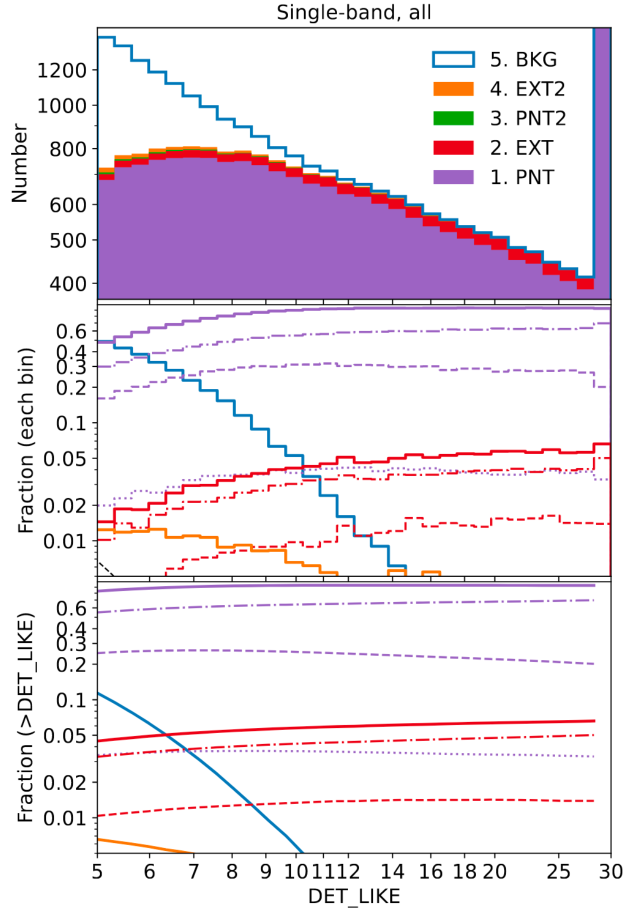

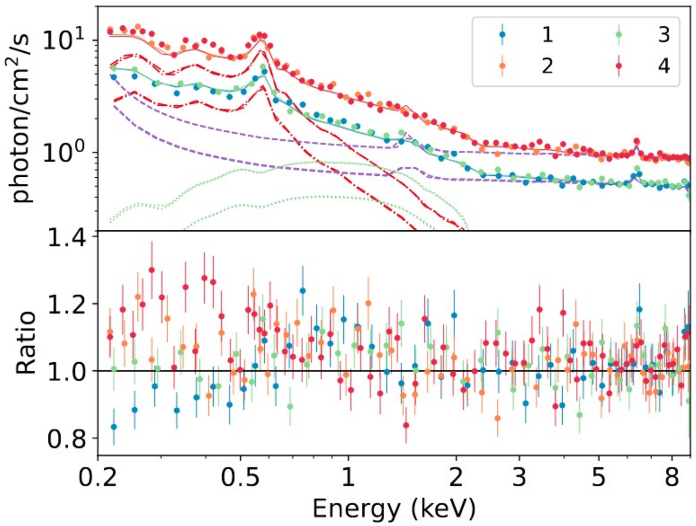

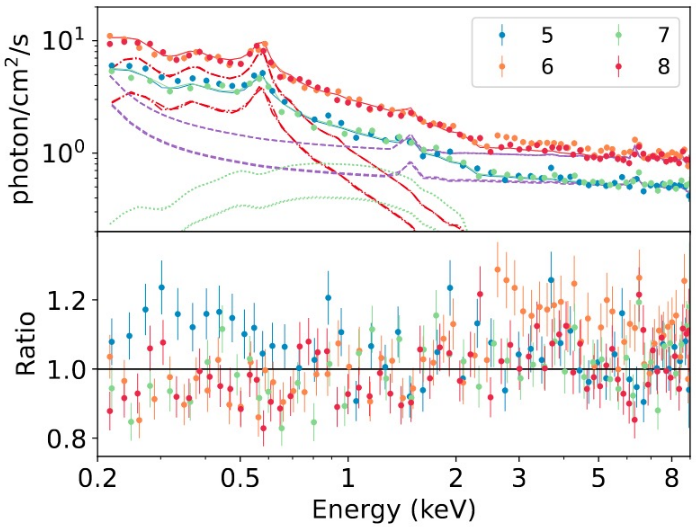

T. Liu+22 validate with extensive photon-event simulations based on instrument characteristics, bkg spectrum, and pop of X-ray sources the strategy implemented in Brunner+22... NB halo with profiles assigned from a generator trained on a set of observed clusters (Comparat+20), isothermal

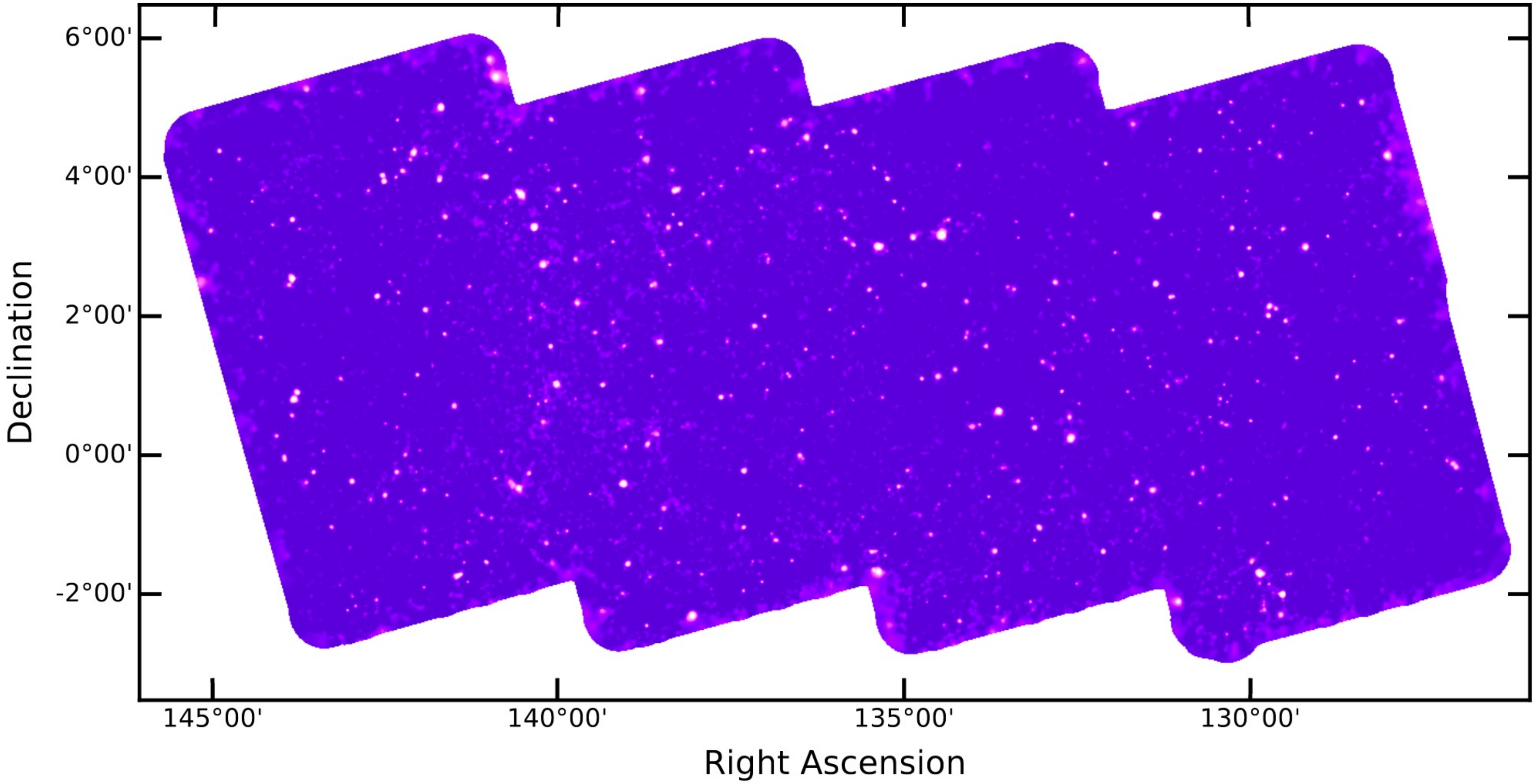

Selection	Number of clusters	z_{median}	Flux limit (0.5–2 keV, 1 arcmin)	Completeness	Purity
Full sample	542	0.35	10^{-14} erg s^{-1} cm^{-2}	40%	80%
$\mathcal{L}_{\text{ext}} \geq 12$	325	0.34	1.7×10^{-14} erg s^{-1} cm^{-2}	44%	>85%
$\mathcal{L}_{\text{ext}} \geq 15$	267	0.33	2×10^{-14} erg s^{-1} cm^{-2}	47%	>90%

A. Liu+2022 (eFEDS)

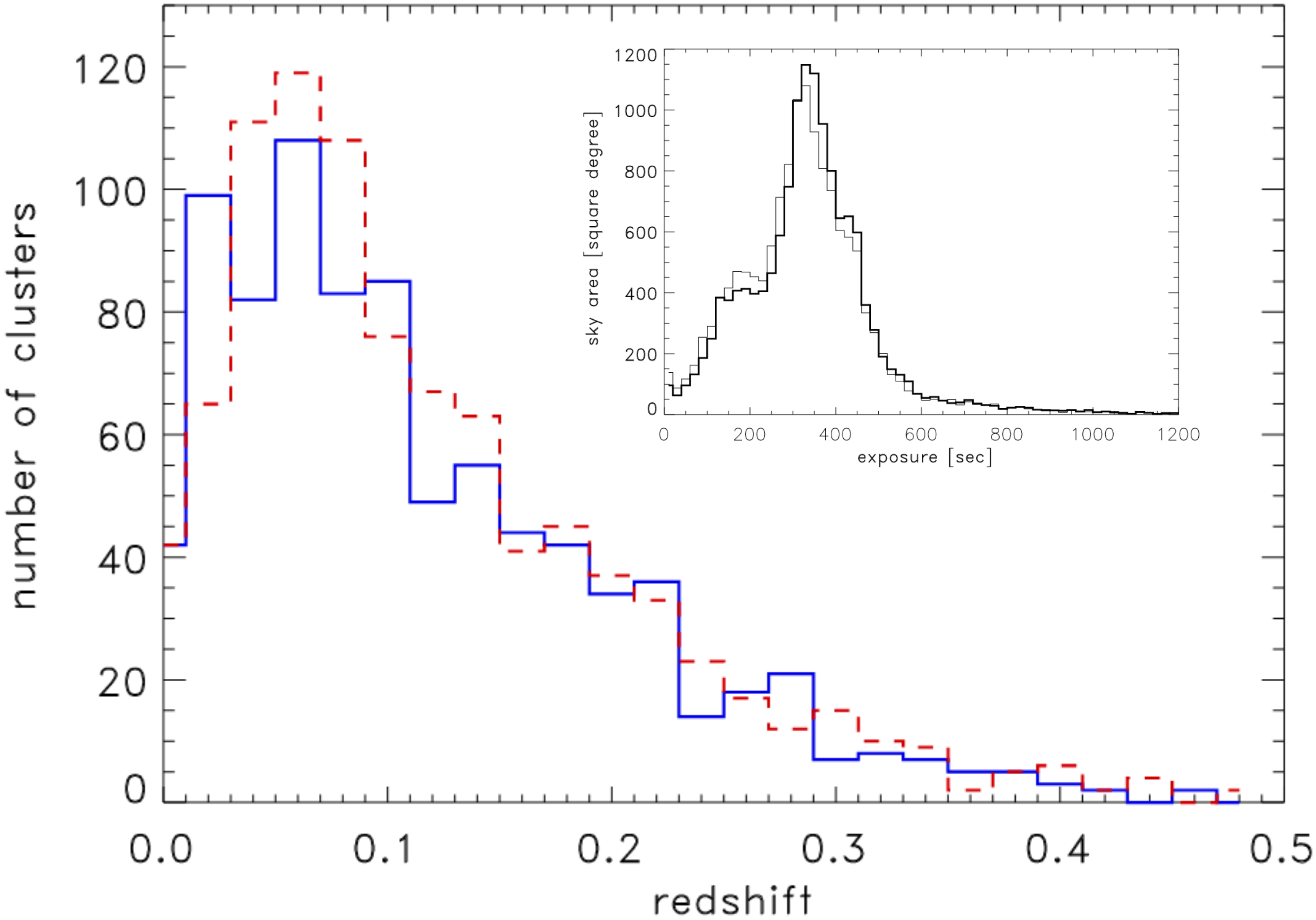

Figure 8. Redshift distribution of the NORAS II clusters (solid line). This function is compared to that of the REFLEX II sample (dashed line).

PSF~1.5 arcmin

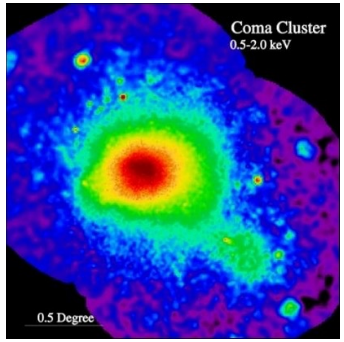

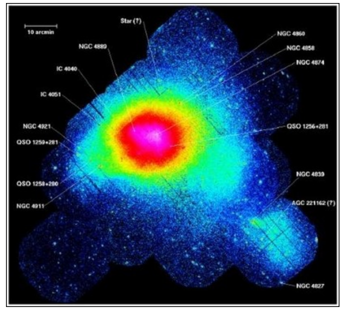

Böhringer+: NORAS (860 obj)+RELEX II (910 obj)

From RASS @flux limit of 1.8e−12 erg/s/cm^2 (0.1–2.4 keV)

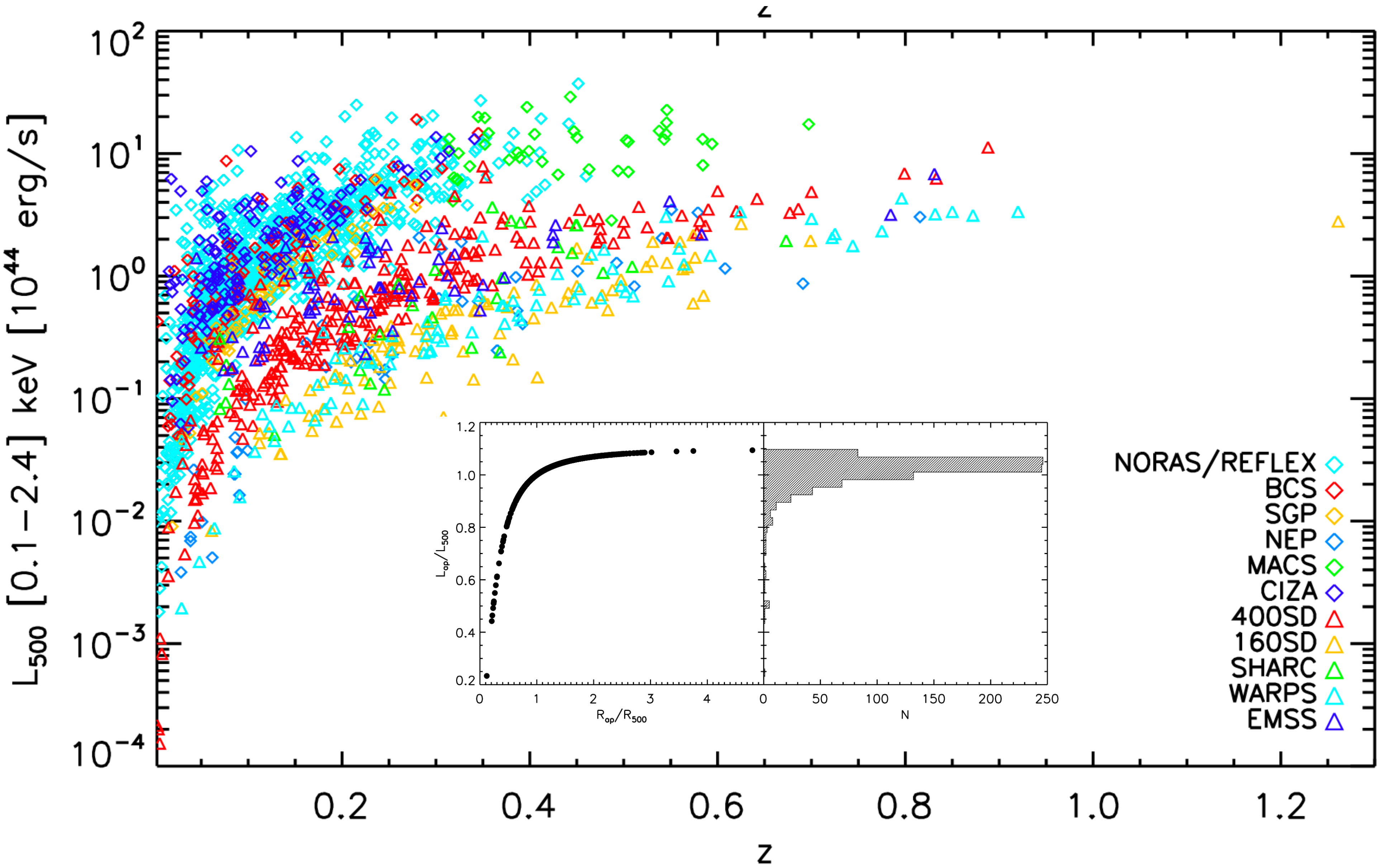

MCXC (Piffaretti+11): 1743 entries; MCXC2021 (in prep.)

➔ M2C (X-ray &SZ) Database: https://www.galaxyclusterdb.eu/m2c/

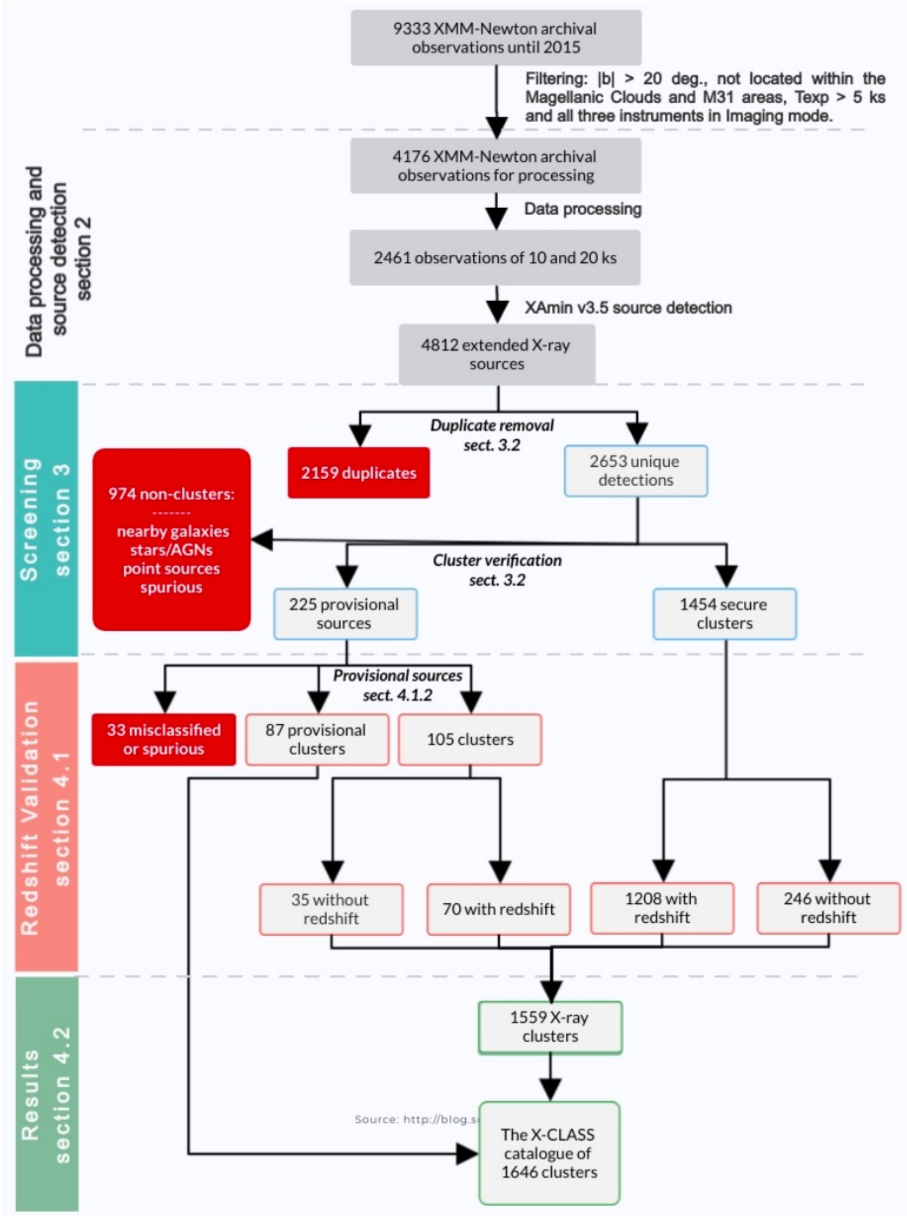

Fig. 1. Flowchart of the overall procedure for the compilation of the new X-CLASS cluster catalogue. Red filled frames contain the sources that were discarded.

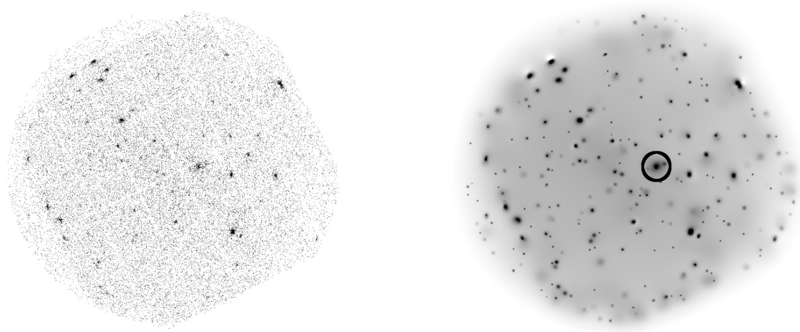

Fig. 3. X-ray image in the [0.5 – 2] keV X-ray band of a 10 ks *XMM-Newton* observation (left panel, mosaic of all three XMM-newton detectors) and the corresponding wavelet filtered image (right panel). The images are not background-subtracted and their diameter is 26′. The circle marks the position of a detected cluster candidate. Similar images are available for all X-CLASS clusters in the public database.

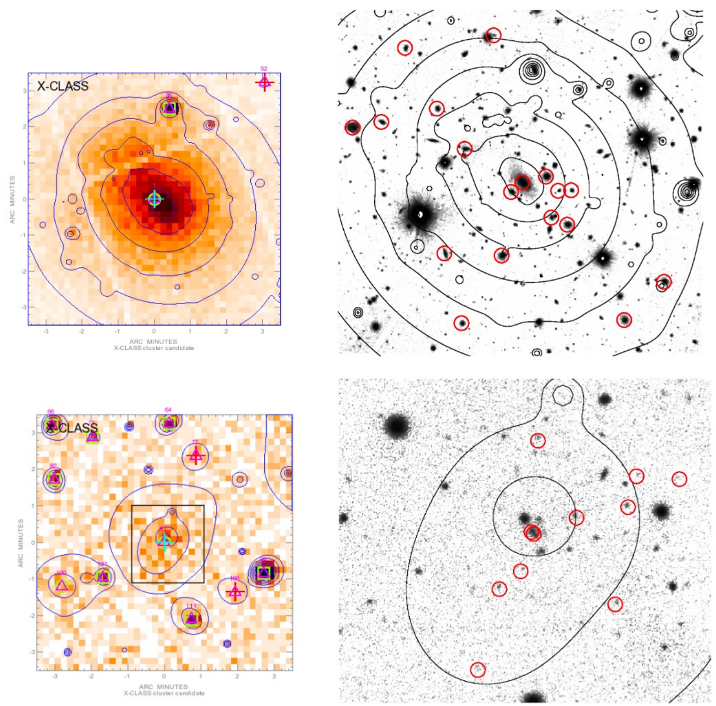

Fig. 4. Examples of X-ray selected galaxy clusters in the X-CLASS survey. Top panels: cluster Xclass0561 (ABELL 2050) at z=0.119 as confirmed by 19 member galaxies. Bottom panels: cluster Xclass0219 at z=0.791 as confirmed by 11 member galaxies. Left panels: X-ray images and contours. Green circles (squares) mark detections of extended (point-like) sources as classified by the XAmin pipeline. Straight lines that cross the image are CCD gaps of the XMM-Newton detector. Right panels: i-band optical images from PanSTARRS over-plotted with X-ray contours. Red circles mark the member galaxies with available spectroscopic redshift. In the case of Xclass0561 both X-ray and optical image cover the same sky area, while in the case of Xclass0219 the optical image corresponds to the central region of the X-ray image marked with the black square.

Koulouridis+21, X-CLASS, 1646 obj @z<1.5

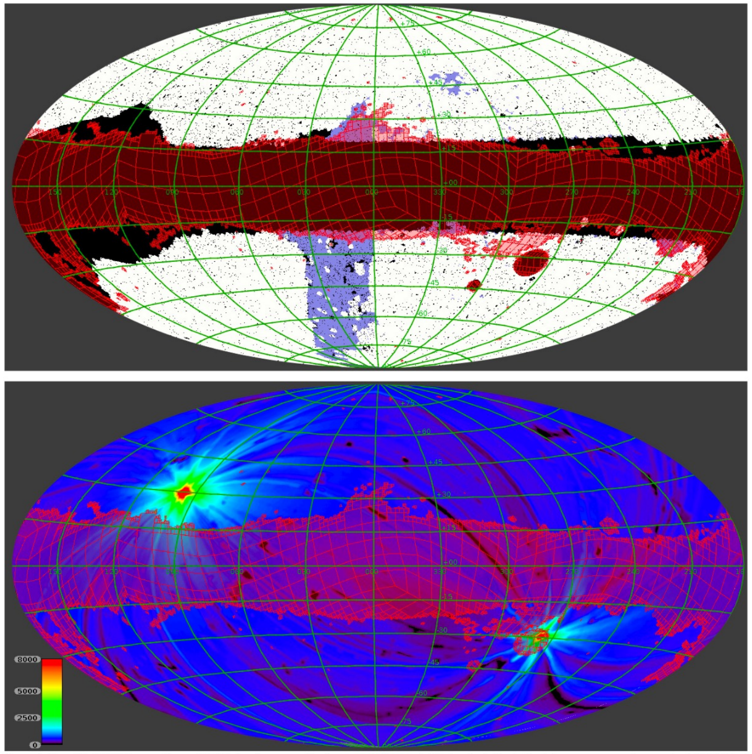

Figure 1. Top: The DESI Legacy Survey DR10 showing extragalactic coverage in grz (white) and gi (blue). Both datasets are supplemented with WISE $w1$ and $w2$ photometry. Bottom: The ROSAT All-Sky Survey exposure map from the 2RXS source catalog is drawn. Highlighted in red are sky regions impacted by high galactic NH column densities ($N_H > 10^{21}$ cm^{-2}) or high stellar densities and therefore less suited for cluster search.

Klein+23: MARDELS catalog of 8,471 X-ray selected galaxy clusters over 25,000 deg^2; deep, multiband optical imaging data +optical counterpart classification algorithm MCMF +DESI Legacy Survey DR10 catalog +ROSAT All-Sky-Survey source catalog (2RXS)

➔ **90% pure MARDELS catalog**, *the largest ICM-selected cluster sample to date*

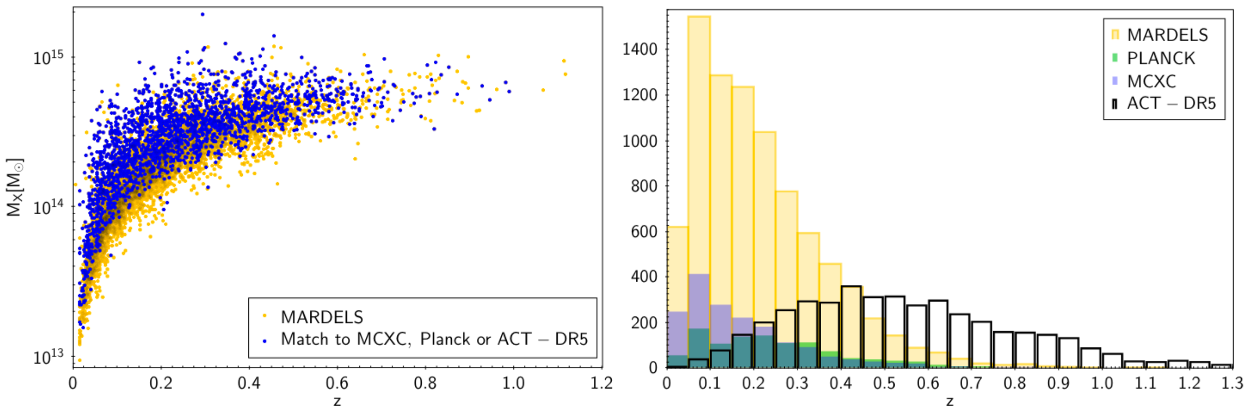

Figure 8. Left: X-ray mass proxy M_X versus redshift for the 90% pure MARDELS sample. Highlighted in blue are matches to the MCXC, Planck PSZ2 and the ACT-DR5 cluster catalogs. Right: Redshift distribution of the 90% pure MARDELS sample, as well as for MCXC, Planck PSZ2 and the ACT-DR5. The MARDELS catalog contains more clusters per redshift interval (dN/dz) than ACT-DR5 out to $z \sim 0.4$ and more clusters overall than all three external cluster surveys put together.

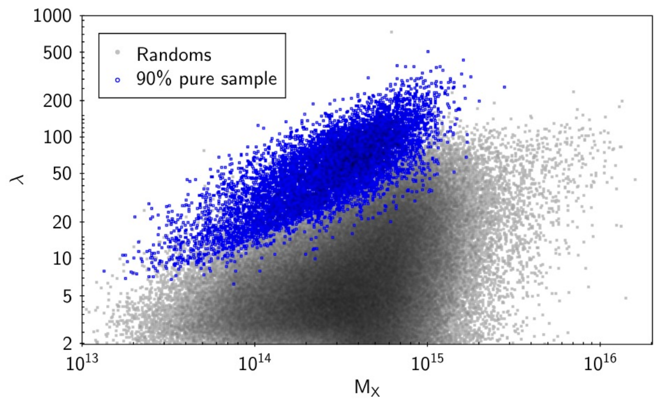

Detection through cluster outskirts

(Kafer+20, Xu+18): outperform standard method (***erbox*** sliding-box algorithm to detect peaks in the input count images) for extended (>80”) sources

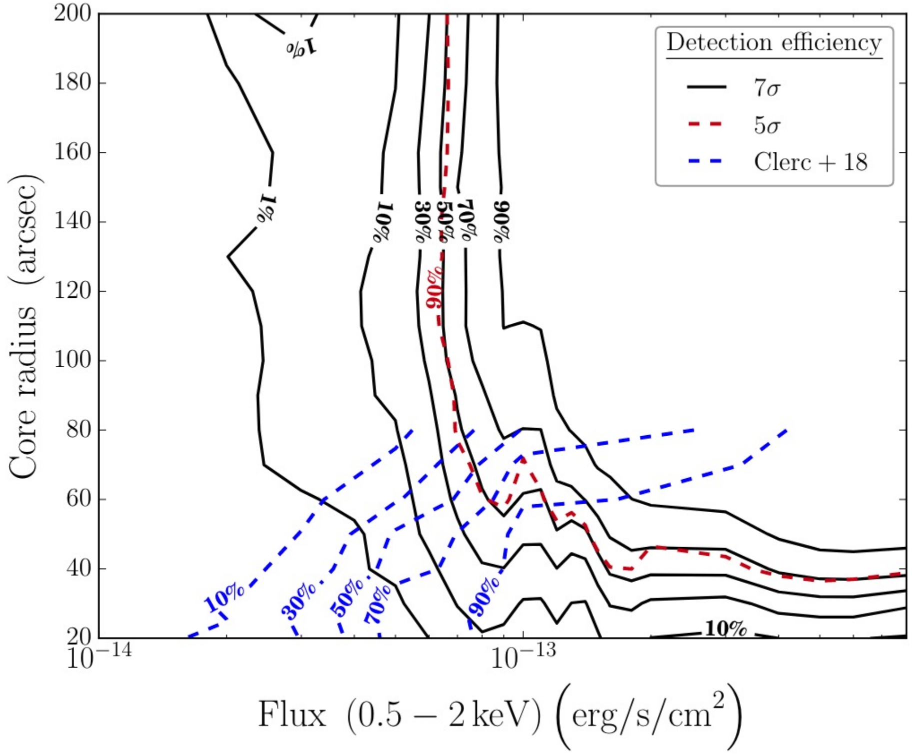

Fig. 7. Extended source detection efficiency of our maximally clean (7σ threshold, black contours), our 5σ threshold (brown contour), and the Clerc et al. (2018) threshold (blue contours) in the core radius vs. input flux plain for an equatorial eROSITA survey field of approximately 1 ks exposure.

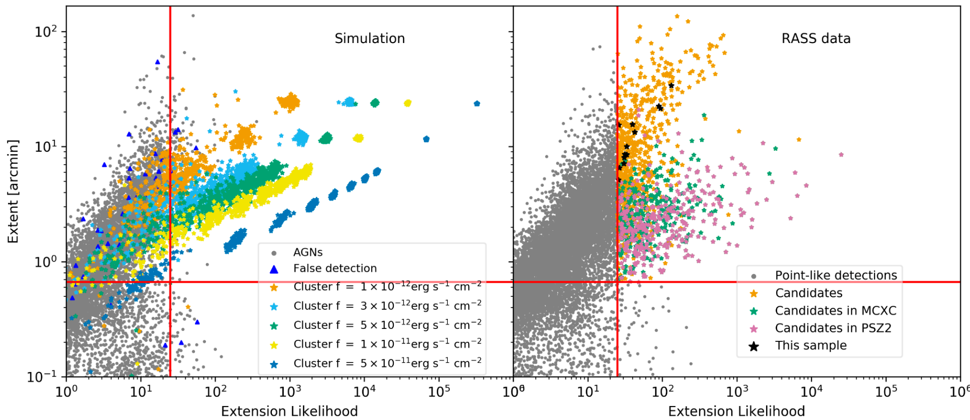

Fig. 1. Selection criteria for extended sources. The selection is performed in the extension likelihood - extent plane. The red-solid lines define the optimal parameters obtained from simulations to characterize extended sources. *Left*: simulation results. Gray dots represent simulated AGNs, and blue triangles, false detections. Colored stars represent clusters with different input fluxes. *Right*: results from reprocessing RASS data. Gray dots stand for point-like detections and the star symbols for the cluster candidates. Green and pink stars show the candidates with identified counterparts in the MCXC and PSZ2 catalogs, respectively. The black stars represent the 13 groups of our pilot sample described in Table 3.

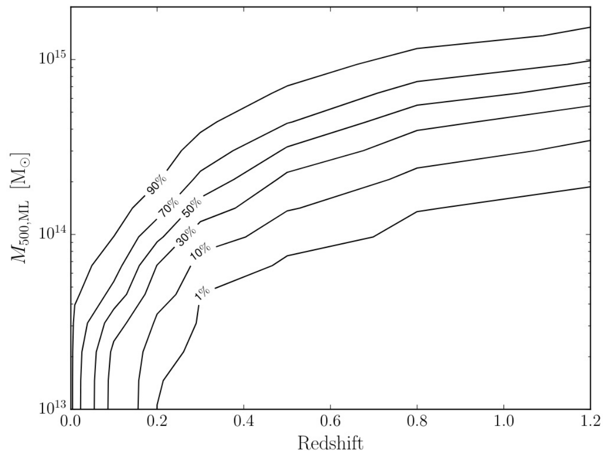

Fig. 8. Maximally clean (7σ) extended source detection efficiency (black contours) in the mass vs. redshift plain for an equatorial eROSITA survey field of approximately 1 ks exposure.

On SZ selection

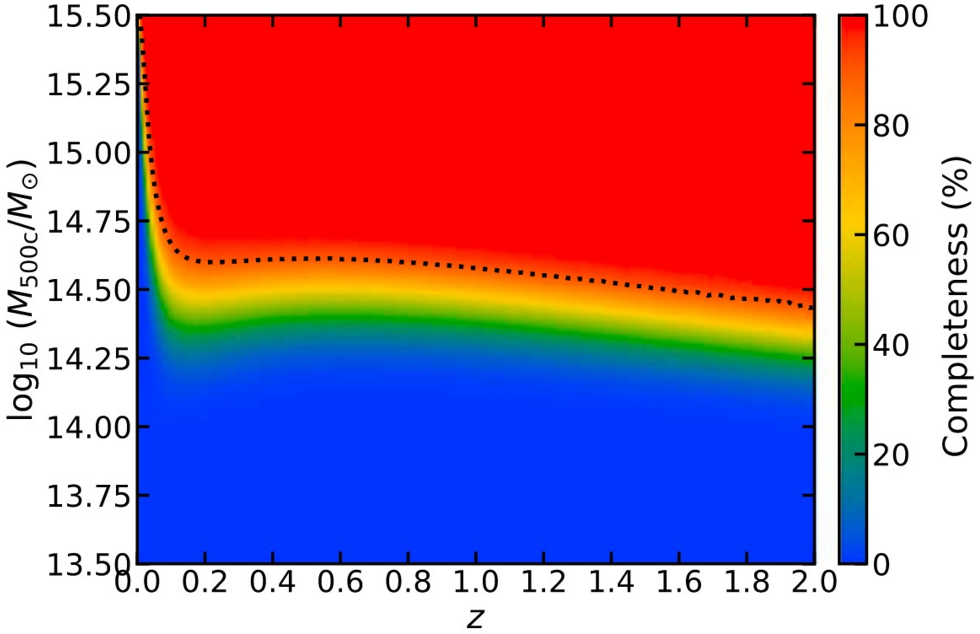

Figure 7. Completeness for $S/N_{2.4} > 5$ as a function of redshift, in terms of M_{500c}^{UPP}, over the full 13,211 deg^2 survey footprint. The Tinker et al. (2008) halo mass function and Arnaud et al. (2010) scaling relation are assumed (see Section 2.4). The dashed black contour marks the 90% completeness limit.

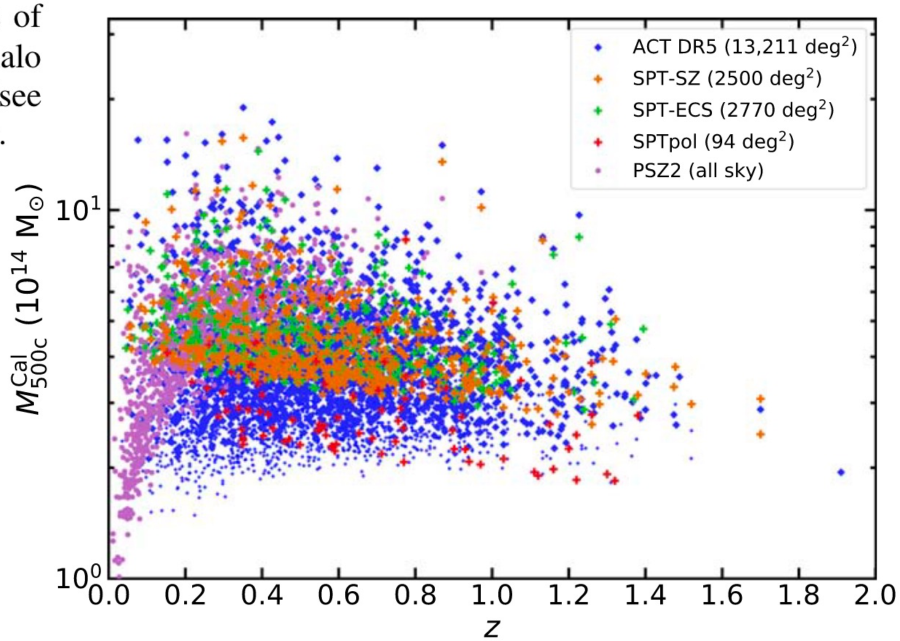

ACT, Hilton+21

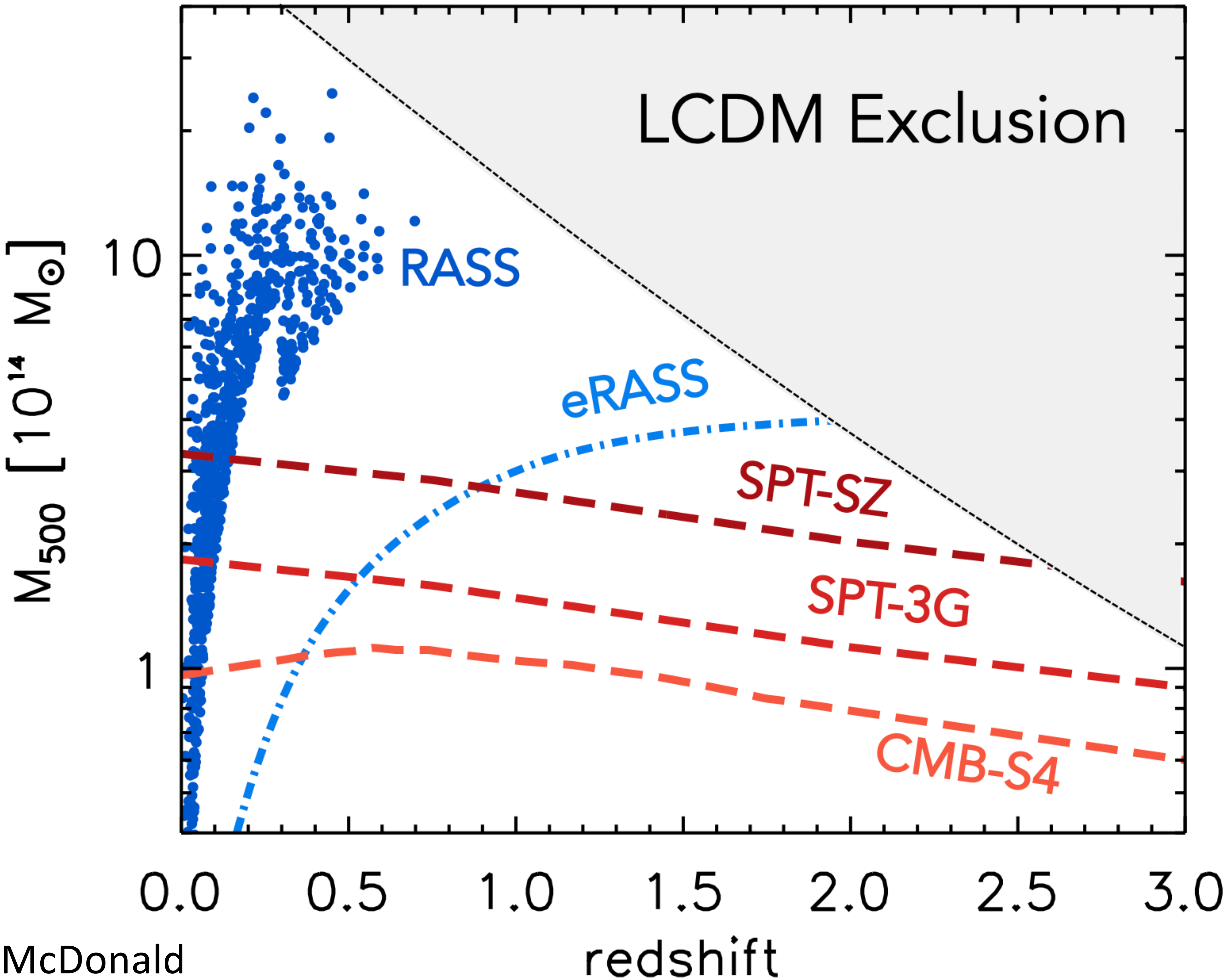
LCDM Exclusion
RASS
eRASS
SPT-SZ
SPT-3G
CMB-S4
M_{500} [10^{14} $M_\odot$]
10
1
0.0
0.5
1.0
1.5
2.0
2.5
3.0
redshift

@McDonald

Scaling laws & selection biases

X-ray flux-limited samples suffer from two forms of selection bias, ***Malmquist bias***, where higher luminosity clusters are detectable out to higher redshifts and so occupy a larger survey volume, and ***Eddington bias***, where in the presence of intrinsic/statistical scatter in L for a given M, objects above a flux limit will have above-average luminosities for their mass. Due to the steep slope of the cluster f(M), the Eddington bias is amplified, resulting in a net movement of lower mass objects into a flux-limited sample.

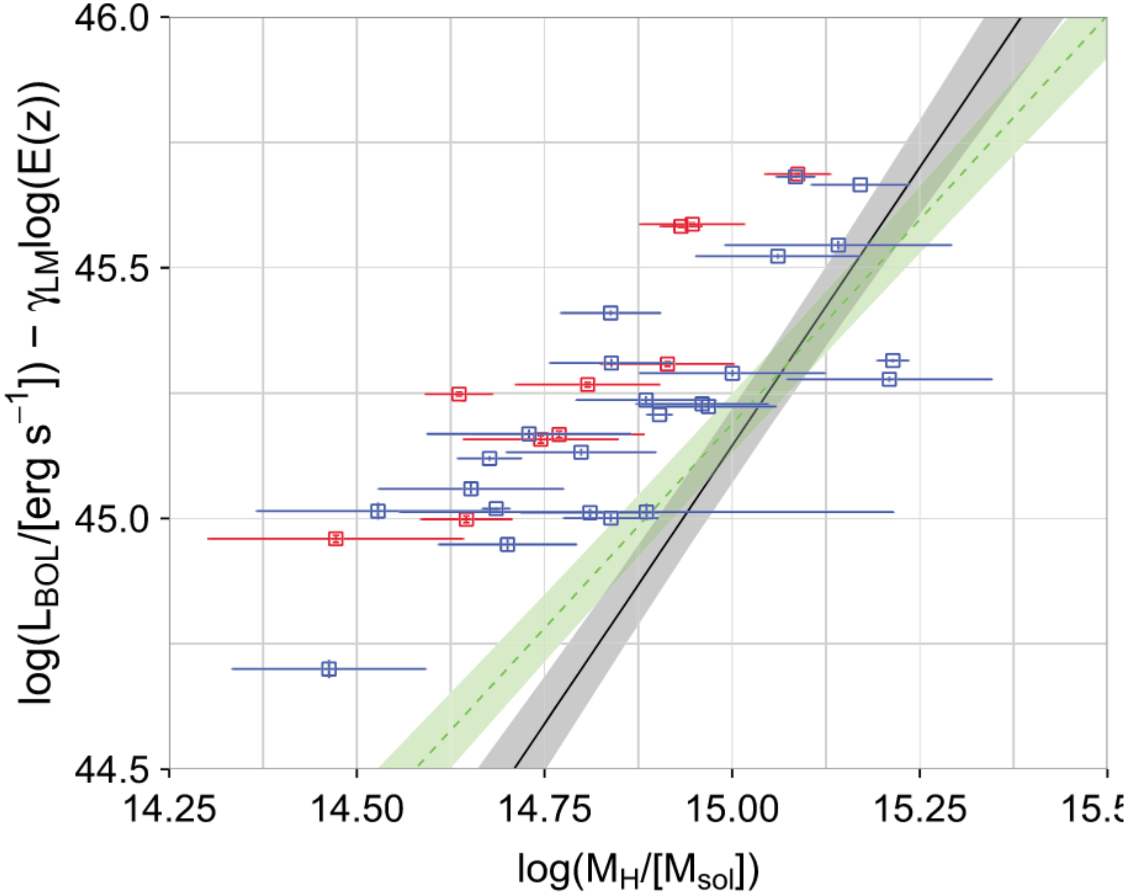

From Giles+17: neglecting selection effects in the sample would lead to a 40% underestimate in the mass for a given L.

The solid line in this plot is the estimated relation when selection effects are accounted for. Red/blue points represent relaxed/disturbed systems. The green line and shaded area represent the best-fitting relation of Mantz+10 and the corresponding 1σ uncertainty

Scaling laws & selection biases

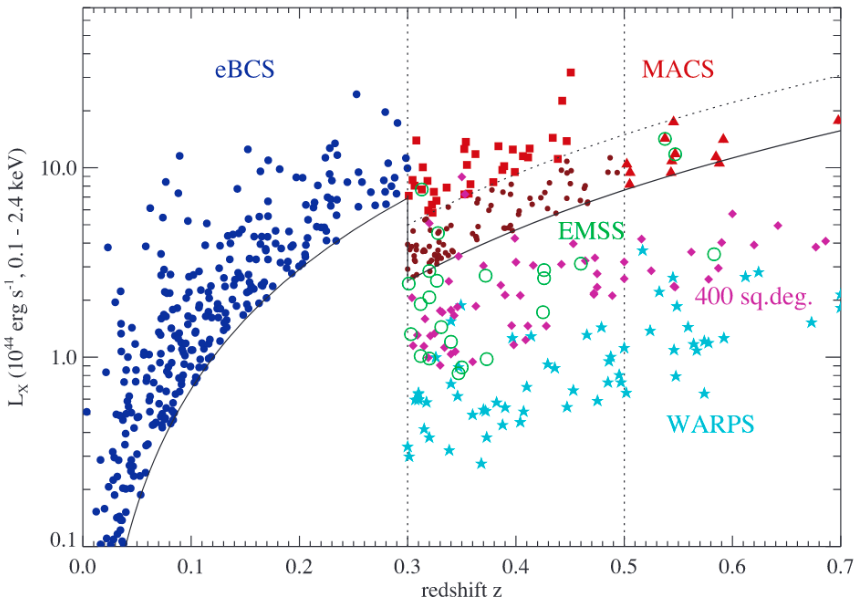

Figure 2. L_X–z distribution of clusters from various X-ray-selected samples. By design, MACS finds the high-redshift counterparts of the most X-ray luminous (and best-studied) clusters in the local Universe. Note also how MACS selects systems that are typically about 10 times more X-ray luminous, and thus much more massive, than those found in deeper serendipitous cluster surveys such as the EMSS, WARPS or the 400 deg^2 project. Two subsets of the MACS sample are highlighted: the sample presented here (red squares) and the 12 most distant MACS clusters at $z > 0.5$ (red triangles; Ebeling et al. 2007). A ΛCDM cosmology ($\Omega_M = 0.3, \Lambda = 0.7, h_0 = 0.7$) has been assumed.

Ebeling+01: MACS, based on RASS Bright Source Catalogue (BSC; Voges+99)

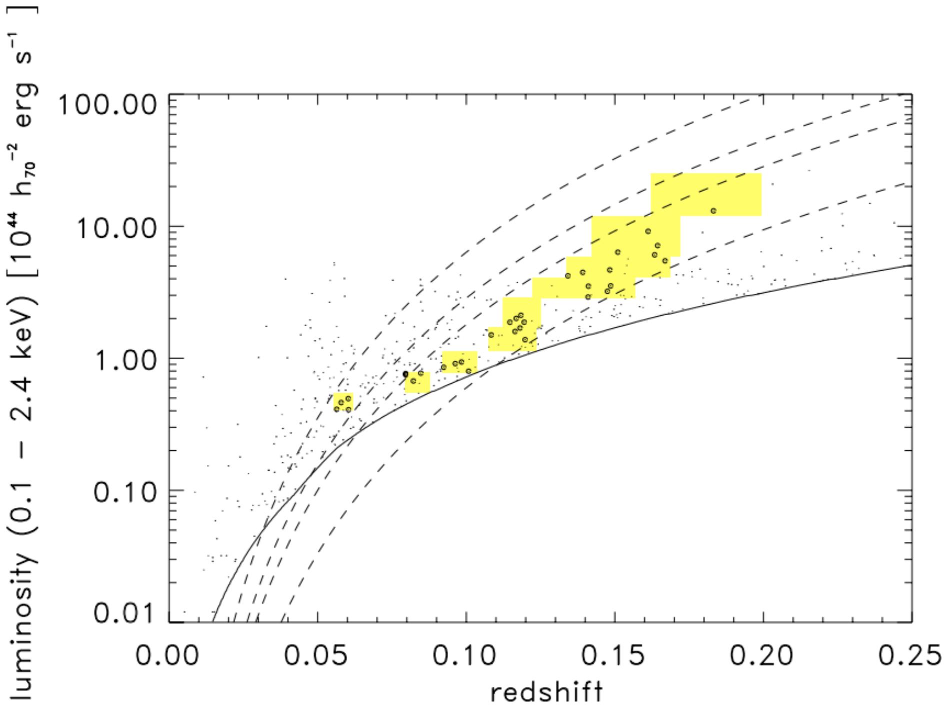

Fig. 1. X-ray luminosity-redshift distribution of the REFLEX sample (small dots: entire REFLEX sample including clusters with less than 30 cts and $N_H > 6 \times 10^{20}$ cm^{-2}), and the representative subsample (encircled dots) selected from the regions marked by colored boxes. The solid line indicates the survey flux limit. The dashed lines show the distances at which r_{500} is 7, 9, 10, and 12 arcmin (*from right to left*), for given X-ray luminosity, respectively.

Böhringer+07: The representative XMM-Newton cluster structure survey (**REXCESS**) of an *X-ray luminosity selected* galaxy cluster sample

An XMM-Newton Multi-Year Heritage Program

Witnessing the culmination of structure formation in the Universe

URL: xmm-heritage.oas.inaf.it

CHEX-MATE (the Cluster HEritage project with XMM-Newton: Mass Assembly and Thermodynamics at the Endpoint of structure formation): **3 Msec** over the period 2018-22 to survey ***homogenously*** 118 Planck-SZ selected objects (**SNR>6.5; z ∈ [0.05, 0.6]; M_{Tier-2}>7.25e14**) comprising an unbiased census of:

- *the population of clusters at the most recent time (z < 0.2)*
- *the most massive objects to have formed thus far in the history of the Universe*

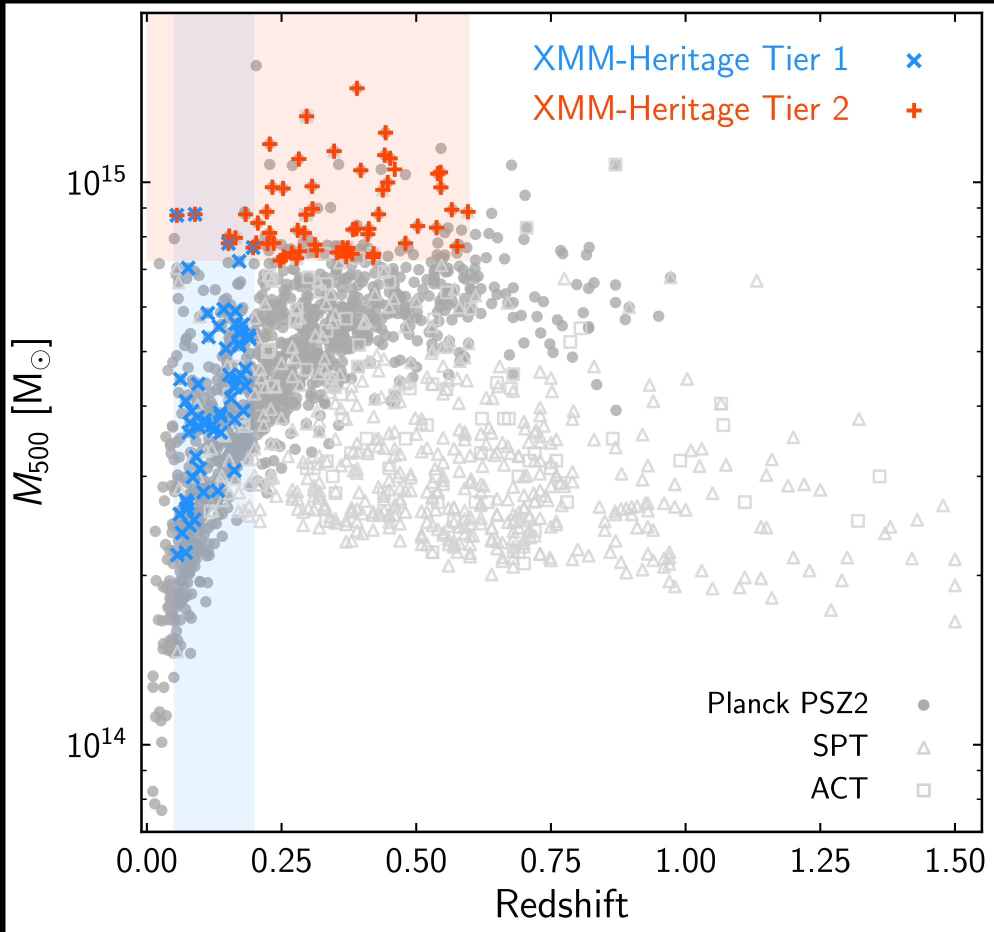

CHEX-MATE gallery *2021, A&A, 650, 104*

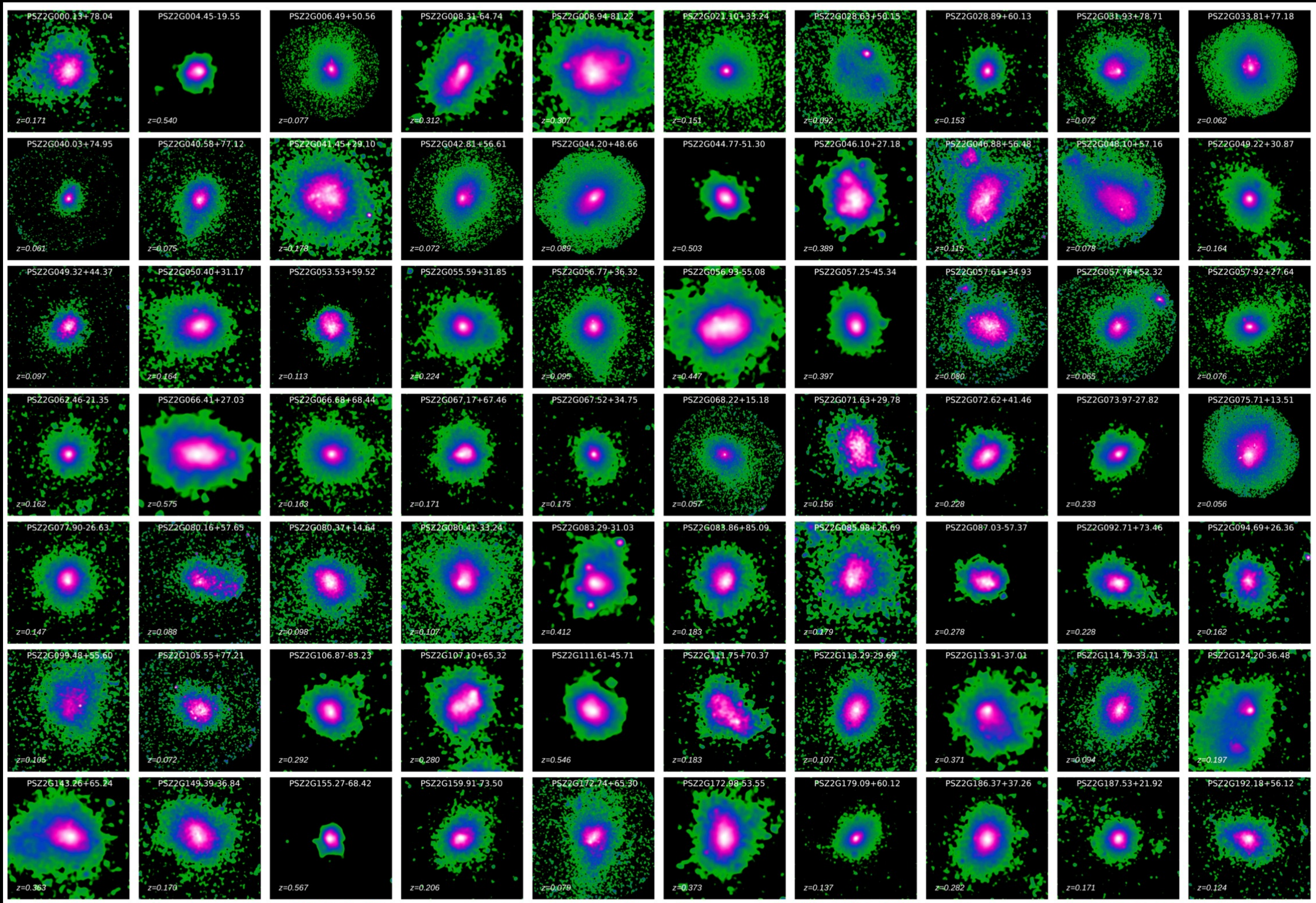

X-ray morphology
(Campitiello+22 A&A 665 117)

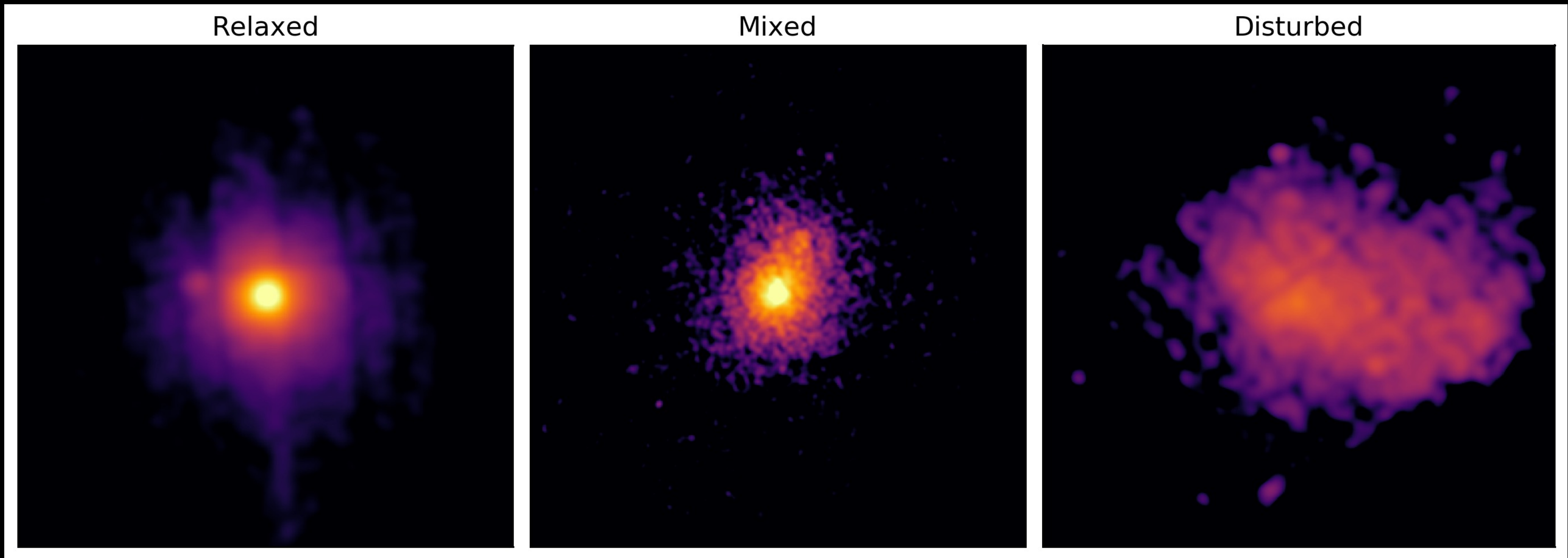

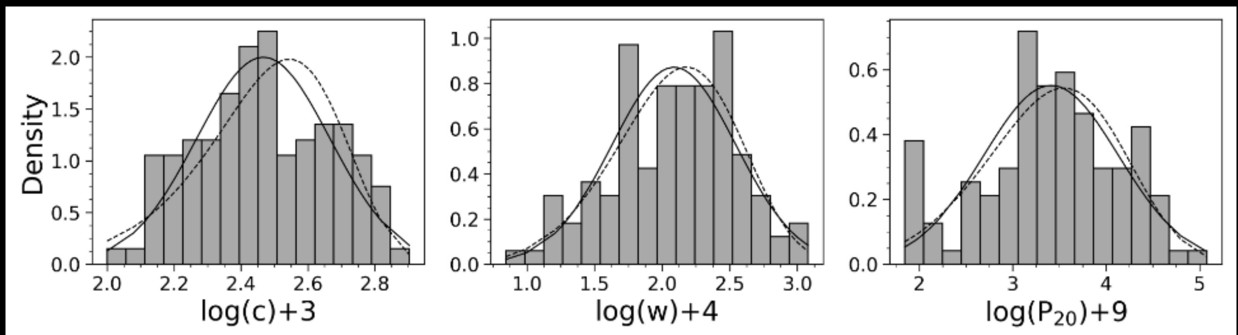

Distributions of morphological parameters is preferentially log-normal and do not show any bimodality

X-ray morphology
(Campitiello+22 A&A 665 117)

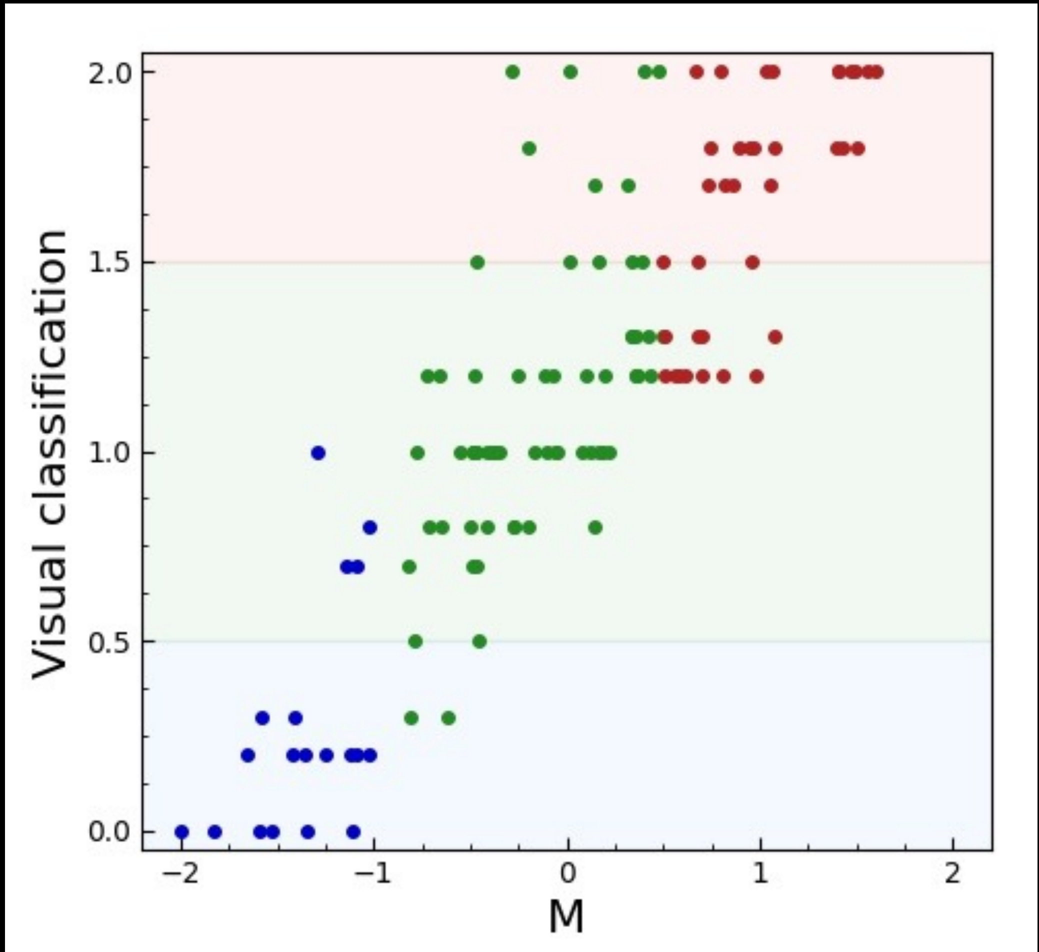

$$M = \sum \frac{\log_{10}(Par^{\alpha_{Par}}) - < \log_{10}(Par^{\alpha_{Par}}) >}{\sigma_{log_{10}(Par^{\alpha_{Par}})}}$$

- We compress all morphological info into the parameter M
- *15 (13%) very relaxed & 27 (23%) very disturbed objects*
- We confirm that SZ selected sample contains more disturbed systems than X-ray selected ones

The most massive clusters at high-z

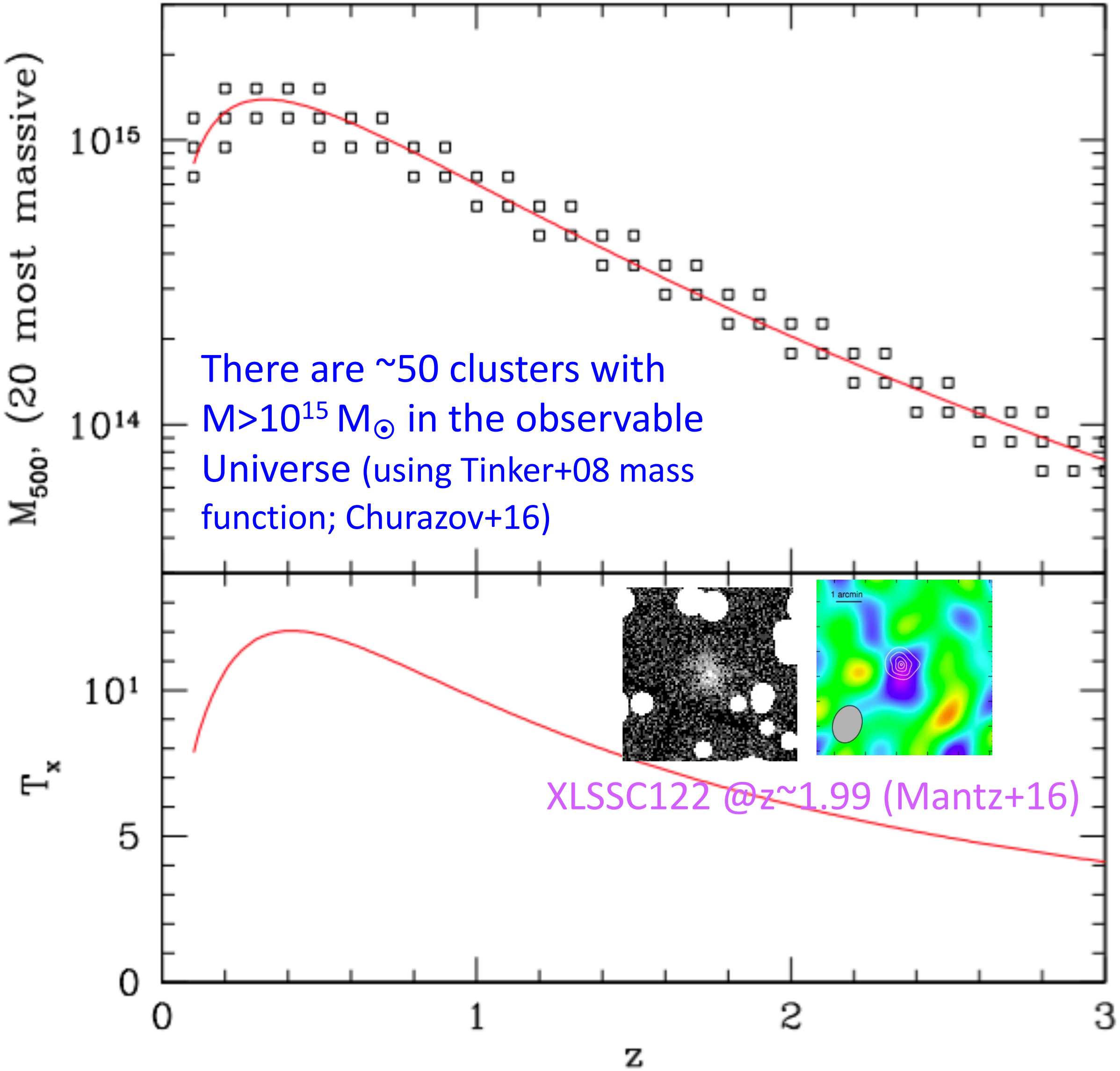

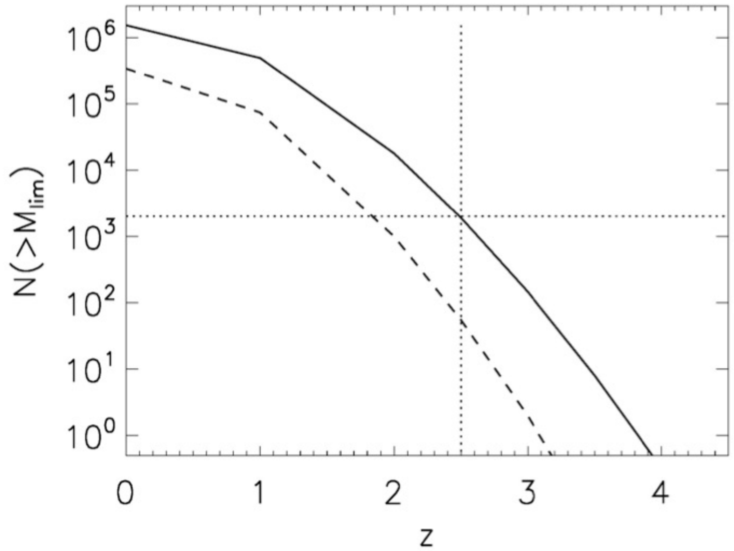

Number of objects with $M_{500}/M_{\odot}$ > 5e13 (solid; >1e14 dashed): 1900 (WMAP9; 5000 using Planck13) are expected at z>2.5 (full sky; 1 per 22 deg^2; Reiprich+)

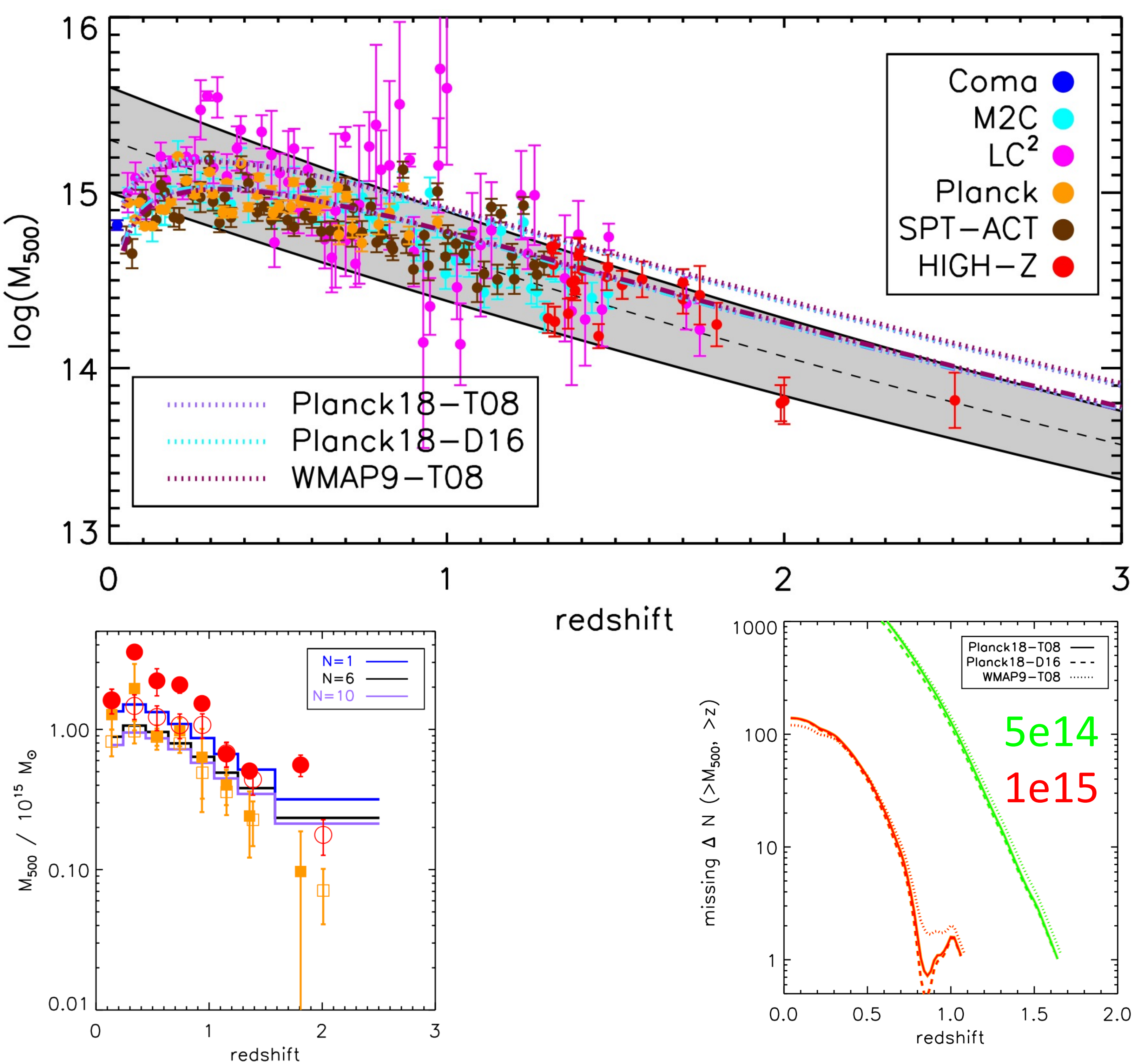

Coma
M2C
LC²
Planck
SPT−ACT
HIGH−Z
Planck18−T08
Planck18−D16
WMAP9−T08
log(M500)
redshift
N=1
N=6
N=10
M500 / 10^15 M⊙
missing Δ N (>M500, >z)
5e14
1e15

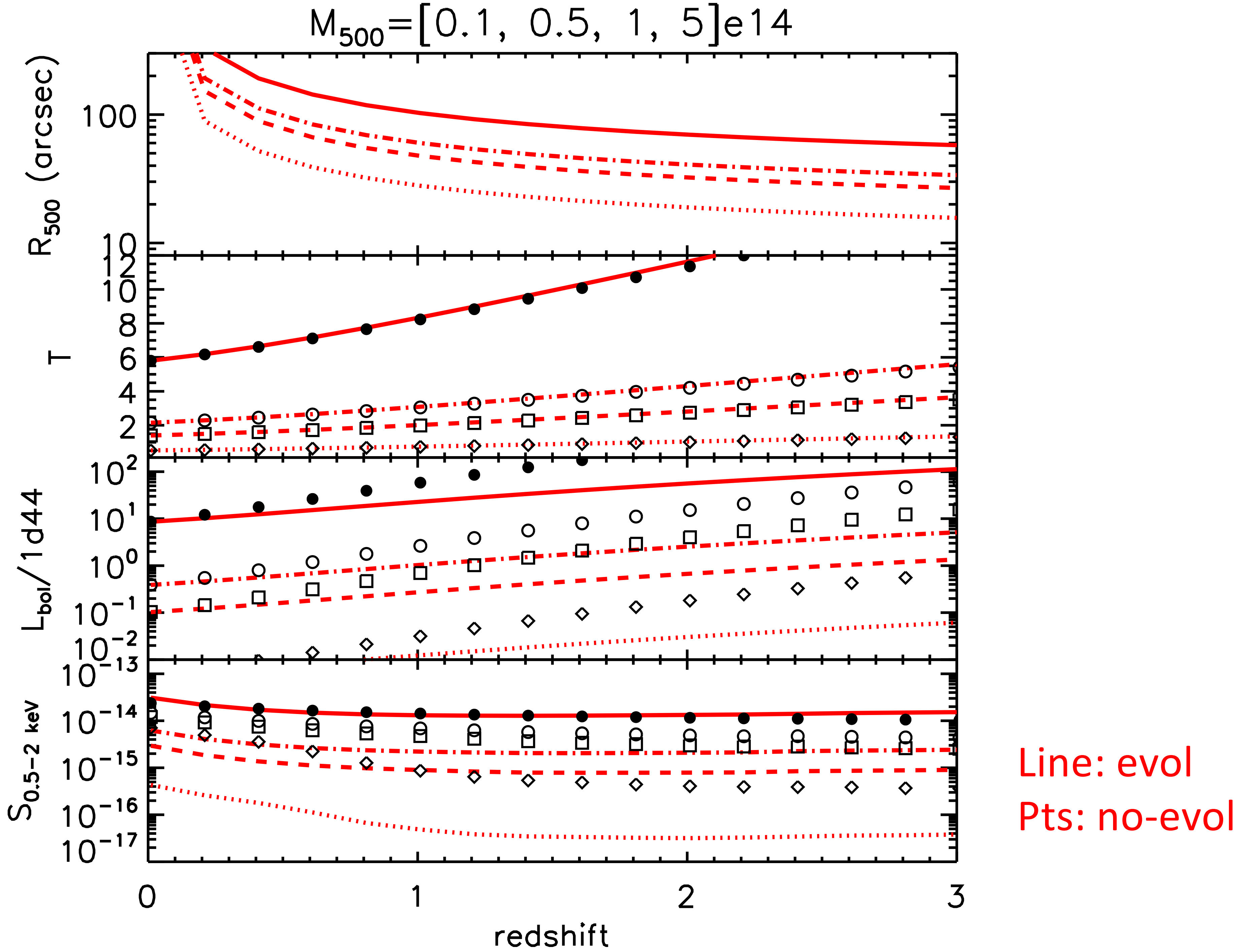

M500=[0.1, 0.5, 1, 5]e14
R500 (arcsec)
100
10
T
12
10
8
6
4
2
Lbol/1d44
10^2
10^1
10^0
10^-1
10^-2
S0.5-2 keV
10^-13
10^-14
10^-15
10^-16
10^-17
0
1
2
3
redshift
Line: evol
Pts: no-evol

Chandra data of high-z clusters

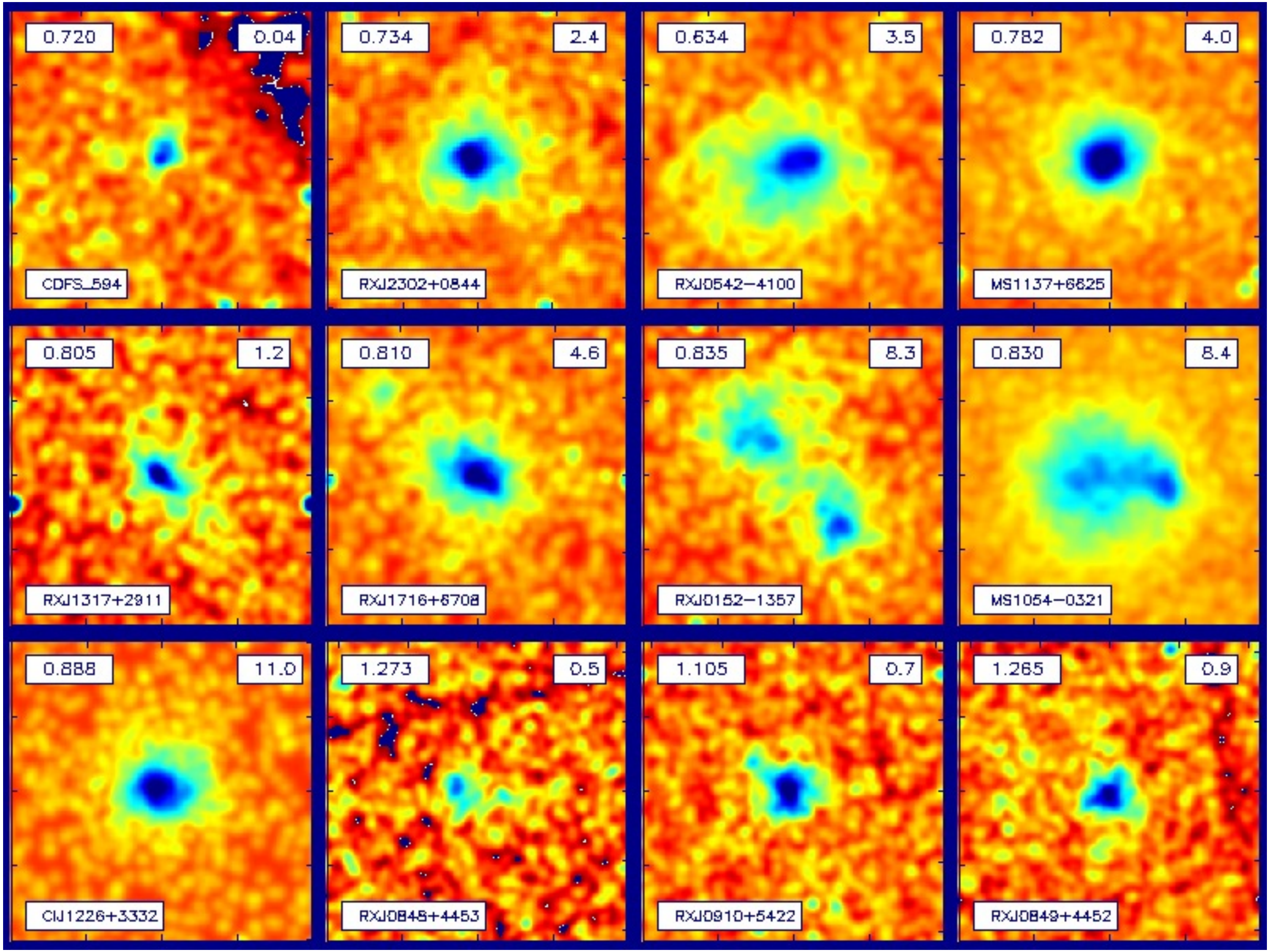

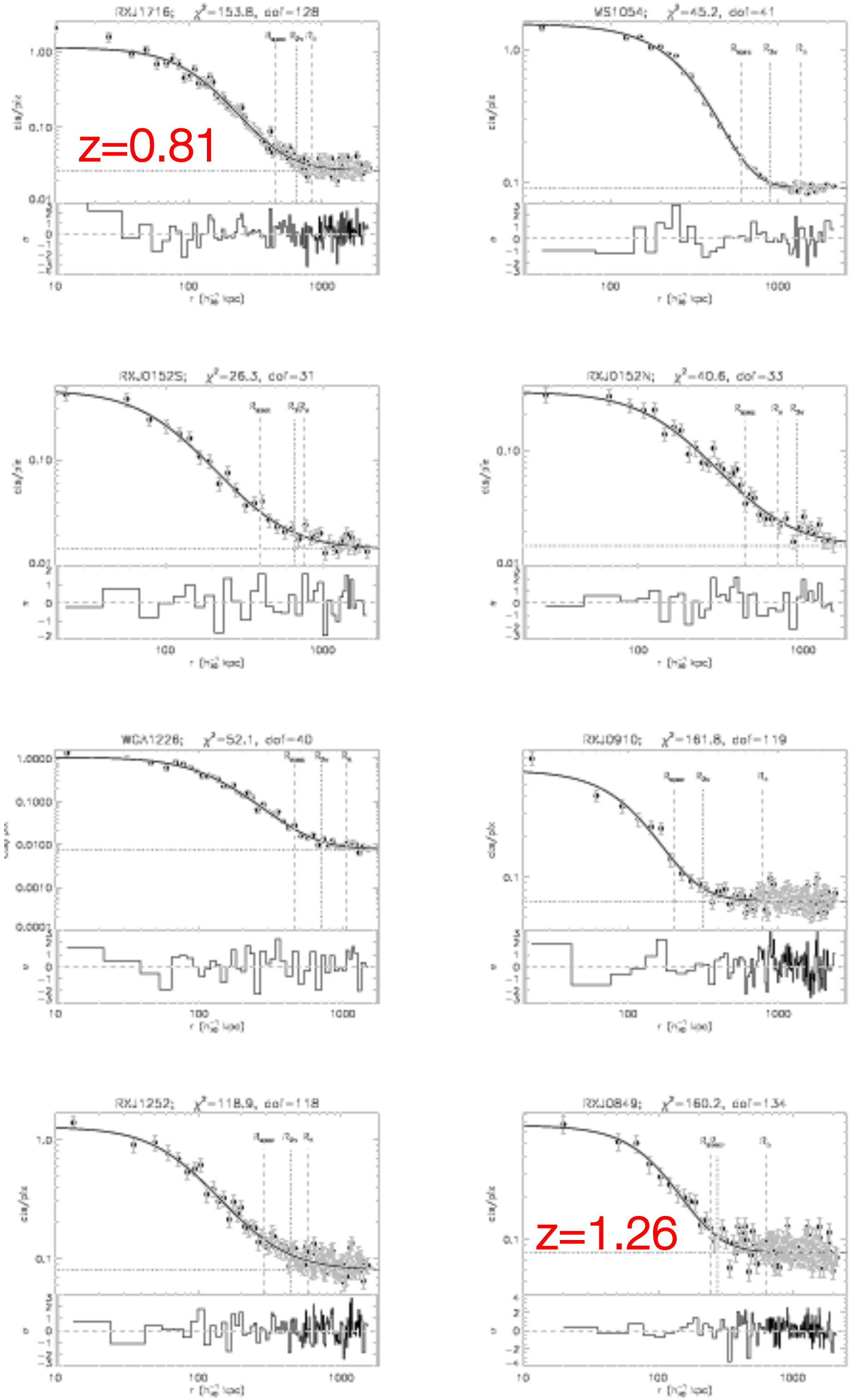

β-model reproduces quite well the surface brightness of these high-z clusters.

A single emission-weighted temperature is measurable.

The central density is obtained by deprojecting the normalization of the thermal model through the best-fit β-model.

(from Ettori+04; mostly from RDCS by Rosati+)

Two extreme cases: S_b & T_{ew}

z = 1.26

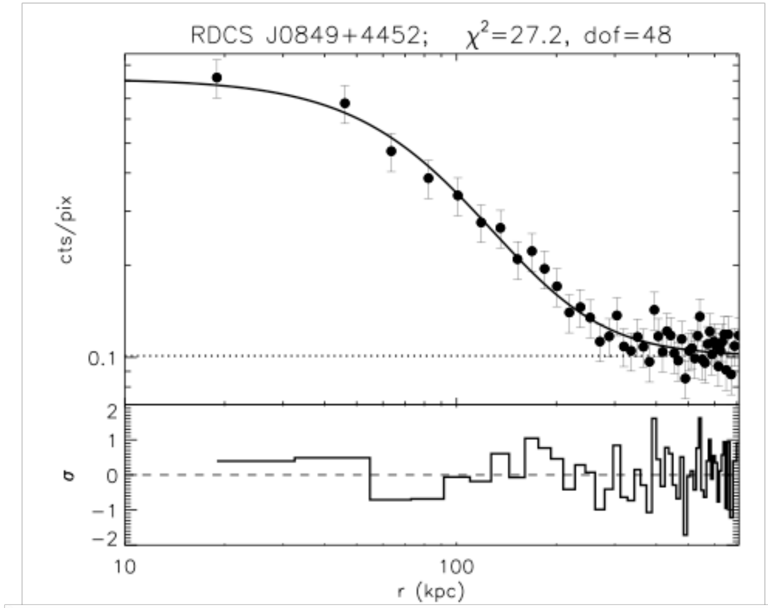

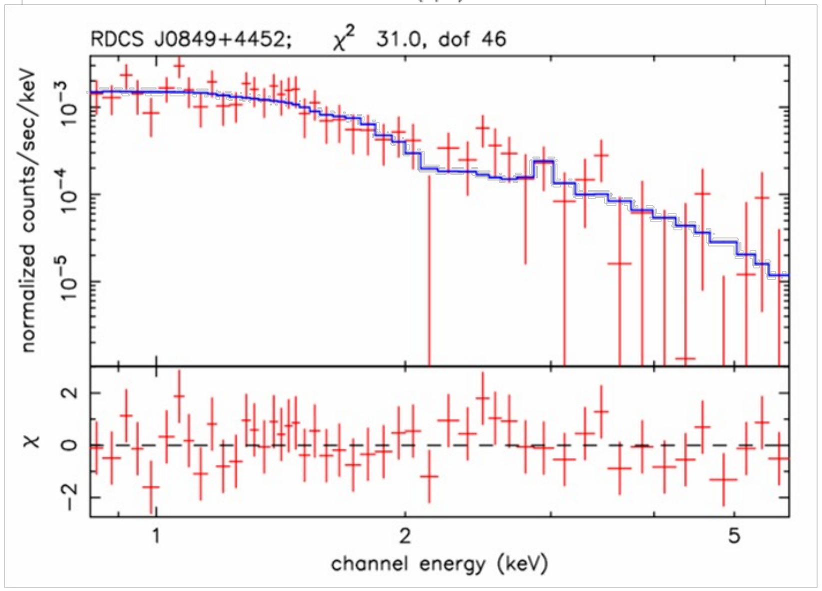

z = 1.10

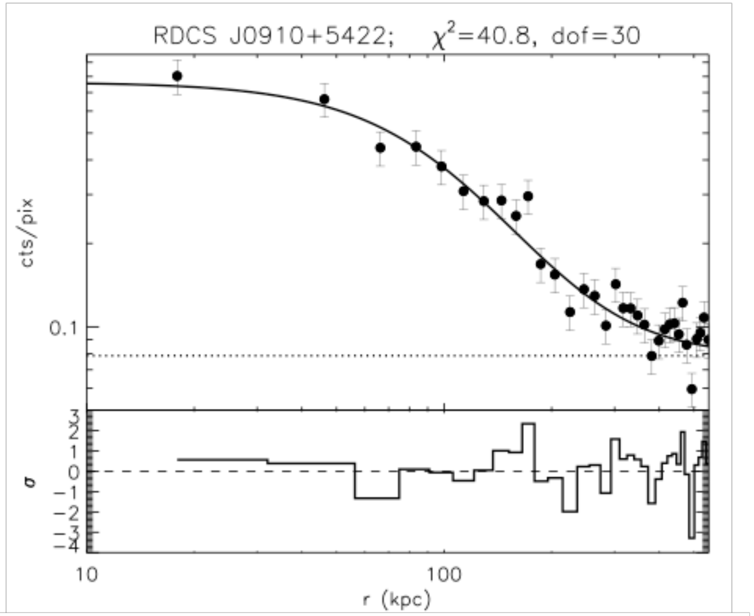

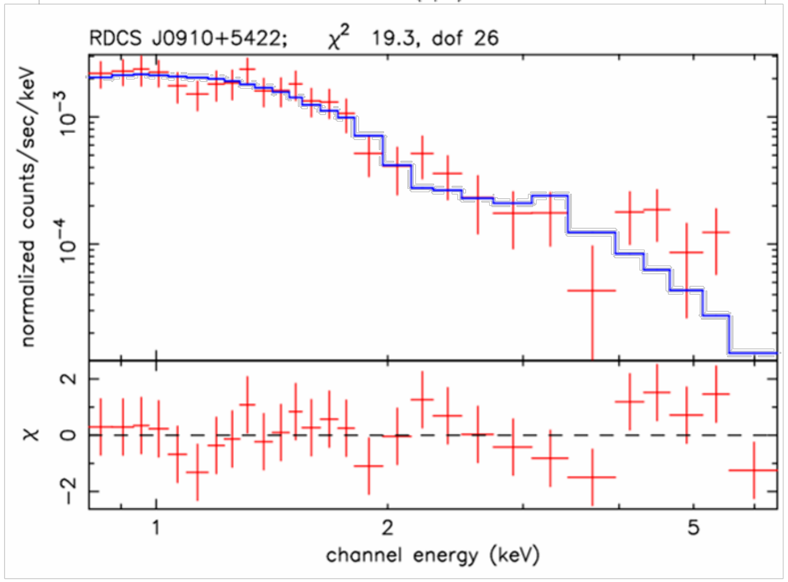

Evolution in the X-ray scaling laws

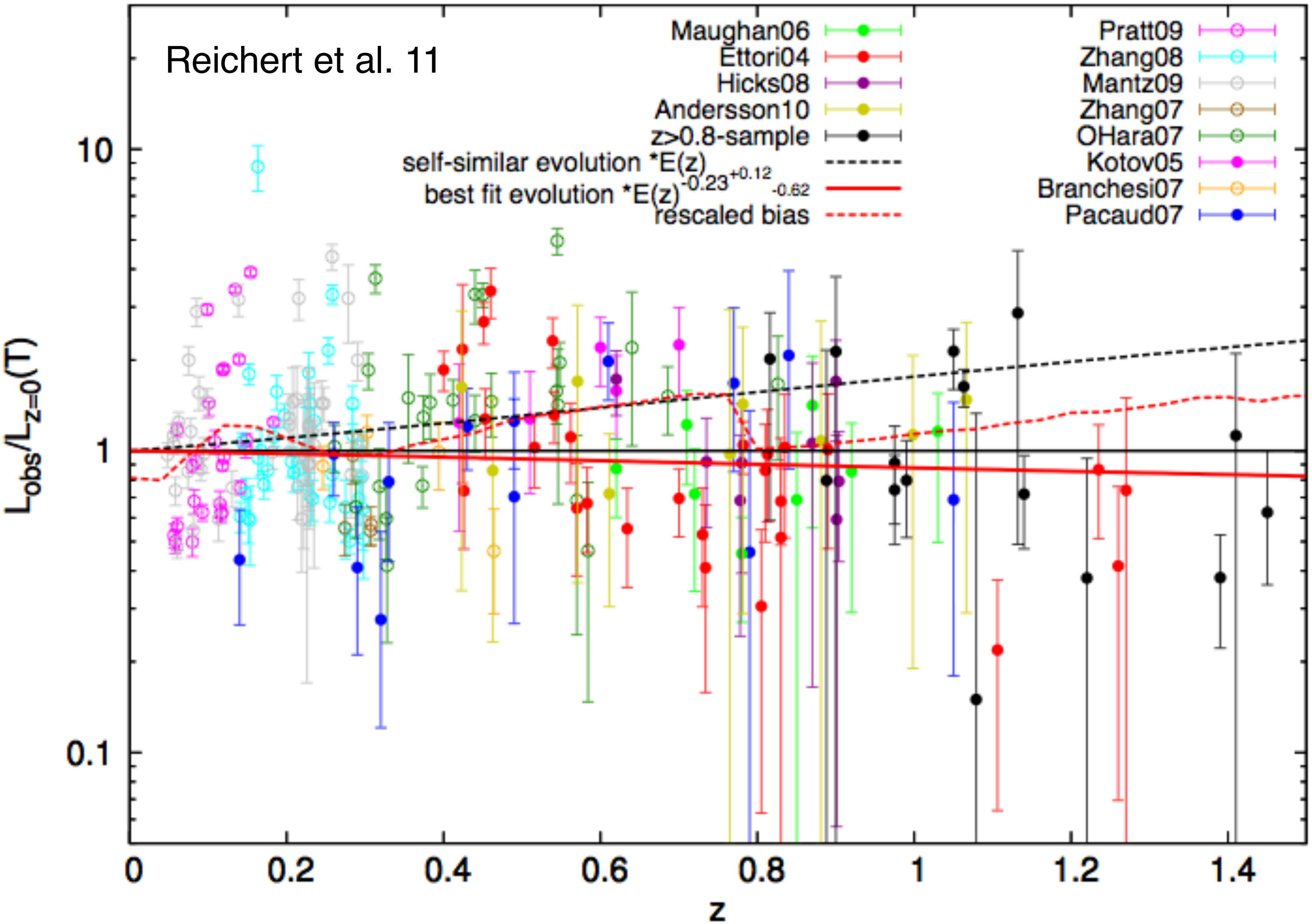

Dashed **(solid)** line: expected **(best-fit)** relation

Evolution in the X-ray scaling laws

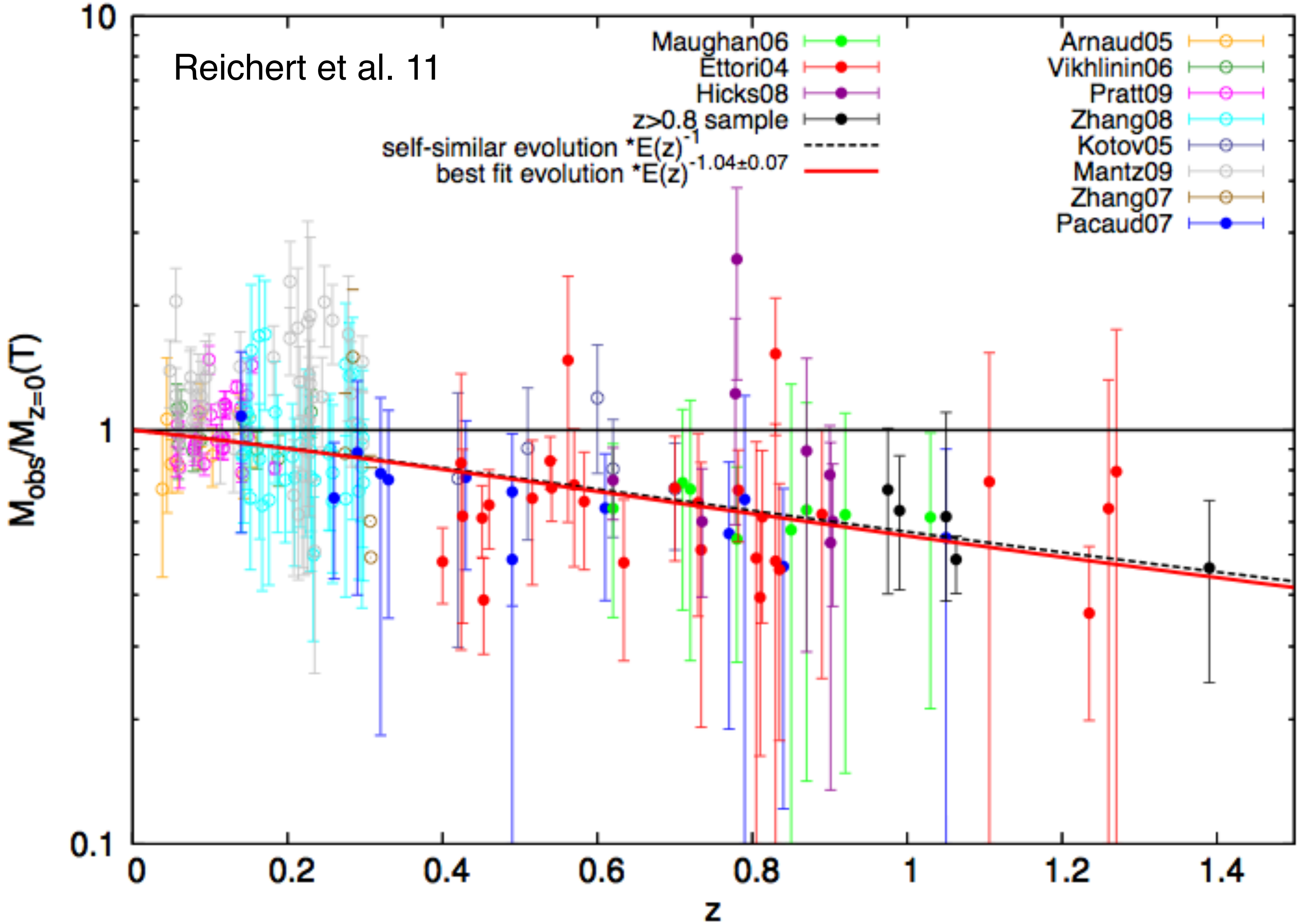

Dashed (solid) line: expected **(best-fit)** relation

Evolution of the X-ray scaling laws

• **No evolution, *apart from self-similar expectations*, is observed in M-T & M_{gas}-T & L-Y** The normalization in M – T/Y_X for nearby systems is lower (by ~20%) than the one predicted from simulations including cooling & galaxy feedback.

• **Negative evolution in L-T**: i.e. a slight decrease in L for given T at higher z is observed (*when cores are not excised*; *the entropy at 0.1 R_{200} is measured higher in systems at higher redshift)*

• ***eROSITA*** needs SLs to connect 10^5 (only 2% with T; ~100 @z>1.5) X-ray detected GCs to their mass

•**BTW**: let's agree to study it w.r.t. Ez = H_z / H_0; it is exactly equal to $(1 + z)^{1.5}$ in an EdS universe and proportional to $(1 + z)^{0.6/0.9}$ in the redshift range 0.4-1.3 for an assumed ΛCDM model with Ω_m = 0.3

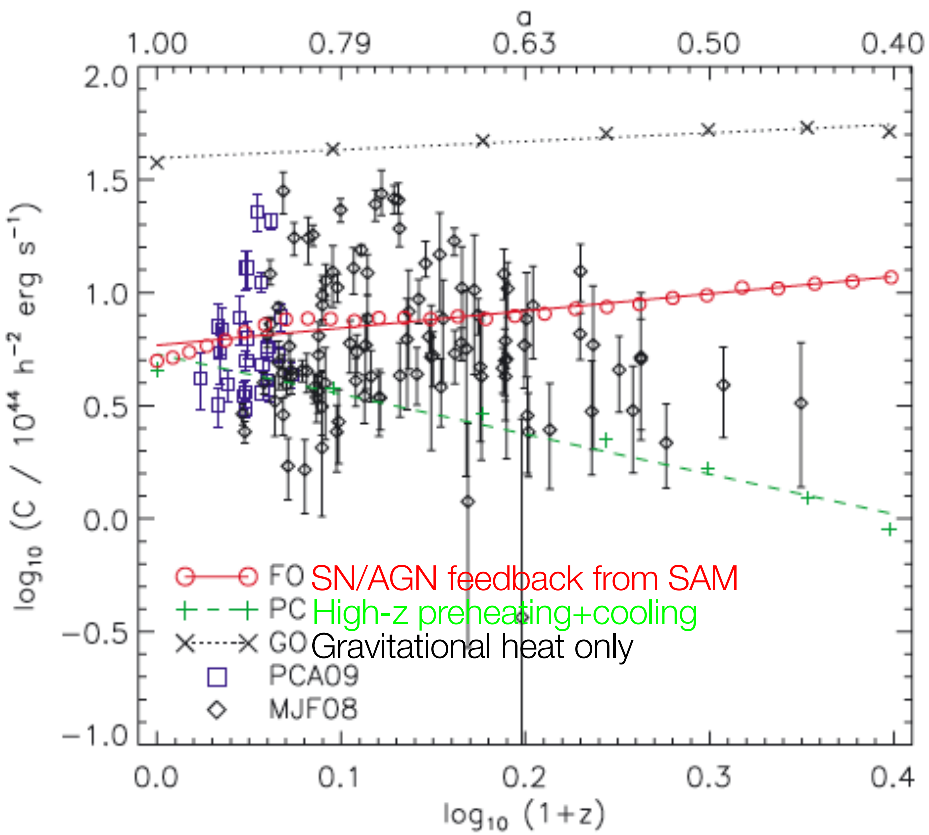

X-ray scaling laws @high-z

- **For a given mass,** scaling relations in the LCDM predict that the clusters formed at larger redshift are **hotter / denser and therefore more luminous** in X-rays than their local z~0 counterparts.

- Provided that scaling relations remain valid at larger redshifts, ***X-ray surveys will not miss massive clusters at any redshift,*** no matter how far they are.

- **New-Athena** will resolve ICM properties up to z~2, detecting the first collapsed structure at z~2.5

The Mass of Galaxy Clusters:

fundamental quantity, but systematically biased with current X-ray/SZ data

$$\boxed{\frac{G\,M_{HE}(<r)}{r^2} = -\frac{dP_g}{dr}\frac{1}{\rho_g}}$$

$$\frac{G\,M_{tot}(<r)}{r^2} = -\frac{dP_g}{dr}\frac{1}{\rho_g} - \frac{d\boldsymbol{v}}{dt}$$

$$\ldots = -\frac{d(P_g+P_{NT})}{dr}\frac{1}{\rho_g} = -\frac{dP_{tot}}{dr}\frac{1}{\rho_g}$$

$$M_{HE}\,/(1-b) = \;M_{tot} \sim T^{3/2} \sim M_{gas} \sim L^{3/4} \sim Y^{3/5}$$

Hydrostatic bias: (1-b) = M_X/M_{500}

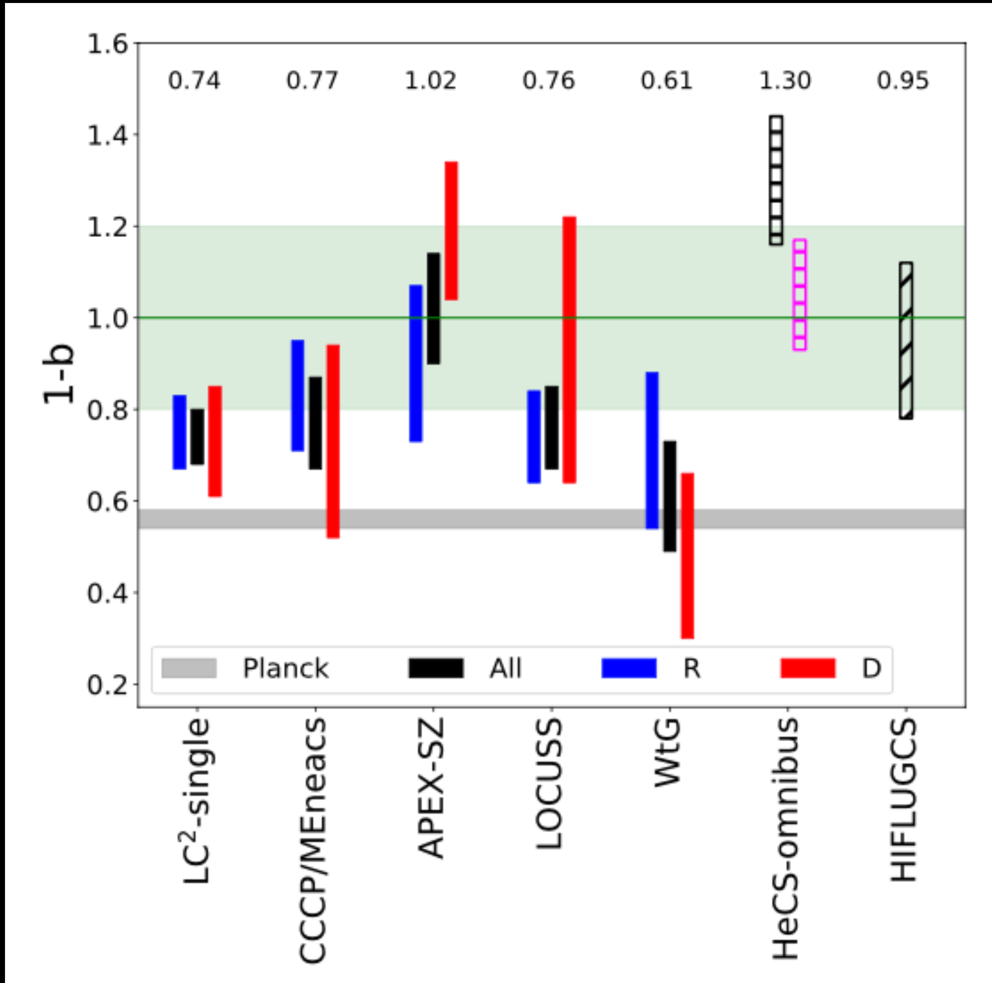

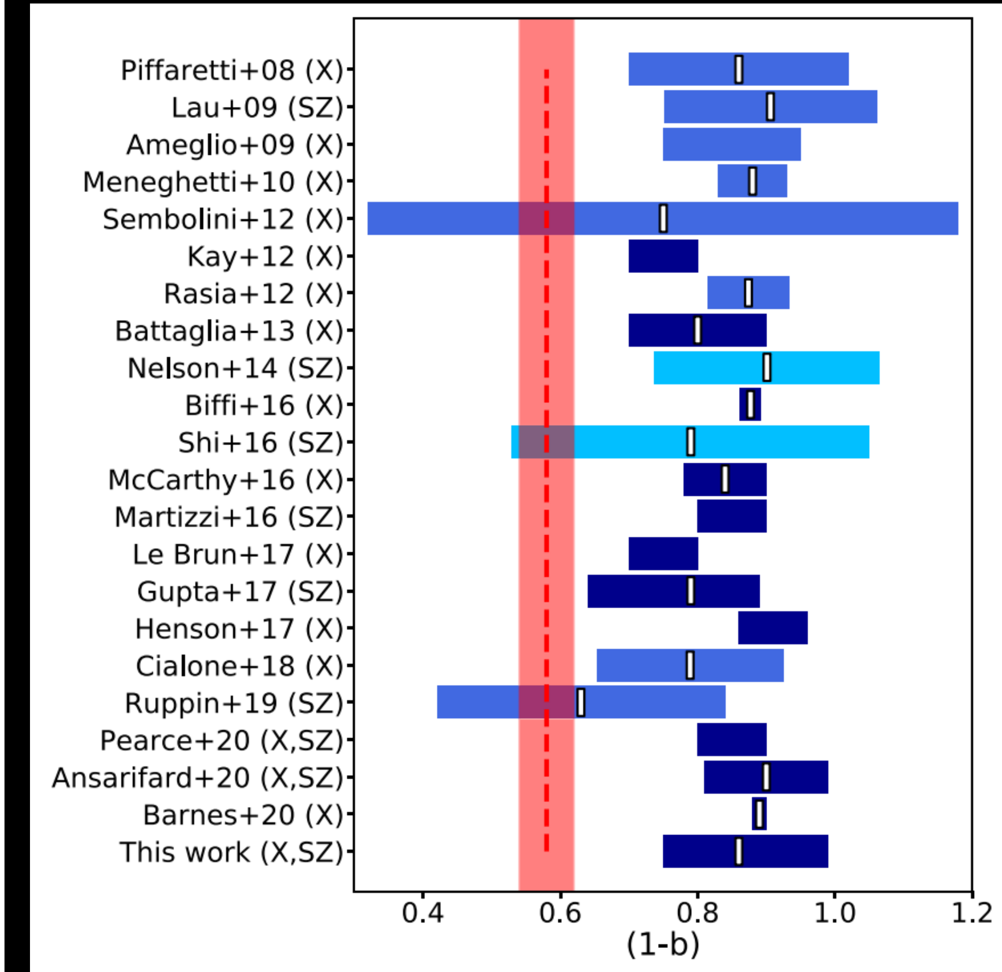

Planck ESZ sample (120 obj; ***Lovisari, Ettori+20***)

Gianfagna+21

R_{500} - limit for XMM/Chandra
R_{200} - limit for Suzaku (LEO)
$3R_{500}$ - limit for Planck SZ stack

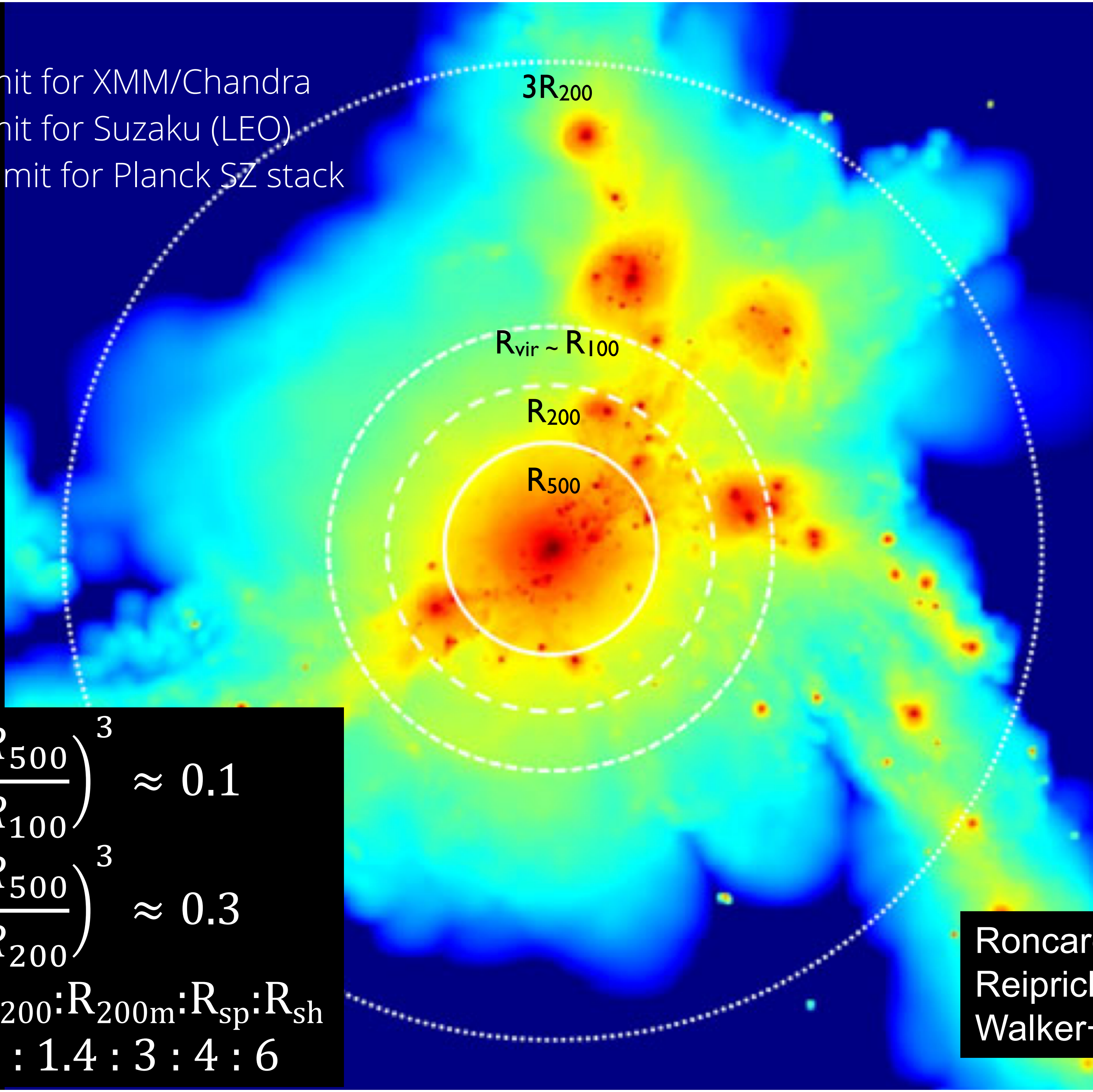

$$\left(\frac{R_{500}}{R_{100}}\right)^3 \approx 0.1$$

$$\left(\frac{R_{500}}{R_{200}}\right)^3 \approx 0.3$$

$$R_{500}:R_{200}:R_{200m}:R_{sp}:R_{sh}$$
$$= 1 : 1.4 : 3 : 4 : 6$$

Roncarelli+06
Reiprich+13
Walker+19

R500 - limit for XMM/Chandra

R200 - limit for Suzaku (

3R500 - limit for Plan

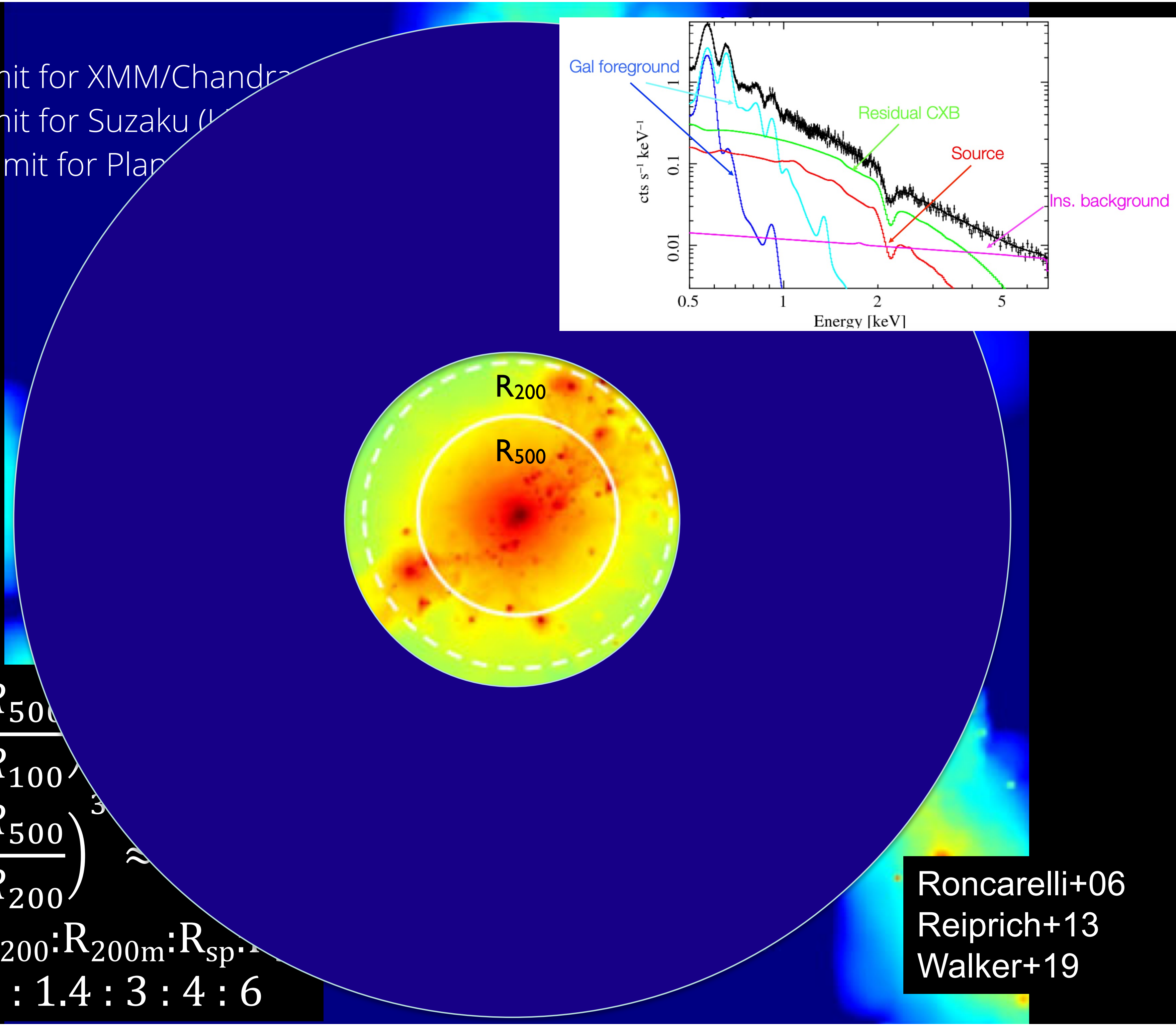

$\left(\frac{R_{500}}{R_{100}}\right)$

$\left(\frac{R_{500}}{R_{200}}\right)^{3} \approx$

$R_{500}:R_{200}:R_{200m}:R_{sp}:$

= 1 : 1.4 : 3 : 4 : 6

Roncarelli+06
Reiprich+13
Walker+19

X-COP: *XMM +Planck* (Eckert+17)

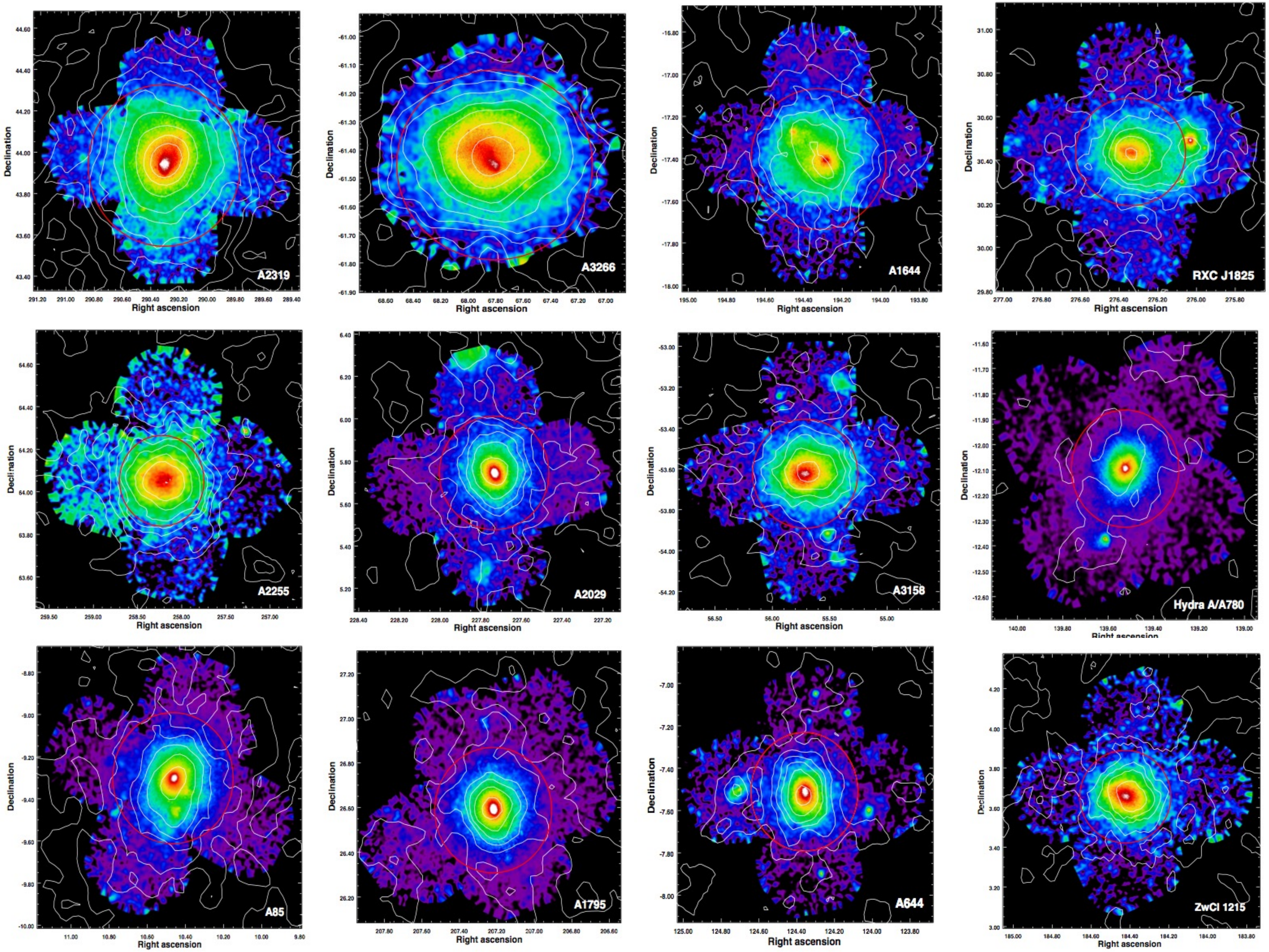

X-COP: “universal” profiles

(& scatter; Ghirardini+19)

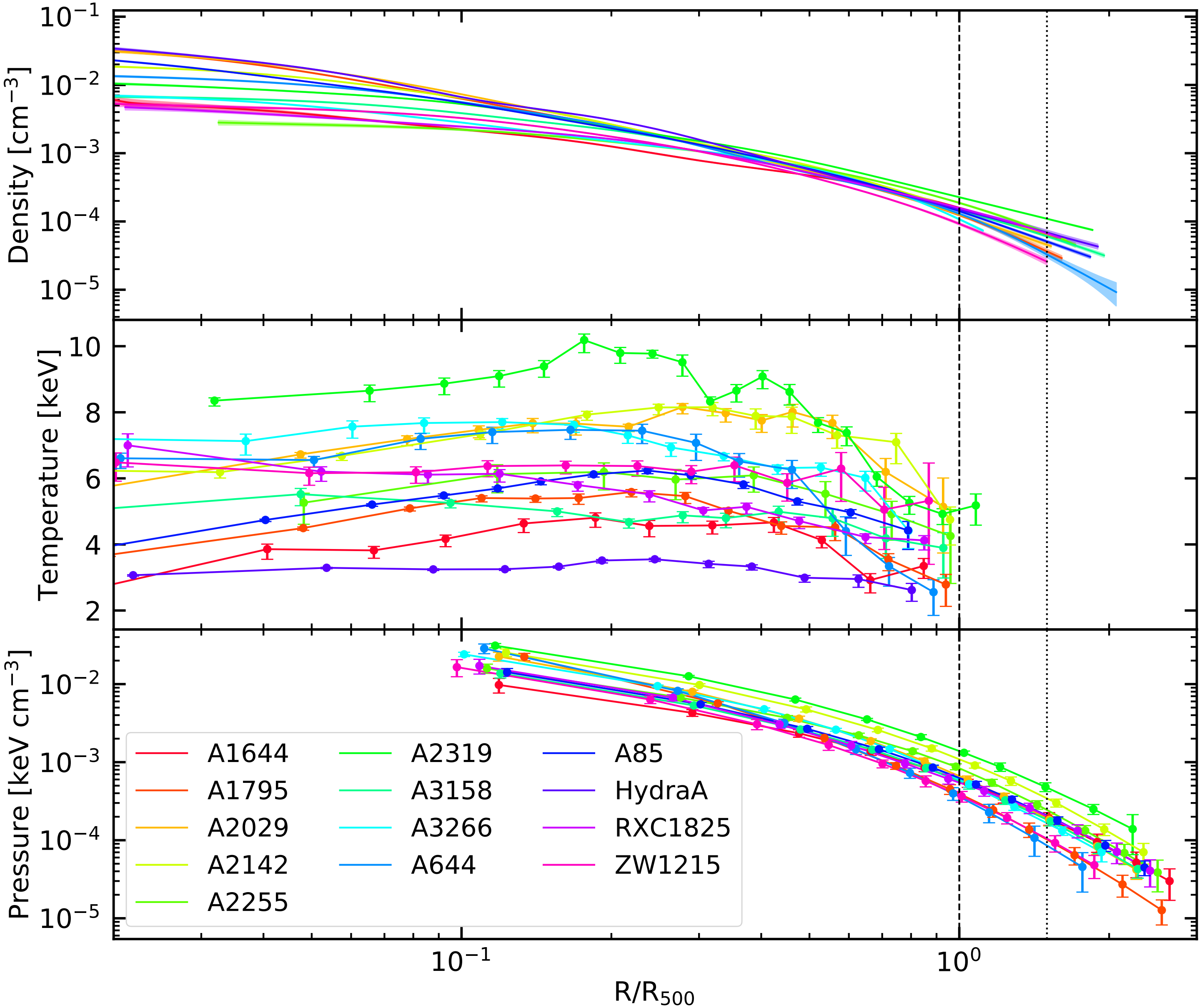

T = **P**/**n**

K = **P**/**n**$^{5/3}$

M ~ -r^2/**n** d**P**/dr

(see also Ameglio+07, 09, Shitanishi+18)

X-COP: mass profiles

(Eckert, Ettori, et al. 2022a)

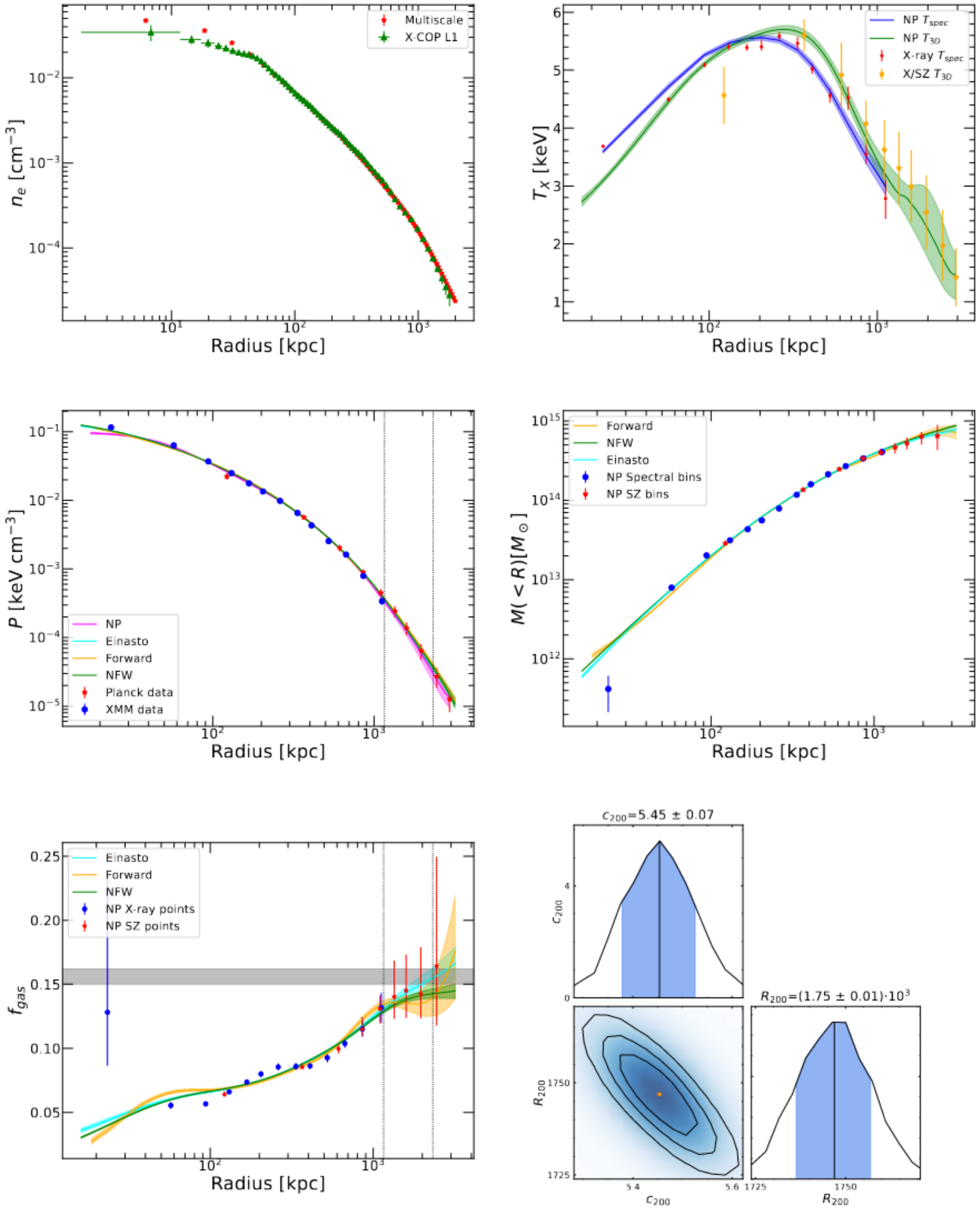

Mass reconstruction in A1795

(i) n_e profile reconstructed with the multi-scale method;

(ii) non parametric reconstruction of the 3D temperature profile compared to the spectroscopic X-ray measurements and the 3D temperature profile obtained by dividing the SZ pressure by the X-ray density (projected, spec-w, PSF convolved T)

(iii) mass profiles obtained with different reconstructions (NFW, Einasto, Forward, and NP) ➔ *https://github.com/domeckert/hydromass*

X-COP: mass profiles

(Ettori+19)

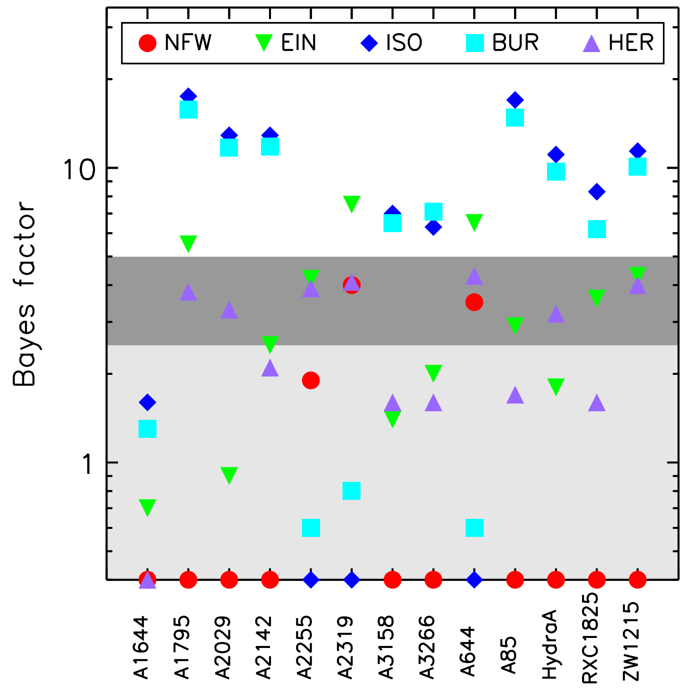

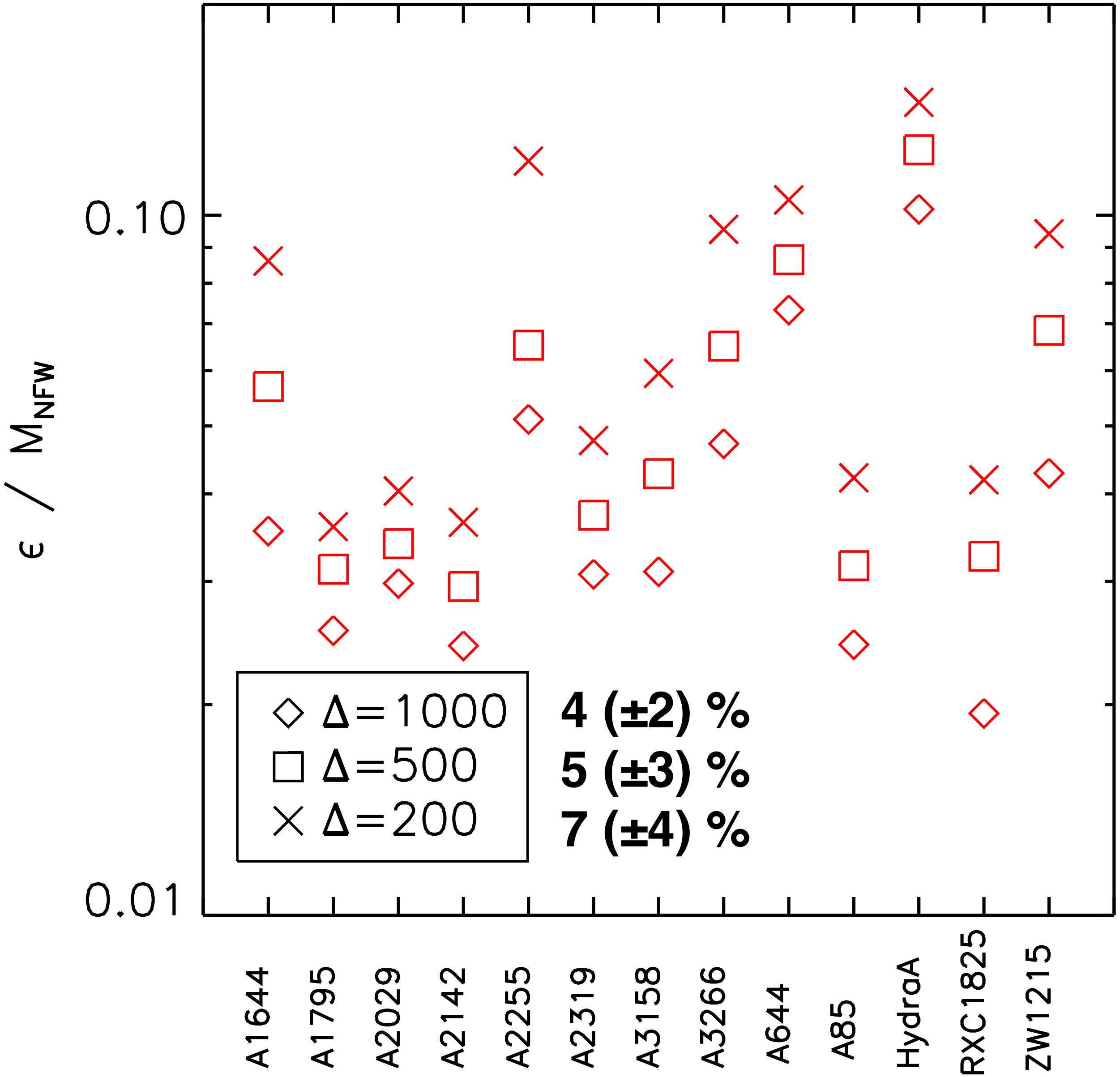

X-COP: mass profiles

(Ettori+19)

Table 2. Systematic differences between the forward method ("Forw") and the other mass models described in Sect. 3.1 with respect to the model of reference defined as backward NFW.

M_i	B (inter-quartile range) %				
	0.5 Mpc	1 Mpc	1.5 Mpc	R_{500}	R_{200}
Forw	+0.6 (−1.1/+3.3)	−2.0 (−5.9/+1.4)	−4.6 (−7.9/+1.3)	−4.7 (−10.9/−0.5)	+1.2 (−5.4/+8.1)
Forw (no SZ)	−1.5 (−3.4/+4.1)	−1.9 (−8.0/+0.6)	−1.3 (−5.4/+4.5)	−4.2 (−9.0/+1.8)	+1.3 (−11.9/+8.0)
EIN	−0.3 (−1.7/+1.3)	−1.7 (−6.5/−0.2)	−1.0 (−9.7/+1.5)	−0.8 (−7.6/+1.0)	−0.8 (−10.3/+4.3)
ISO	+14.1 (+11.8/+21.0)	−3.0 (−3.5/+5.4)	−13.3 (−19.0/−9.7)	−8.2 (−13.0/−5.3)	−23.5 (−28.7/−16.5)
BUR	+11.4 (+10.4/+15.1)	−3.1 (−5.8/+4.0)	−13.7 (−19.2/−8.3)	−8.3 (−12.9/−5.2)	−20.8 (−24.2/−17.9)
HER	+1.6 (+0.9/+2.1)	−0.7 (−5.6/+0.2)	−5.5 (−11.4/−2.4)	−3.7 (−5.3/−1.9)	−9.3 (−13.5/−6.8)

Notes. These differences are quoted as the median (1st-3rd quartiles, in brackets) of the quantity $B = (M_i/\mathrm{NFW} - 1) \times 100\%$, where M_i is listed in the first column.

X-ray mass: final considerations

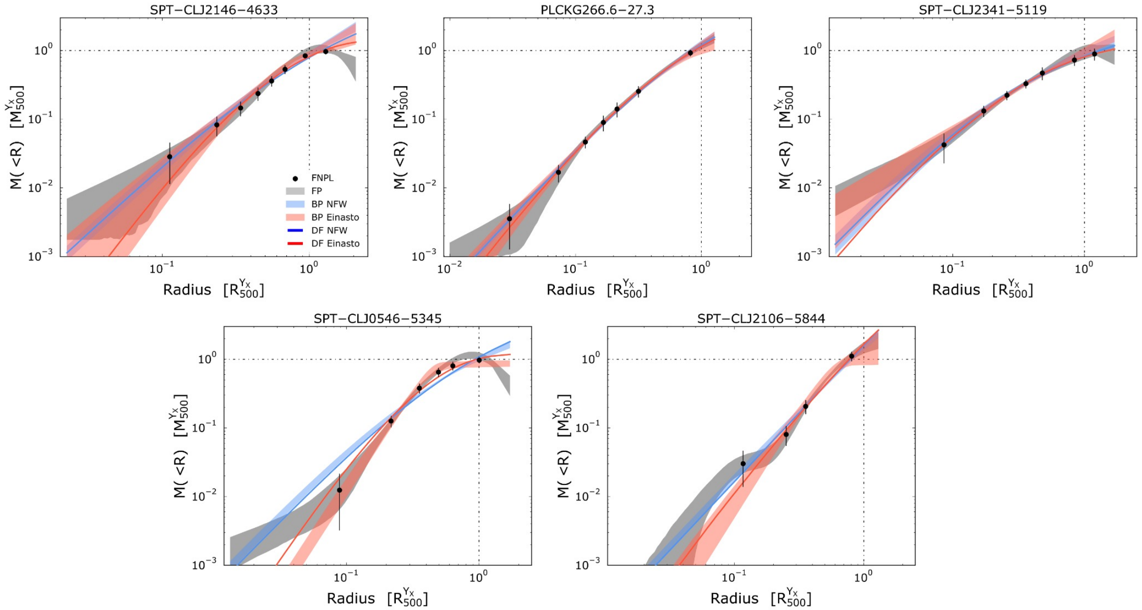

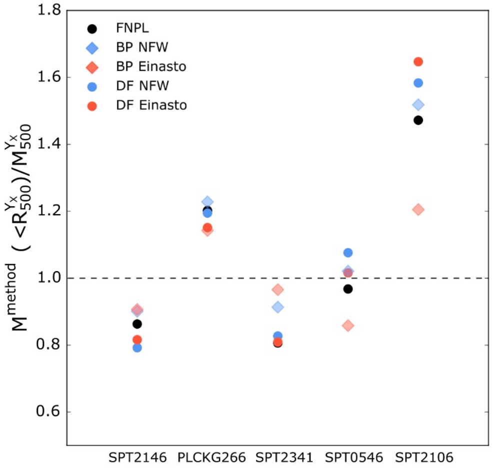

Fig. 3: Comparison of the hydrostatic mass computed at fixed radius, $R_{500}^{Y_X}$, using the different methods, in units of $M_{500}^{Y_X}$. There is excellent agreement, with differences of less than 10%, when the radius is enclosed in the radial range covered by the spectroscopic data.

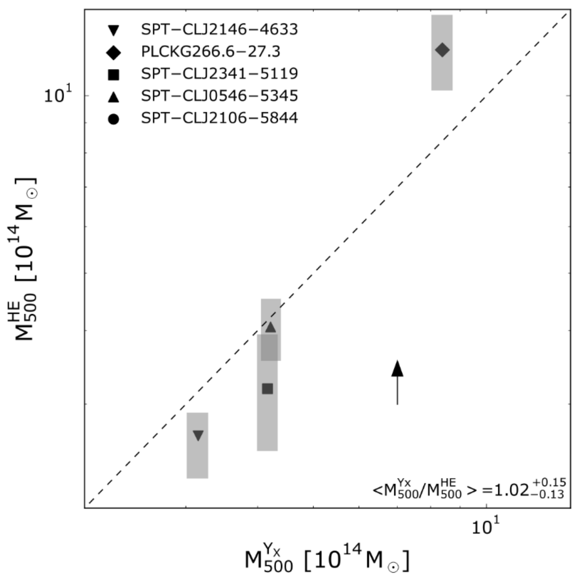

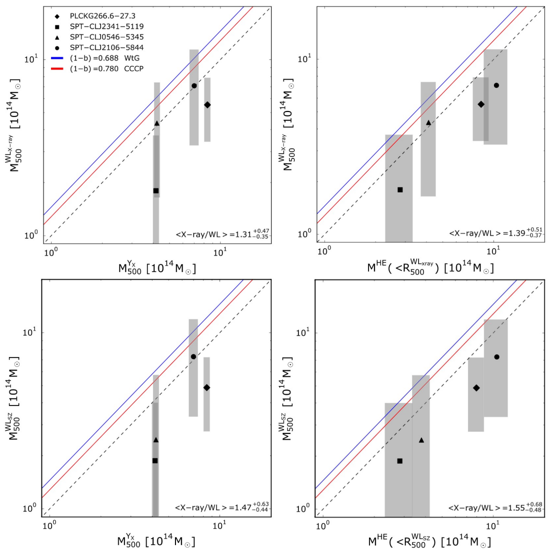

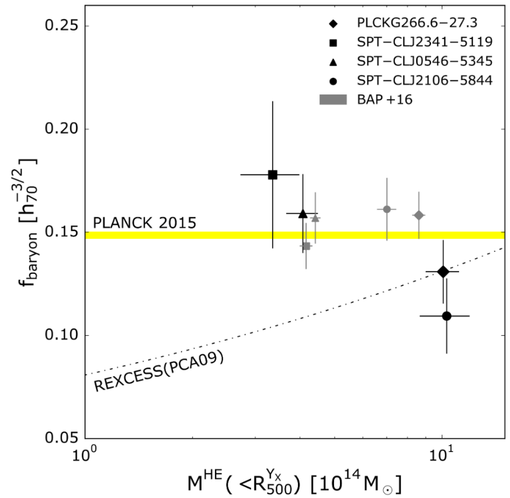

M_{HE} @z~1; Bartalucci+18

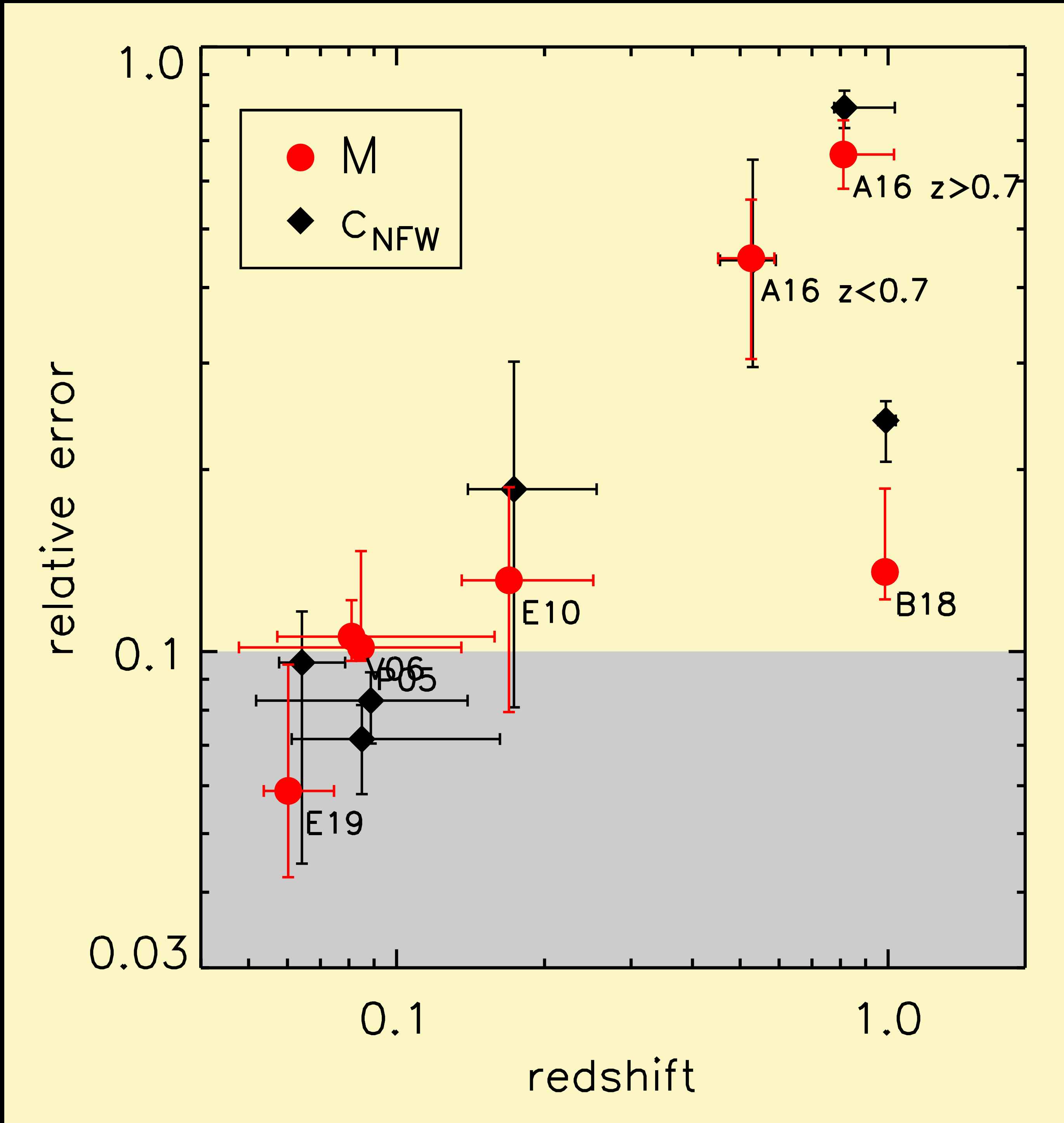

Amodeo+16
Bartalucci+18
Ettori+10, 19
Pointecouteau+05
Vikhlinin+06

X-ray mass: vs Lensing, Caustic

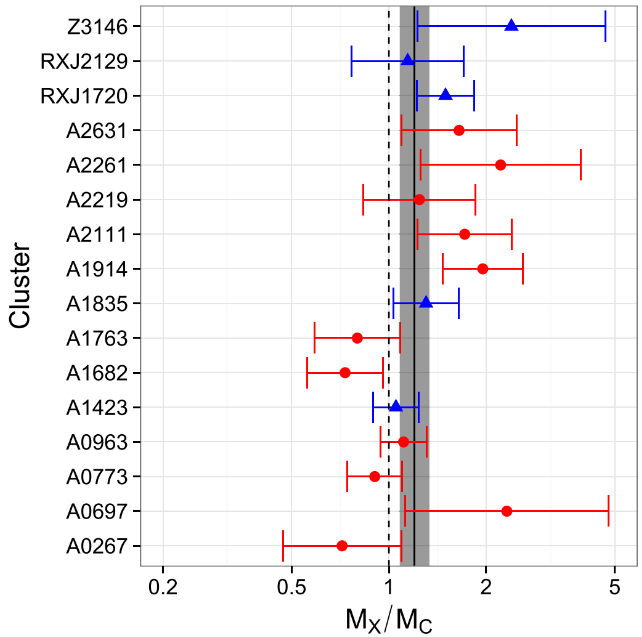

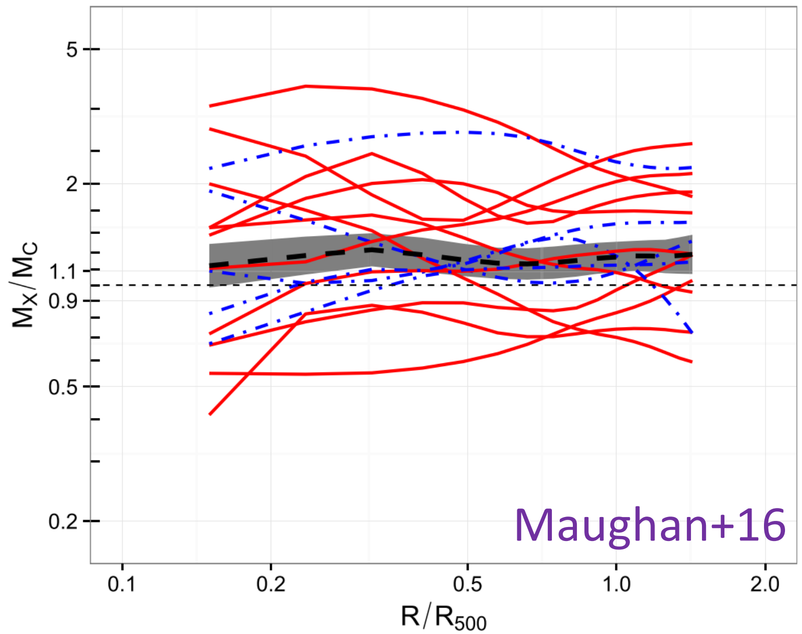

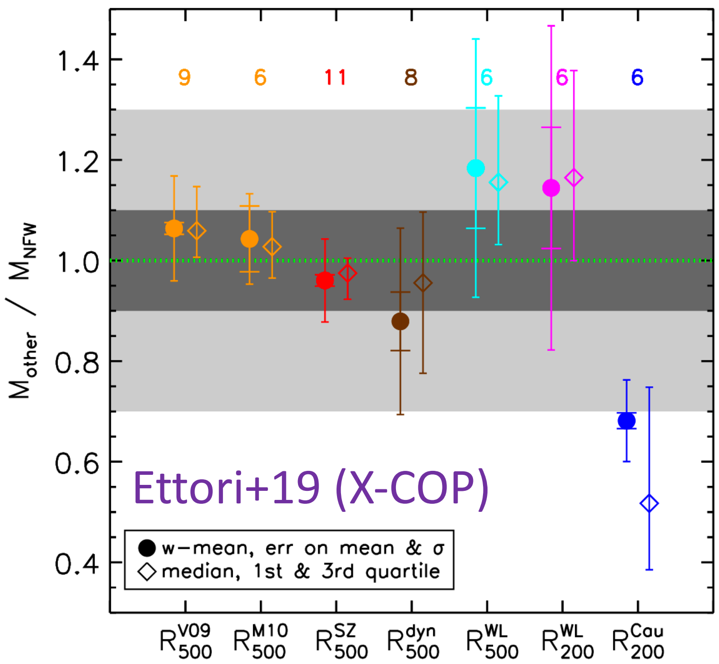

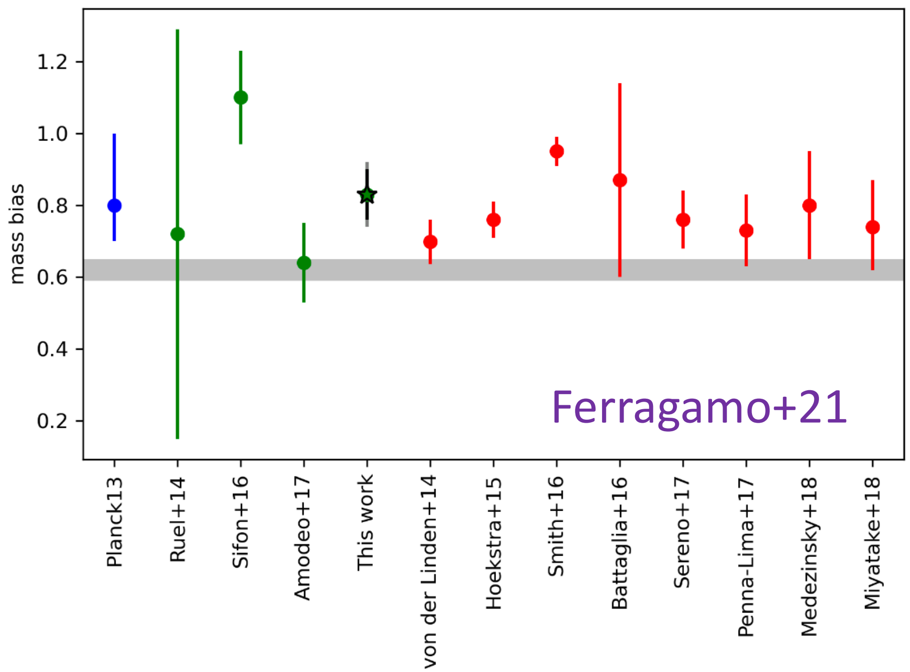

X-ray mass: final considerations

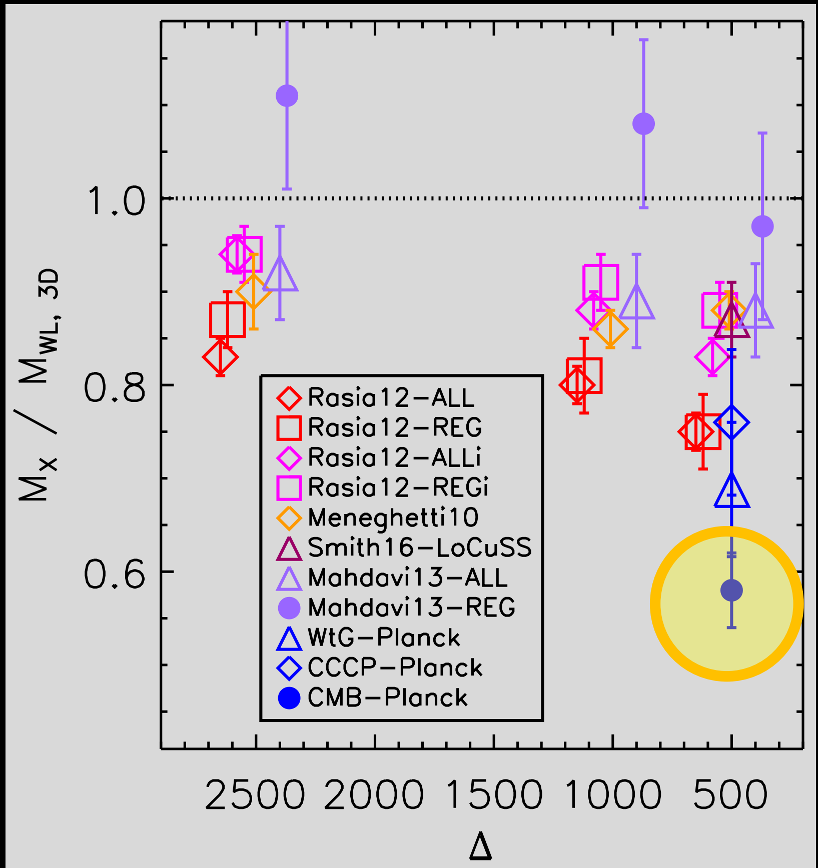

- hydrostatic mass estimates may have systematic biases (Rasia+06, Nagai+07) and is function of R, M, dynamical state (M_{hyd} ~ M_{tot} in CC)
- Done a lot of work on systematics related to the methods (Ettori+10, Bartalucci+18)
- **HE holds locally**: we need objective methods to characterize the dynamical state & localize disturbed regions
- **f_{bar} ~ Ω_b/Ω_m** once some depletion is accounted for (if M_{hyd} is underestimated, "missing baryons" problem appears –see Ettori 2003)

– assumption of spherical symmetry	few %
– hydrostatic mass bias	< 10–30%
– gas temperature inhomogeneities	few–10–15%
– gas clumping	few %
– absolute X-ray temperature calibration	15–20%

Pratt+19

T_{spec} x-calibration

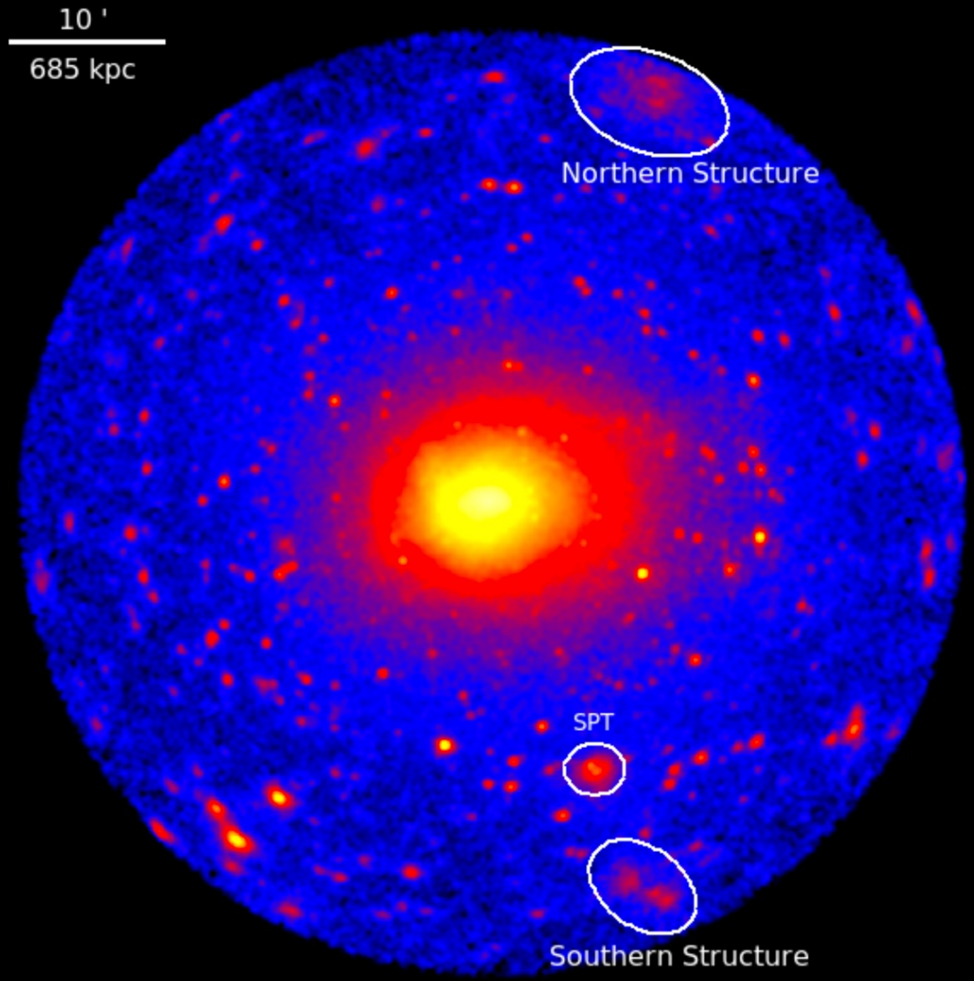

A3158 (Whelan+22)

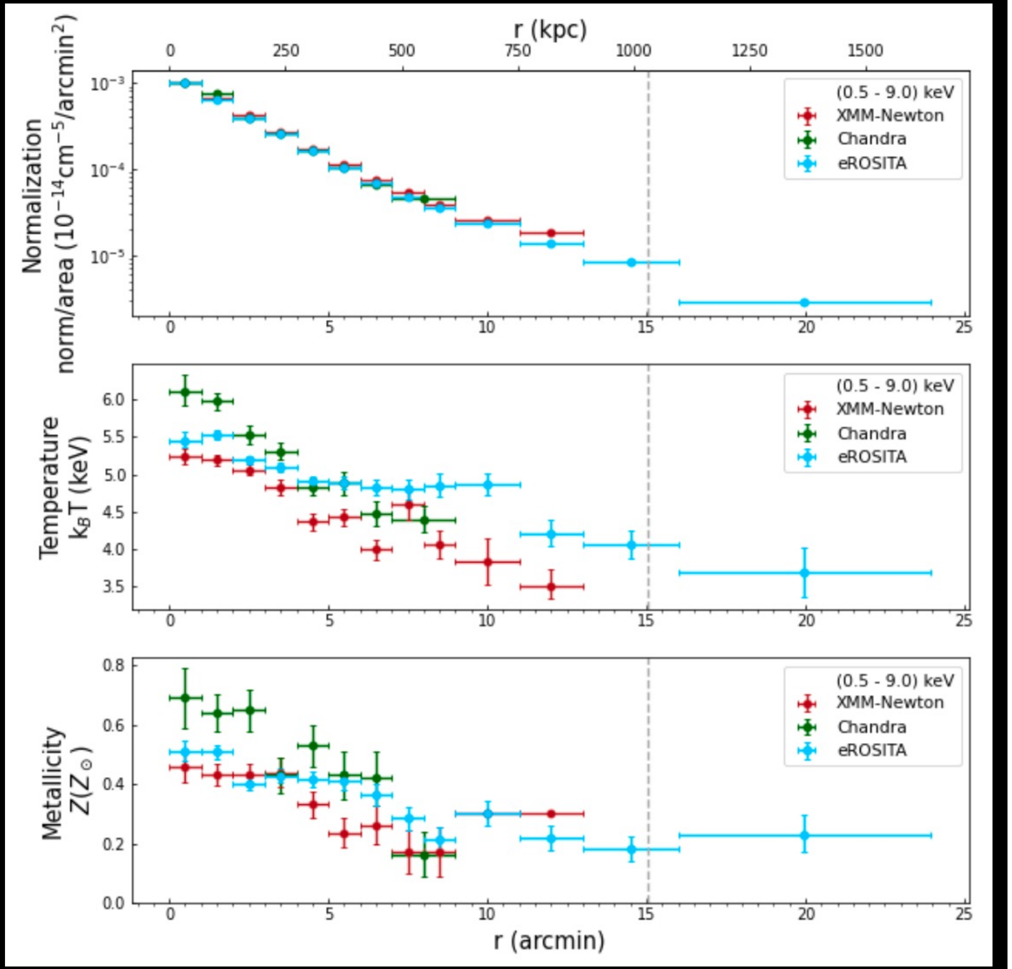

T_{spec} x-calibration

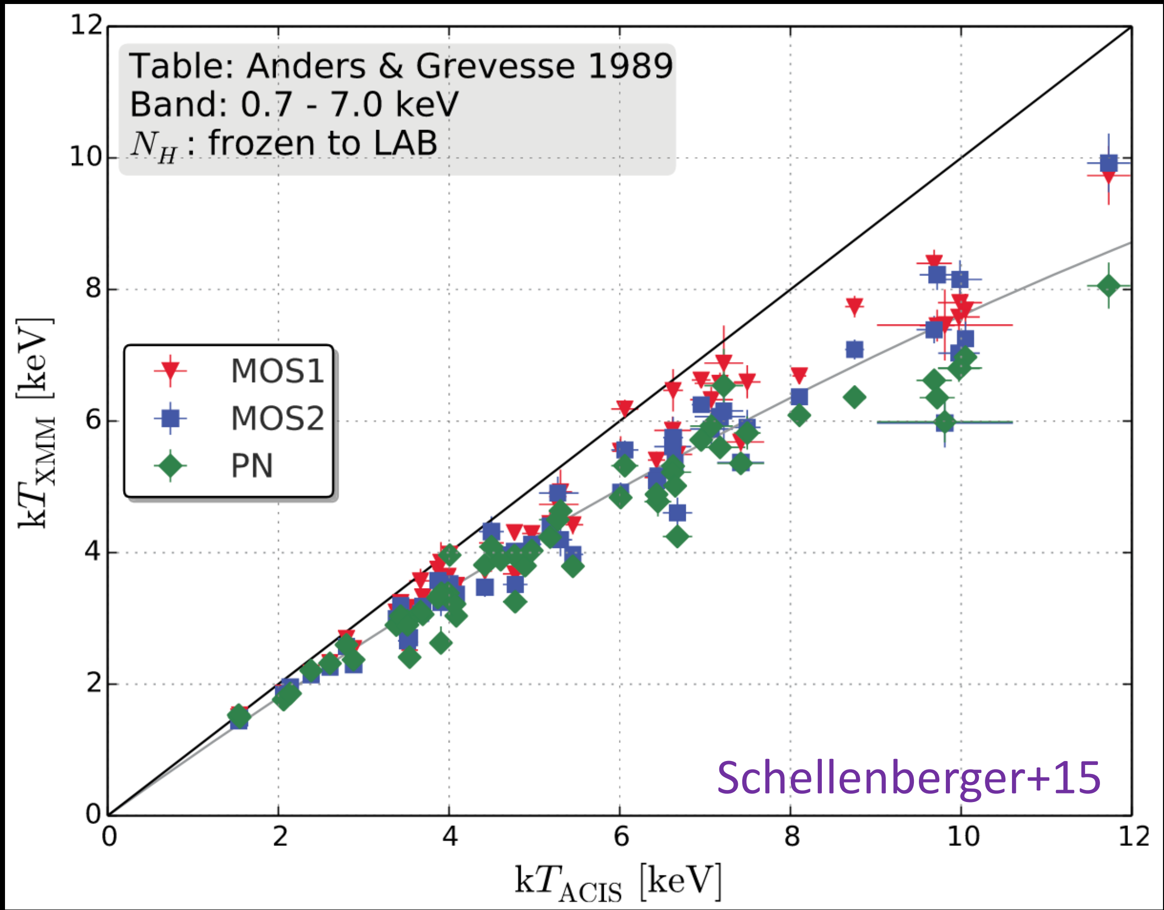

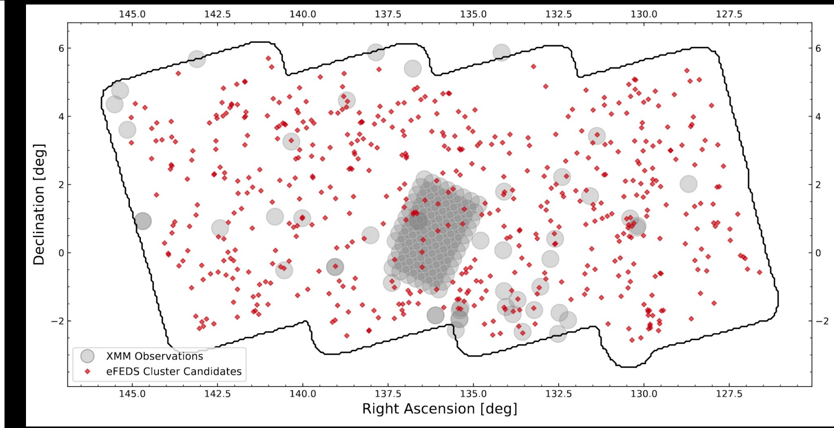

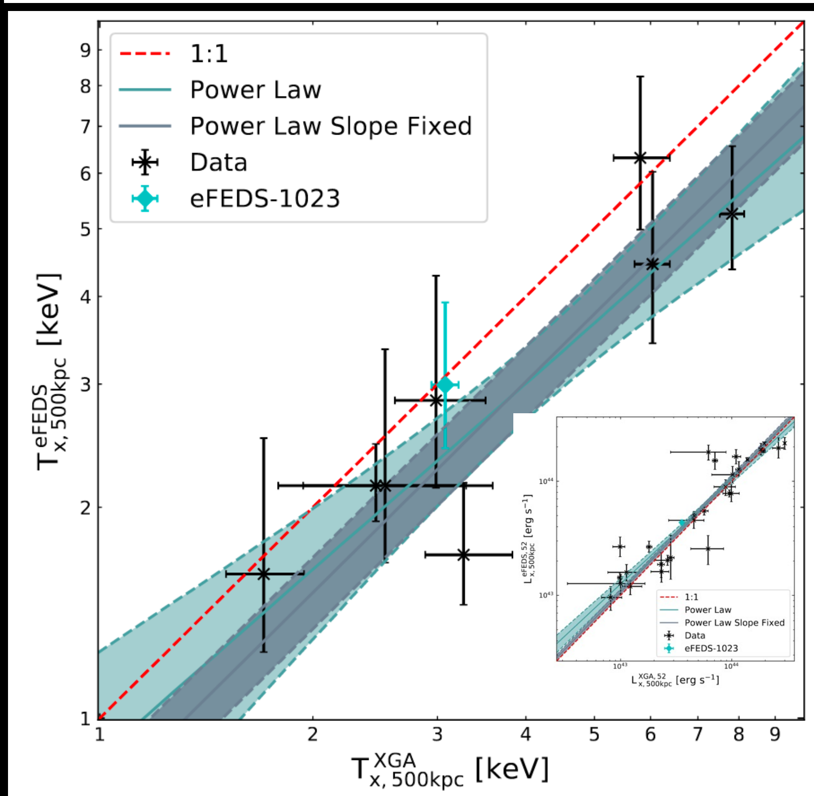

(Turner+21) 8 obj in common;
T_{XMM} 25% higher than T_{eFEDS}
L in agreement
➔ dedicated XMM GO with Lovisari:
~20 obj, stay tuned ;-)

T_{spec} x-calibration

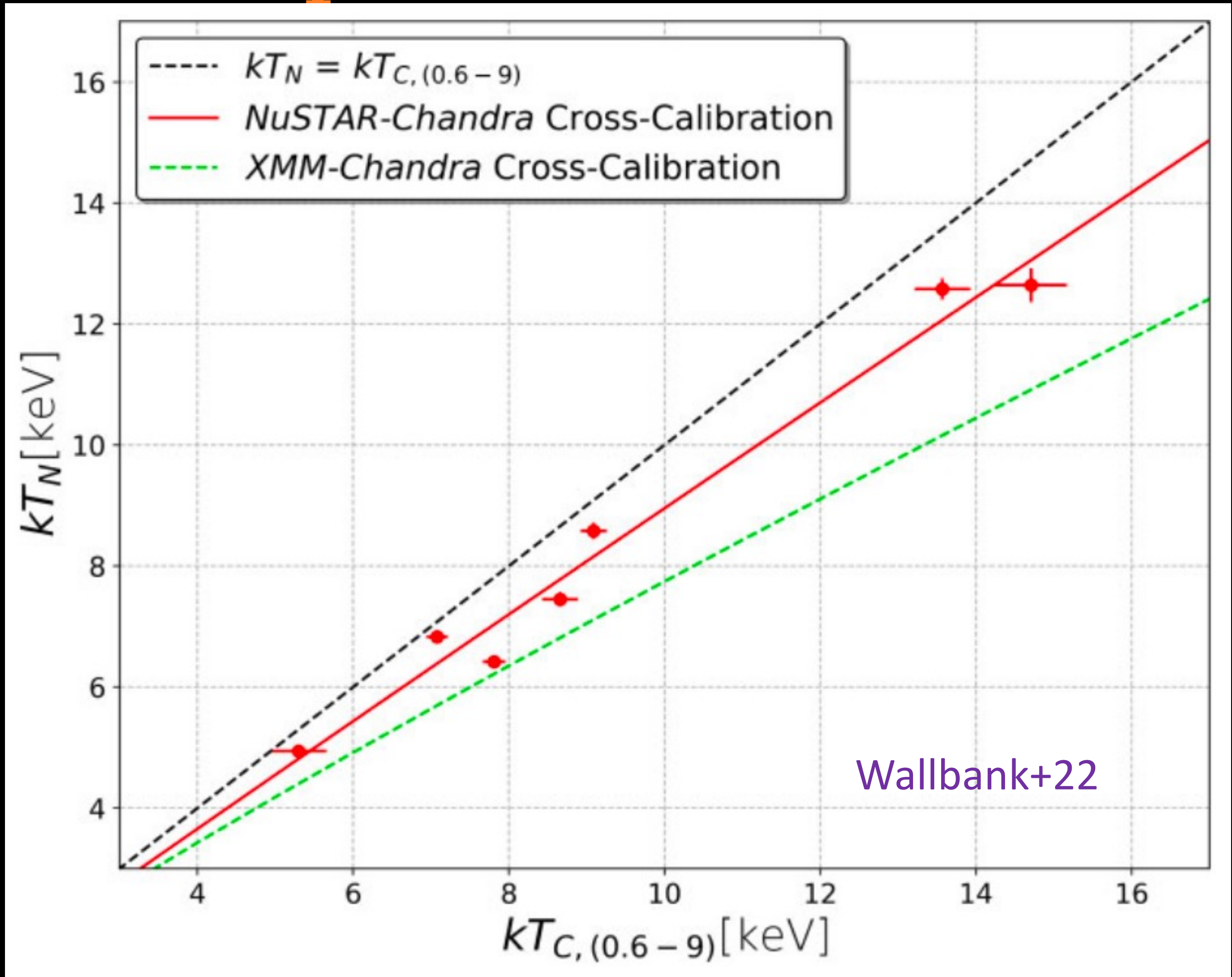

At a Chandra temperature of 10 keV, the average NuSTAR (3-10 keV) T_{spec} was (10.5 ± 3.7) and (15.7 ± 4.6) % lower than Chandra for the broad- and hard-band fits, respectively

T_{spec} x-calibration

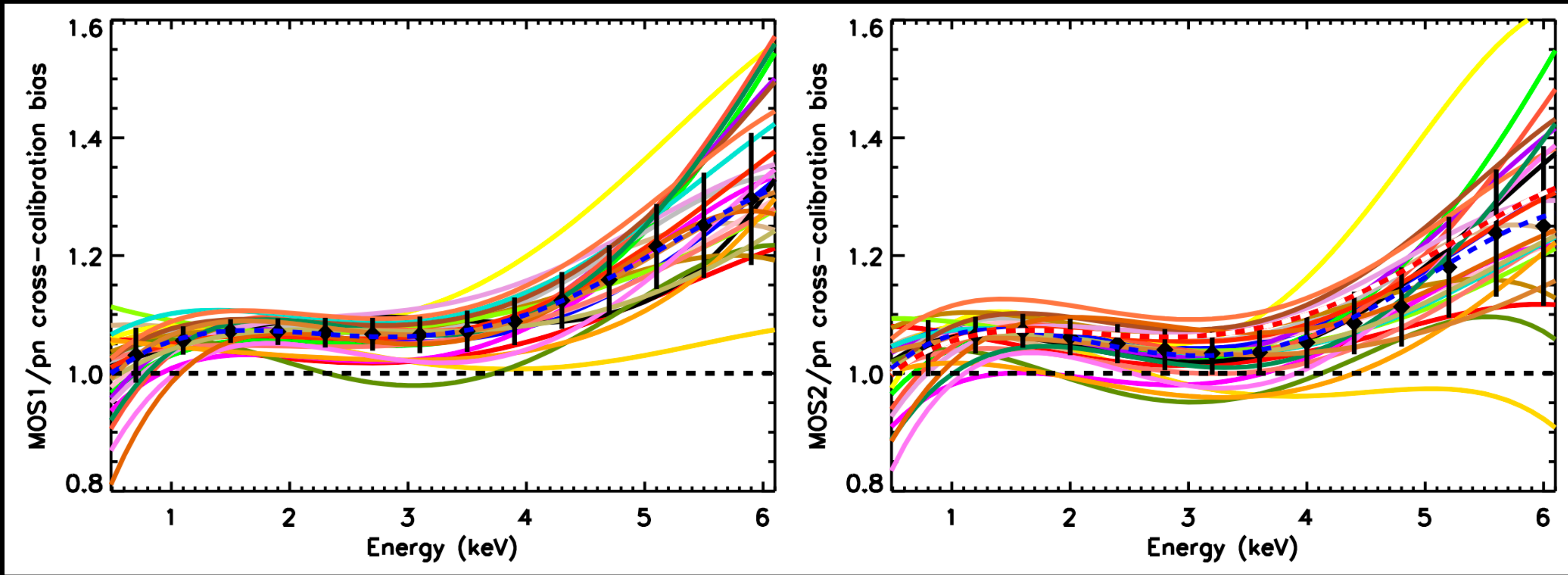

(Nevalainen & Molendi 23) The MOS/pn bias is systematic suggesting that MOS (pn) effective area may be calibrated too low (high), by ~3-27% on average depending on the instrument and energy band. The excellent agreement of the energy dependencies (i.e. shapes) of the effective area of MOS2 and pn suggest that they are correctly calibrated within ~1% in the 0.5-4.5 keV band.

Comparison with an independent data set of point sources (3XMM) confirms this. The cluster sample indicates that the MOS1/pn effective area shape cross-calibration has an approximately linear bias amounting to ~10% in maximum in the 0.5-4.5 keV band

T_{spec} x-calibration: *vs SZ*

$T_{mod\text{-}spec} = \eta_T P_{SZ} / n_e$
Bourdin+17

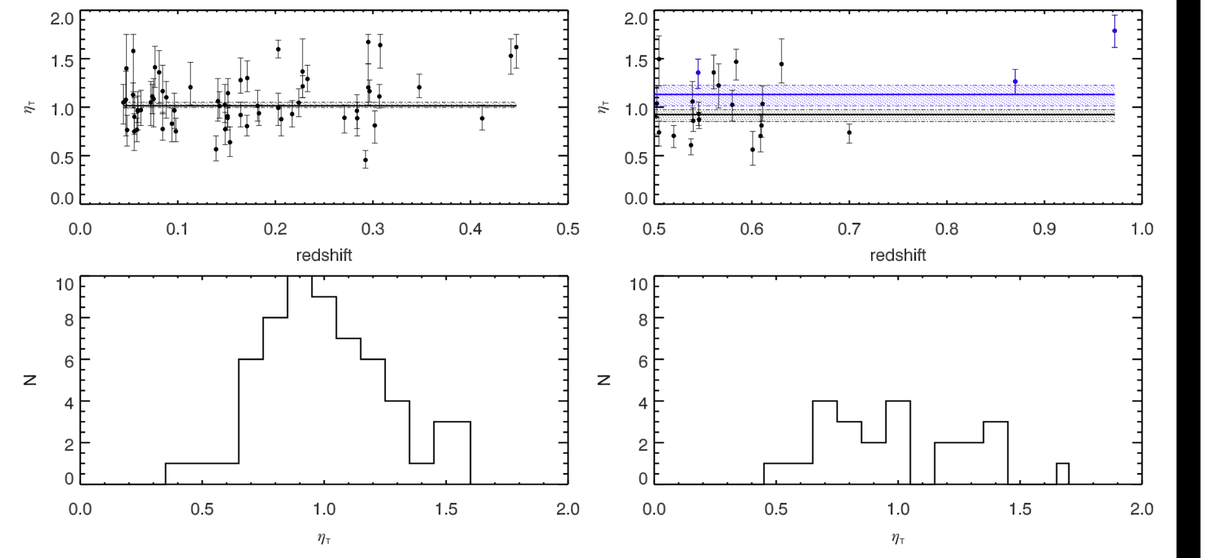

Figure 6. Normalization of the spectroscopic temperatures measured in the nearby (left) and distant (right) cluster samples. *Top:* Normalization values. Black and blue points correspond to *XMM-Newton* and *Chandra* measurements, respectively. Horizontal lines depict temperature normalizations of the average profiles in each sample. *Bottom:* Histogram of the normalization values.

$\eta = P_{SZ} / P_X$
Ettori+20

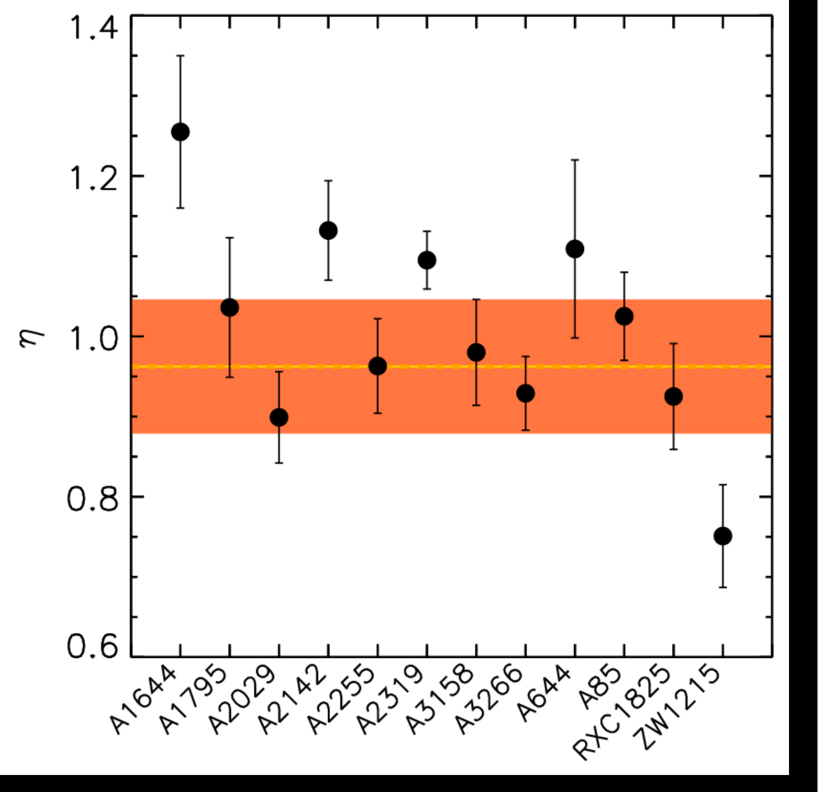

Cosmology from the **internal structures** of Galaxy Clusters

- **Mass distribution ➔** *(SI)DM / MOND* (Ettori+19; Eckert+22)
- **Concentration/sparsity ➔** $\{\Omega_m; \sigma_8\}$ (Corasaniti+21, 22)
- **Triaxial shape ➔** consistency with ΛCDM (Sereno+18)
- **X/SZ pressure profiles ➔** H_0 (*Kozmanyan+19;* Ettori+20)
- **Gas mass fraction ➔** $\{\Omega_m; \Lambda, w\}$ (Ettori+10; *Mantz+21*)

➔ Reliable & robust reconstruction of the (total & baryonic) **mass distribution**

Total mass from SZ/X-rays

Total mass is the fundamental tool to use Galaxy clusters as cosmological probes

- *low counts statistic*: **scaling relations**

(for galaxy clusters mass function: M_{tot} vs $L/T/M_{gas}/Y_X$ *or* ***a combination of these***…)
Ettori et al. 2012; Ettori 2013 & 2015

$$M_{tot} \propto L^{\alpha} M_g^{\beta} T^{\gamma}; \quad 4\alpha + 3\beta + 2\gamma = 3$$

$M_{tot} \sim L^{\alpha} \ T^{-2\alpha+1.5}$

$\alpha = 0$ … $M_{tot} \sim T^{1.5}$
$\alpha = 3/4$ … $M_{tot} \sim L^{3/4}$
$\alpha = 1/2$ … $M_{tot} \sim (LT)^{1/2}$

$M_{tot} \sim M_{gas}^{\alpha} \ T^{-1.5\alpha+1.5}$

$\alpha = 0$ … $M_{tot} \sim T^{1.5}$
$\alpha = 1$ … $M_{tot} \sim M_{gas}$
$\alpha = 3/5$ … $M_{tot} \sim (M_{gas} T)^{3/5} \sim Y^{3/5}$

The generalized scaling relations:

$$M_{tot} = K\, A^{a}\, B^{b}$$

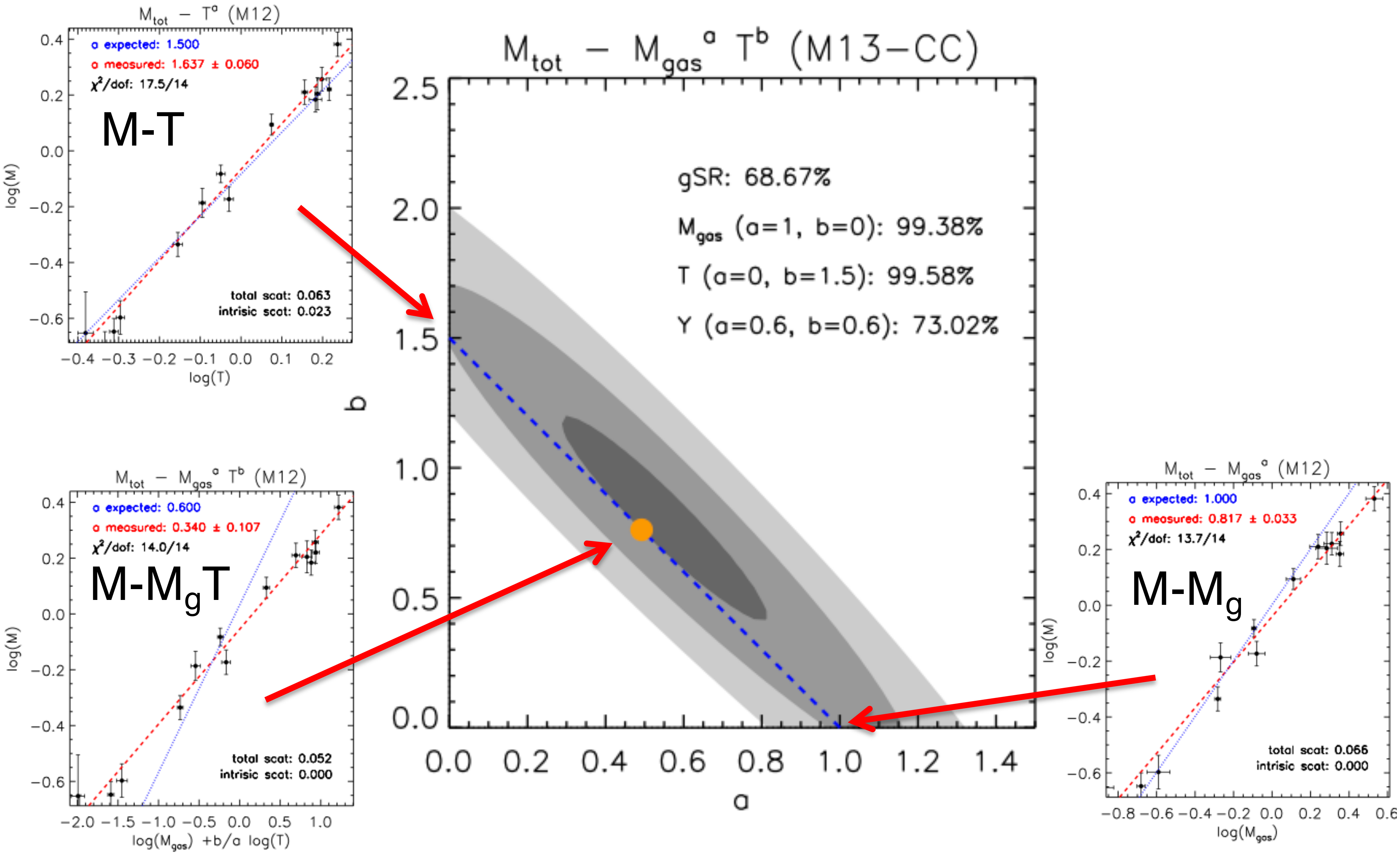

X-ray/SZ scaling relations:

Self-similar +$\{f_g, C, \beta\}$

In galaxy clusters,
the relations between M_{tot} & X-ray/SZ observables have a power-law behaviour with **normalization**, **slope** and **z-evolution** that are simple to estimate in a self- similar scenario

The ***self-similar*** prediction on **normalization & slope** can fully explain the ***observed X-SZ SL*** once **$\{f_g(M), \beta_P(M), C\}$** are considered

X-ray/SZ scaling relations:

Self-similar +{f_g, C, β}

$$F_z M \sim \beta_{\mathrm{P}}^{\theta} f_{\mathrm{g}}^{-\phi} \, (F_z^{-1} L)^{\alpha} (F_z M_{\mathrm{g}})^{\beta} T^{\gamma}$$

$$4\alpha + 3\beta + 2\gamma = 3$$

$$\theta = \alpha/2 + \gamma$$

$$\phi = 2\alpha + \beta$$

(Ettori 2015)

The coming era of multiple observable signals from combined surveys in optical, submillimeter and X-ray wavebands invites a more holistic approach to modeling multiwavelength signatures of clusters. The combination of observable cluster signals reflects the astrophysical evolution of the coupled baryonic and dark matter components in massive halos: **it improves mass selection & estimates**

(e.g. Cunha09; Okabe+10; Stanek+10; Ettori+12-14; Evrard+14; Maughan 14; Rozo+14)

- ICM can be described by "***universal***" profiles (ie *thermodynamic radial profiles that should be equal -within the intrinsic scatter- once rescaled by halo **mass** and **redshift***)

- ***But, it is still missing*** a consistent picture that links these **universal radial profiles** and the **integrated values** of the ICM thermodynamical quantities, also quantifying the deviations from the *standard self-similar gravity-driven scenario*

i(cm)z

a semi-analytic model of the ICM matching *observed* both spatially-resolved & integrated quantities

(Ettori, Lovisari, Eckert 2023; arxiv:2211.03082)

i(cm)z

or a recipe to prepare an ICM that matches ***observed*** spatially-resolved & integrated quantities

- an "universal" $P = P_{500}\, P_0 /(c_{500}\, x)^c / [1 + (c_{500}\, x)^a]^{(b-c)/a}$
- a (c-M-z) relation, $c_{200} = A\, M_{200}^B\, (1+z)^C$
- stir them together in hydrostatic equilibrium
- then add a bit of 3 further ingredients:

(i) $f_T = T(R_{500})/T$, (ii) $f_g = C^{0.5}\, f_{gas}$, (iii) hydrostatic bias b_{HE}

$$\begin{cases} f_{T,\mathrm{ESZ}} = 0.697(\pm 0.103) \times (T/5\,\mathrm{keV})^{0.15(\pm 0.06)} \\ f_{g,\mathrm{ESZ}} = 0.121(\pm 0.045) \times (T/5\,\mathrm{keV})^{0.45(\pm 0.09)} \\ C_{\mathrm{ESZ}} = (<1.4) \times (T/5\,\mathrm{keV})^{1.0(\pm 0.5)} \end{cases}$$

& constraints on b_{HE}

→ ***Ettori, Lovisari, Sereno*** (2020 A&A 644 111)

i(cm)z

or a recipe to prepare an ICM that matches ***observed*** spatially-resolved & integrated quantities

- an "universal" $P = P_{500}\, P_0 / (c_{500}\, x)^c / [1 + (c_{500}\, x)^a]^{(b-c)/a}$
- a (c-M-z) relation, $c_{200} = A\, M_{200}^B\, (1+z)^C$
- stir them together in hydrostatic equilibrium
- then add a bit of 3 further ingredients:

(i) $f_T = T(R_{500})/T$, (ii) $f_g = C^{0.5} f_{gas}$, (iii) hydrostatic bias b_{HE}

- adding the redshift evolution
- new calibrations in (M, z) based on >2020 scaling laws & recent thermodynamic profiles
- new constraints on b_{HE} *(e.g. X-COP)*

→ ***Ettori, Lovisari, Eckert*** (2023; arXiv:2211.03082)

Universal P profile (Nagai+07, Ghirardini+19)

$$P_g = P_{500}\, P_0 / (c_{500}\, x)^c / [1 + (c_{500}\, x)^a]^{(b-c)/a}$$

+ cMz relation (Bhattacharya+13, Dutton+14)

$$c_{200} = A\, M_{200}{}^B\, (1+z)^C$$

& HEE

$$\frac{G\, M_{tot}(< r)}{r^2} = -\frac{dP_g}{dr}\frac{1}{\rho_g}$$

$$M_{tot} \sim R\, T \sim \Delta\, R^3 \sim T^{3/2} \sim M_{gas} \sim L^{3/4} \sim Y^{3/5}$$

Universal P profile
+ cMz relation
& HEE

$$\begin{cases} Q_M(r) \\ \widehat{Q_M} \end{cases} \xrightarrow{f_T \; f_g \; h} \begin{cases} Q_O(r) \\ \widehat{Q_O} \end{cases}$$

$\mathbf{f_T} = T(R_{500}) \,/\, T = t_0 \, T^{\,t1}$

$\mathbf{f_g} = \mathbf{C^{0.5}} \, M_g \,/\, M_{tot} = f_0 \, T^{\,f1}$

$\mathbf{h} = (1\text{-}b) \;\; = h_0$

As proposed in *Ettori 2015* to accommodate for **deviations** from **self-similar relations**

i(cm)z

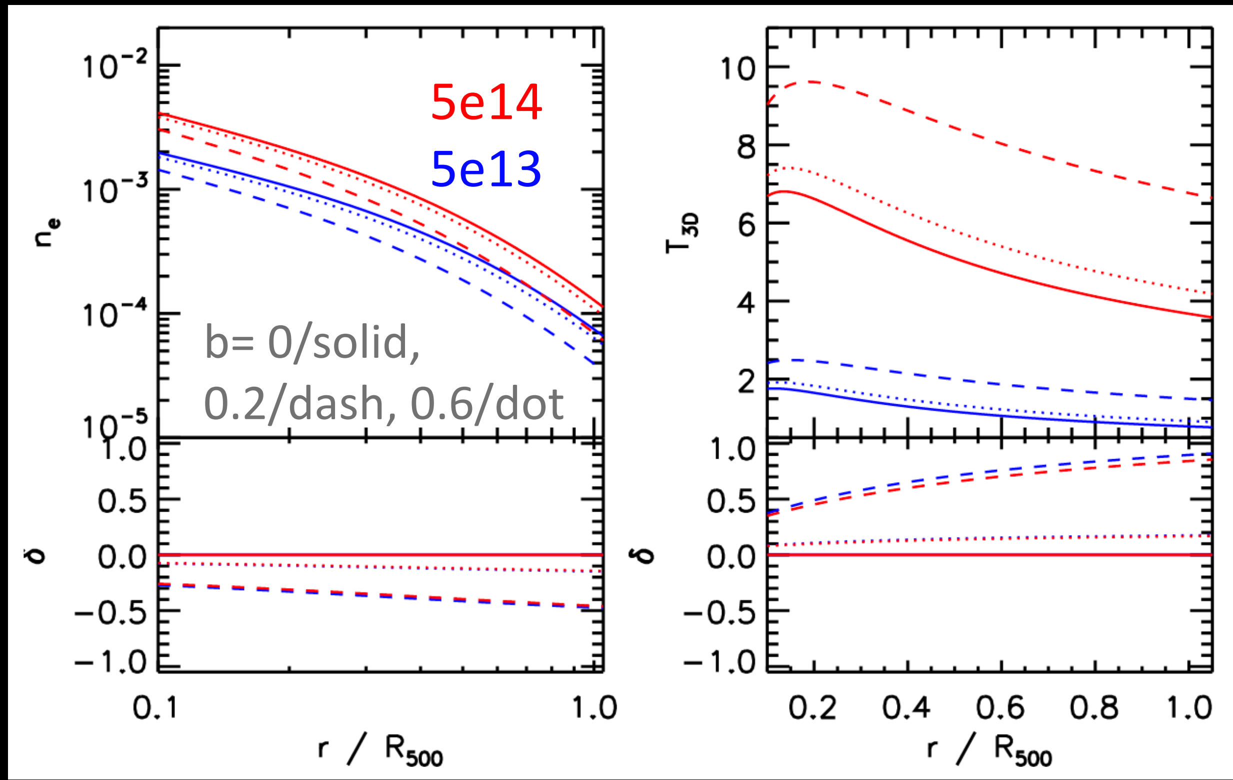

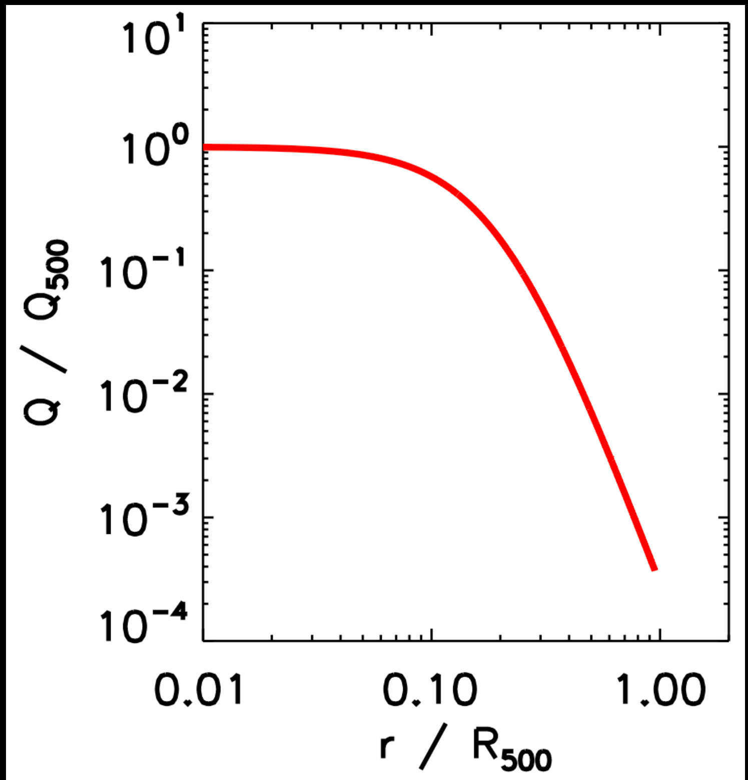

$$M_{HE} = (1 - b)\, M_{tot}$$

$$R_{500} \sim M_{tot}^{1/3}$$

$$Q_{500} = f(\,M_{tot})$$

Universal profiles

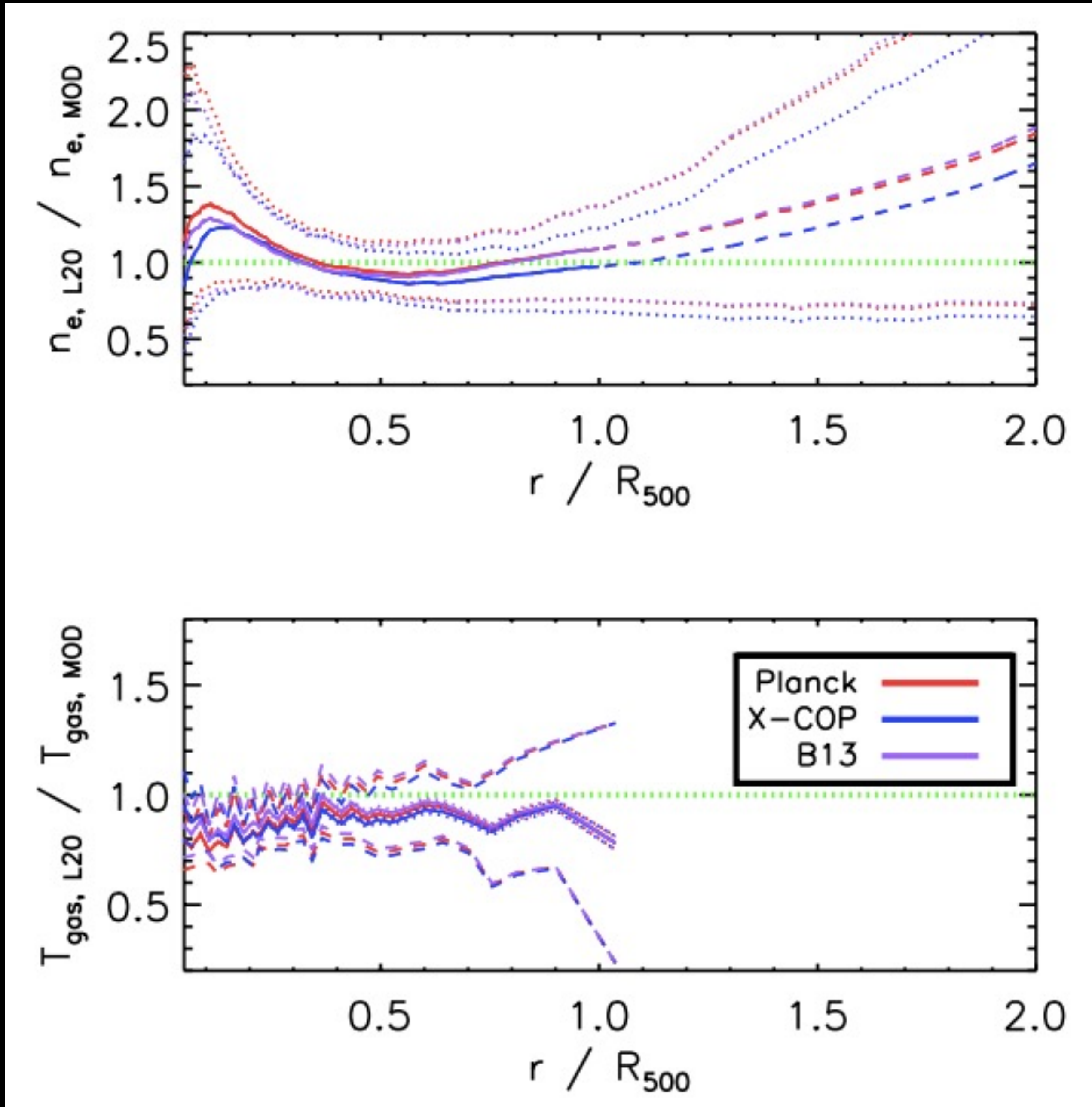

From universal profiles to universal scaling laws

- Some other applications: *Study the impact of b*; define the depletion parameter Y_b; **rescale the characteristic physical quantities that renormalise the observed profiles**

Table 1. Dependences of the characteristic physical scales on the temperature, mass, and redshift (as $E_z^{\alpha_z}$) in the self-similar and `i(cm)z` models.

Quantity	$f(M,z)$	$f(f_{\rm gas})$	$f(T,z)$	$f(M,z)$
	self-similar		`i(cm)z`	
T_Δ	$M^{2/3}\,E_z^{2/3}$	$f_{\rm gas}^0$	$T^{1+t_1}\,E_z^{t_z}$	$M^{2/3}\,E_z^{2/3}$
n_Δ	E_z^2	$f_{\rm gas}^1$	$T^{f_1}\,E_z^{2+f_z}$	$M^{2/3\,f_1/(1+t_1)}\,E_z^{2+f_z+f_1(2/3-t_z)/(1+t_1)}$
P_Δ	$M^{2/3}\,E_z^{8/3}$	$f_{\rm gas}^1$	$T^{1+t_1+f_1}\,E_z^{2+f_z+t_z}$	$M^{2/3+2/3 f_1/(1+t_1)}\,E_z^{8/3+f_z+f_1(2/3-t_z)/(1+t_1)}$
K_Δ	$M^{2/3}\,E_z^{-2/3}$	$f_{\rm gas}^{-2/3}$	$T^{1+t_1-2/3 f_1}\,E_z^{-4/3-2/3 f_z+t_z}$	$M^{2/3-4/9 f_1/(1+t_1)}\,E_z^{-2/3-2/3 f_z-2/3 f_1(2/3-t_z)/(1+t_1)}$

Notes. The basic equations are $T_\Delta = f_T T \sim T^{1+t_1} E_z^{t_z} = (E_z M)^{2/3} = (E_z^3 R^3)^{2/3}$ and $n_\Delta \sim \Delta\rho_{cz} \sim f_g E_z^2 \sim T^{f_1} E_z^{2+f_z}$. All the other relations were obtained by combinations of those.

Q_Δ	a_M	a_z	a_T	$a_{T,z}$
T_Δ	2/3 [2/3]	2/3 [2/3]	1.14 (0.02) [1]	0.35 (0.06) [0]
n_Δ	0.23 (0.01) [0]	2.11 (0.03) [2]	0.40 (0.01) [0]	2.00 (0.02) [2]
P_Δ	0.90 (0.01) [2/3]	2.78 (0.03) [8/3]	1.55 (0.02) [1]	2.35 (0.06) [2]
K_Δ	0.51 (0.01) [2/3]	−0.74 (0.02) [−2/3]	0.88 (0.02) [1]	−0.98 (0.06) [−4/3]